SWITCHING REGULATOR CONFIGURATIONS

and

CIRCUIT REALIZATIONS

Thesis by

Loman Rensink

In Partial Fulfillment of the Requirements

for the Degree of

Doctor of Philosophy

California Institute of Technology

Pasadena, California

1980

(Submitted December 3, 1979)

ACKNOWLEDGEMENTS

My advisor, Professor R. D. Middlebrook, has given me direction in my scholastic endeavor through his experienced counseling, keen perception of pertinent problems, and helpful suggestions toward their solution. He and my informal advisor, Professor S. Ćuk, have cultivated an intellectually stimulating environment in the Power Electronics Research Group conducive to the progress of research.

My thanks to Mrs. Michelle Schroeder for her industrious and attentive typing of the manuscript and to Hughes Aircraft for financial support by way of their fellowship program.

Of great personal importance to me has been the understanding, encouragement and support of my wife Shirley through my years of higher education.

ABSTRACT

Methods for obtaining improved performance from switching regulators with respect to their noise generation characteristics and dynamic response are developed through topology selection, refinement and generation, and by application of modern control techniques to both continuous and discrete time converter models.

Reduction in switching noise is attained by focusing analysis and design effort on rendering the external converter current waveforms as near to the ideal dc quantities as possible. Three techniques, not relying on conventional low-pass filtering, are promoted and several new or refined converter topologies are generated with these methods. In addition, a power-processing elliptic-function filter specifically designed to meet the requirements of the switching conversion environment and applicable to many common converter types is presented. Performance of the new low-noise converter topologies is substantiated by several circuit realizations and laboratory measurements.

Switching regulator dynamic performance is optimized by use of modern control theory in conjunction with the state-space-averaging technique. State-vector feedback coefficients which will minimize transient error excursions are determined through use of generally applicable algorithms for optimal linear regulator design.

An alternative approach is developed that relies on a discrete-time formulation of converter and regulator dynamics that is the dual to state-space-averaging. Among the important results are a simple expression for duty-ratio-controlled inductive current bandwidth of wide applicability, and a general solution for obtaining the fastest possible transient response from a switching regulator. The results of the control analysis are convincingly supported with laboratory measurements.

TABLE OF CONTENTS

INTRODUCTION

The proliferation of sophisticated electronics in commercial, military, and aerospace applications is accompanied by numerous demands for diverse forms of electric power. Electric energy obtained from a public utility or derived from a primary power source is often in improper form or fails to meet user regulation requirements. Thus it is frequently the case that electric energy must be converted from one form to another and/or regulated to obtain characteristics suitable for operation of modern electronic and electric equipment.

Power processing techniques are in themselves widely varied in form, complexity, and performance ranging, for example, from a simple resistive divider network to highly-efficient feedback-controlled switched-mode converters employing elaborate logic to adapt to varying source and load conditions. The spectrum of power processing approaches can be divided into two general classifications, linear and switching converters or regulators, even though many schemes may use a combination of both. The distinction between the two types of conversion lies in the fundamental circuit operation. Linear regulators are essentially dissipative in nature, using resistors or active devices to effect regulation by diverting or restricting the flow of energy from the source to the load. As the name implies the linear regulator may be analyzed by standard linear circuit analysis techniques without difficulty. Potential advantages of the linear in addition to ease of analysis include wide bandwidth and excellent noise characteristics. In contrast, switching regulators are ideally non-dissipative, relying principally on switching

elements and reactive components to effect the desired processing function. "Switchers" typically offer smaller size and weight along with higher efficiency, but are inferior to linears with respect to bandwidth and noise characteristics. The very switching action responsible for the converter's attributes also generates undesirable noise and imposes fundamental limitations on system bandwidth. In addition the switcher is more difficult to analyze since it is inherently nonlinear.

In spite of the apparent difficulties with switching regulation, the arguments in its favor are such that there is strong motivation to gain the advantages of switching while one seeks to alleviate its drawbacks. Commercial applications for power processing must consider the benefits of increased efficiency. Low efficiency not only costs the user for wasted power, but also penalizes him with respect to heat dissipation requirements. With the increasing price of energy, long-term cost analysis is moving steadily in favor of high-efficiency conversion schemes for more applications even if the initial expense is greater. In military and aerospace projects severe size and weight constraints are often added to high efficiency requirements making switching regulation the only effective alternative. Thus topics of considerable interest at present and in the foreseeable future are those of <u>improvement in the noise characteristics of switching converters and extension of their bandwidth</u>, both of which are considered herein.

Part I of this work contains analysis of existing switching dc-to-dc converter topologies with respect to their input and output current characteristics. Some converters are found to possess pulsating external

current waveforms at either input or output, or both. The step discontinuities of current associated with pulsating waveforms interact with circuit parasitics to generate spurious high frequency ringing and noise which, in the absence of external filtering, is transmitted directly to the source or load. One family of converters does not suffer as severely from this additional mode of noise generation since its external current waveforms are nonpulsating. The analysis effort focuses on this type of converter with the intent of understanding the sources of its already small current ripple so that refinements to the converter structure may further improve its compatibility with other electronic equipment. Three techniques of ripple reduction are developed which lead to the generation of several configurations possessing superior current ripple performance rivaling that of the linear regulator. Two of the approaches are found to be applicable to many common converter types. It is shown that such ripple attenuation can be attained with minimal impact on system size, weight and bandwidth, in contrast with conventional low-pass filtering techniques. The important analysis findings and resultant circuit topologies envisioned are verified by circuit realization and laboratory measurement of performance.

Part II of this work addresses the problem of extension of the dynamic performance of switching regulators by application of generalized multiple or total state-feedback control. Two approaches are examined.

The first approach makes use of an existing linearized small-signal system dynamic model in conjunction with the optimal linear regulator problem to derive feedback gains which minimize an integral quadratic

penalty function on state variable error and exercise of control. This technique has utility in that it is a general approach to regulation loop design and yields state feedback gains which are the best with respect to a chosen criterion. Since the most difficult step with this method is often the definition of a suitable performance objective, alternatives to penalty function parameter selection are developed in conjunction with closed-form answers for the optimal return gains. In certain circumstances it is shown that the engineer may achieve an optimal design with trade-offs posed in terms of meaningful system characteristics such as closed-loop bandwidth or feedback gain, instead of the possibly unfamiliar concept of quadratic penalty coefficients. Thus the configuration may be determined by familiar classical control criteria and practical engineering considerations with additional refinement provided by optimal control theory.

The second approach establishes generally applicable algebraic difference equations for the ac propagation of the state vector. The solution for the system response and for the desired feedback gains may be effected in either the time domain with matrix algebra, or the z-domain through use of transform theory. The principal advantage of this approach is that is uses the switching period T_s in the analysis and as such acquires extended accuracy in circumstances where sampling effects, inherent in switching conversion, are significant. This discrete model is promoted as an adjunct to the established classical modelling methods. As such, the relationships between the existing continuous-time model and the discrete model are derived so that either may be employed as deemed

appropriate, and the engineer is afforded an easily adjustable point of view. The advantages obtained are illustrated in an example where the continuous model is used to design an optimal voltage regulator with apparent unconditional stability irrespective of closed-loop bandwidth, and subsequently the discrete model provides a revised stability criterion which includes the previously neglected effects of sampling. The example clearly illustrates how one may benefit by using in harmony the modelling tools available. Since the merits of the discrete approach center around its ability to predict high frequency transient behavior, a challenging regulator design task is undertaken and subjected to time-domain measurements which clearly demonstrate the power of the modelling method. A converter is constructed and its regulation determined in accordance with a general solution for the linear feedback that will produce the fastest possible transient recovery from error. The response predicted and attained is termed a finite-settling-time response since the error decay completely transpires in two switching cycles. The solution for the finite-settling-time feedback gains and the accuracy of the discrete modelling of converter dynamics are both convincingly verified by laboratory measurements on the example converter.

The content of this work illustrates how the performance of switching regulators in terms of noise characteristics and system bandwidth may be improved through topology selection and control technique, and how such improved configurations may be implemented without undue sacrifice in terms of size, weight or complexity. The results are not purely esoteric in nature but have practical application as evidenced by several circuit

realizations with appropriate substantiating laboratory measurements. Whenever possible the conclusions of analysis are reduced to simple conceptual forms without undue mathematical complexity so that they may be easily retained and understood at least on an approximate basis suitable for engineering guidance.

PART I

ELIMINATION OF SWITCHING

CURRENT RIPPLE

through

TOPOLOGY SELECTION AND GENERATION

CHAPTER 1

REVIEW OF BASIC DC-TO-DC CONVERTER TOPOLOGIES

In this introductory chapter four basic converter topologies are reviewed and discussed. Since three of the four converters have been in use for some time their action will be discussed only briefly for sake of completeness. The new converter is given a more complete exposition including some of its extensions to aid the reader in negotiating the remainder of this text, much of which is concerned with the unique properties of this recently developed converter topology. Particular attention is given to the external current waveforms typical for the converters since the noise characteristics are in part determined by the magnitude of the switching disturbance on these currents. The new converter is found superior in this respect and some of its extensions are found to exhibit rather curious, potentially very attractive behavior which provides motivation for its more detailed analysis in the succeeding chapters of Part I.

In the following four chapters the input and output current characteristics of the new converter topologies will be analyzed and exploited. Results include the generation and laboratory verification of several new configurations with very desirable current ripple and hence noise characteristics. Such performance is shown to be attainable without undue sacrifice of bandwidth or compromise in size and weight.

1.1 The four basic converter topologies

In this context a "basic" switching converter topology is defined as one which is comprised only of a single switch and the reactive elements necessary for the proper conversion action without provision of transformer isolation. With these restrictions there are only four possible basic topologies known, the fourth of which was only recently introduced. Figure 1.1 illustrates the basic topologies with their ideal switch representation and the corresponding bipolar device realization.

In all of the discussion in this text the converter switches will be assumed to operate in the constant-frequency duty-ratio-controlled mode. The switch is in position A for time DT_s, the duty ratio D corresponding to the fraction of the switching period T_s that the transistor conducts. For the remainder of the switching period $D'T_s = (1 - D)T_s$ the switch is in position B indicative of diode conduction. Implicit in this description is the assumption that the converter inductor currents never fall to zero during $D'T_s$, which would result in an open diode and transistor and hence a third switch position. Equivalently stated, constant frequency, duty ratio modulated, continuous conduction mode of operation is assumed for all converters considered herein.

Perhaps the most fundamental of all the converters shown in Fig. 1.1 is the buck converter. The switching action in the buck merely applies a square wave of voltage to the output averaging LC filter. As such the dc voltage gain is simply $V/V_g = D$, the relative switch on time. Note that i_{out} is a nonpulsating quantity since the derivative

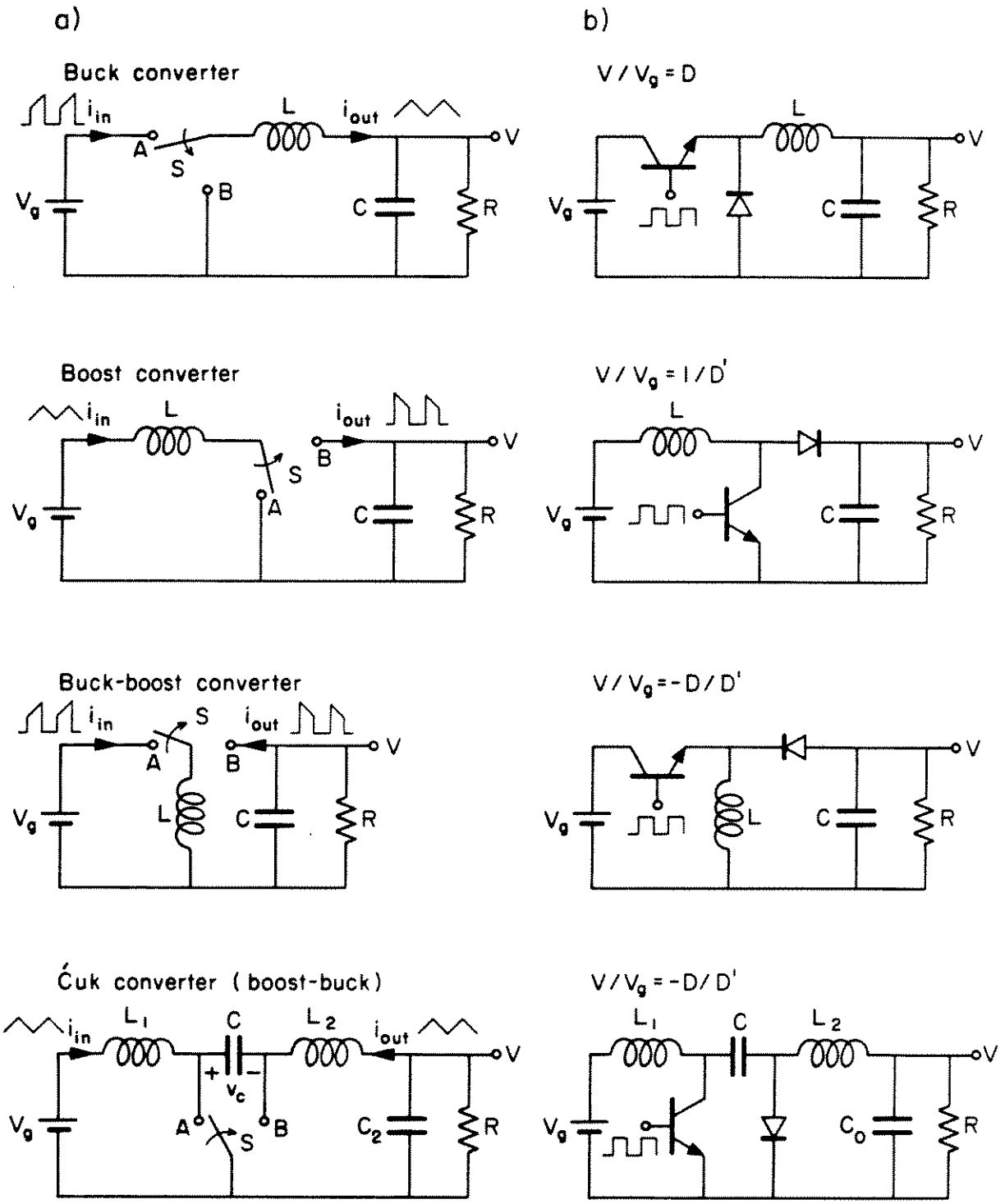

Fig. 1.1 The four basic converters with input and output current waveforms illustrated and dc voltage conversion function indicated; a) ideal switch representation, b) bipolar device implementation.

of i_{out} is fixed by the inductor L and the voltages applied. In contrast, the input current to the buck labeled i_{in} is a pulsating quantity, flowing while the switch is on and abruptly interrupted when the switch turns off. This input current characteristic is one undesirable feature of the buck converter since it often necessitates the inclusion of an input low-pass filter to reduce interference between the converter and other electronics operating from the same source.

The boost converter, as its name implies, performs a step-up voltage conversion given by $V/V_g = 1/D'$. The switching action first stores energy in L during the switch on-time DT_s and then releases energy into C during $D'T_s$. In the case of the boost the input current i_{in} flows continuously while the output current into R and C pulsates.

The buck-boost converter is an inverting topology with its conversion function a combination of the buck and boost such that $V/V_g = -D/D'$. Since the switch acts to commute the continuous inductor current alternately between input and output neither i_{in} nor i_{out} is smooth.

In sharp contrast to the buck-boost is the Ćuk converter [1], a boost-buck topology named after its inventor Slobodan Ćuk. This switcher may also be referred to as the "new converter" since it is the most recently discovered basic topology. The new converter has the same inverting dc voltage transfer function as the buck-boost, $V/V_g = -D/D'$, but at that point the similarity ends. The switching action in the Ćuk converter boosts the input voltage into the energy transfer capacitor C such that $V_c = V_g/D'$. In turn the capacitor voltage is

bucked to the output so that $V = -DV_c$. It may be seen that the capacitor serves as the energy transfer medium in this circuit while in the buck-boost and the other two the energy transfer element is an inductor. Further, the input and output currents in the new converter are nonpulsating, an important property unique to the new topology, lessening problems associated with electronic interference. Figure 1.2 illustrates the typical input and output current waveforms for the Ćuk converter. Both input and output currents are smooth with a roughly triangular inductive ripple current superimposed on the dc levels. The currents ramp upward during the switch on-time and downward when the switch is off, but never fall abruptly to zero. This current ripple behavior is common to the basic Ćuk converter and several of its extensions.

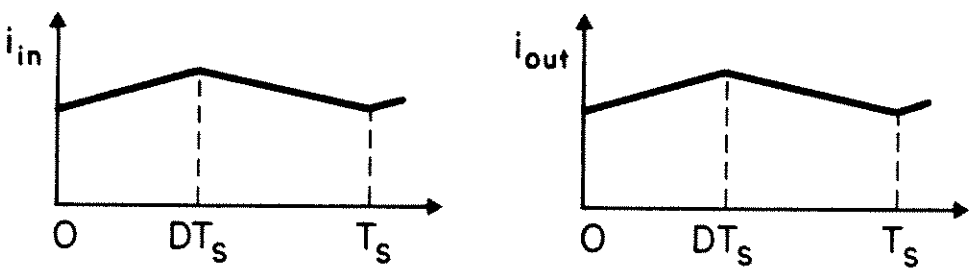

Fig. 1.2 Typical input and output current waveforms for the Ćuk converter showing the nonpulsating nature of the external currents.

1.2 Some extensions of the basic Ćuk converter

Many extensions to and applications of the basic new converter have been envisioned and constructed [2-10]. Just a few of these will be described here to prepare the reader for the discussion of the next several chapters.

Transformer isolation may be implemented in the basic converter by use of a split energy transfer capacitor, with the isolation transformer placed in the dc blocked position between the two fractions of the capacitor [2]. Figure 1.3 shows a transformer-isolated Ćuk converter. The transformer in Fig. 1.3 is shown 1:1 noninverting, but the possibility exists for polarity inversion at the transformer making the converter noninverting, or for different turns ratios affecting the voltage transfer function. In addition the isolation transformer makes

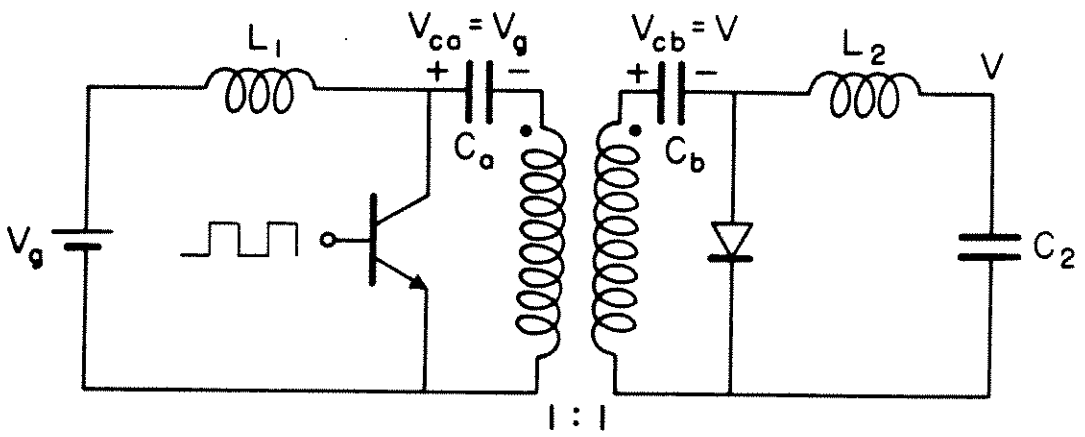

Fig. 1.3 Transformer-isolated Ćuk converter with dc values of voltages on the split energy-transfer capacitors indicated. The simple case of a 1:1 noninverting single-output transformer is illustrated.

possible multiple-output versions of the converter. The converter shown in Fig. 1.3 operates in a virtually identical manner to the basic configuration with the same desirable current ripple characteristics. The only significant difference is that now transformer isolation is provided.

One extension of the basic converter that will be the subject of close scrutiny is the coupled-inductor version [3]. The observation was made that the voltage waveforms exciting current in L_1 and L_2 in Fig. 1.1 were identical irrespective of operating condition, which revealed the possibility of winding both inductances on a single core. When this is done the coupled-inductor Ćuk converter configuration of Fig. 1.4 results.

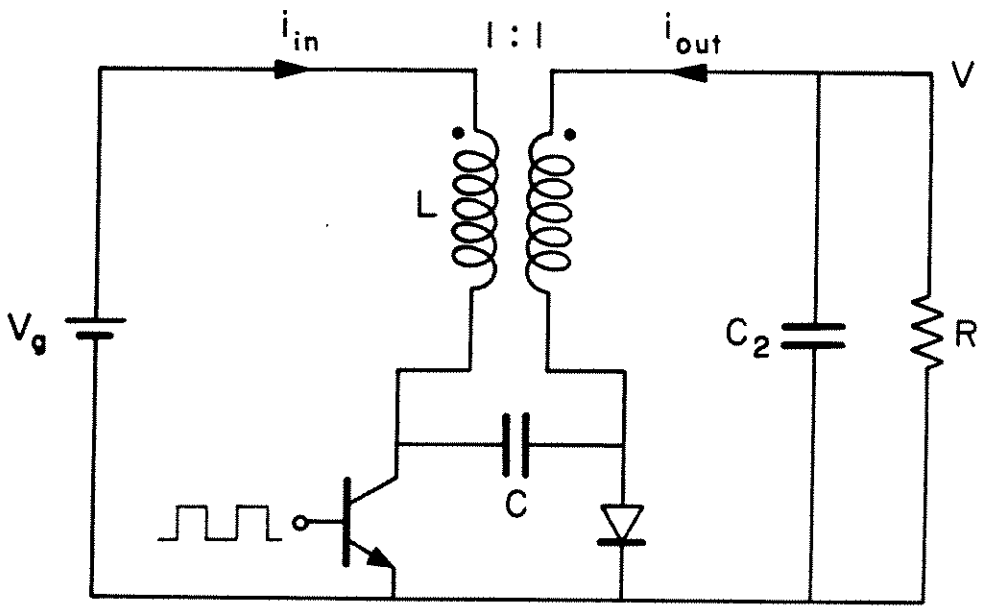

Fig. 1.4 Coupled-inductor Ćuk converter with input and output currents indicated.

The magnetic coupling of the inductors does not change the voltage conversion or nonpulsating current properties of the converter. It does however have major impact on the input and output current ripple characteristics. Only under certain circumstances are the typical waveforms of Fig. 1.2 observed. Some of the deviations observed from typical behavior are illustrated in Fig. 1.5.

Figure 1.5a shows the two current ripples distorted from the normal linear slope appearance in a regular but seemingly arbitrary manner. In 1.5b the output current is ramping downward when the switch is on, exactly the opposite of the normal inductive behavior. For descriptive purposes this is called the negative inductance effect since the output ripple behaves as though it were passing through the physically unrealizable but conceptually useful negative inductor. Of greatest interest is the condition illustrated in Fig. 1.5c. The output current has essentially zero ripple. This means that the output current properties are close to ideal. Similar behavior may be observed for the input

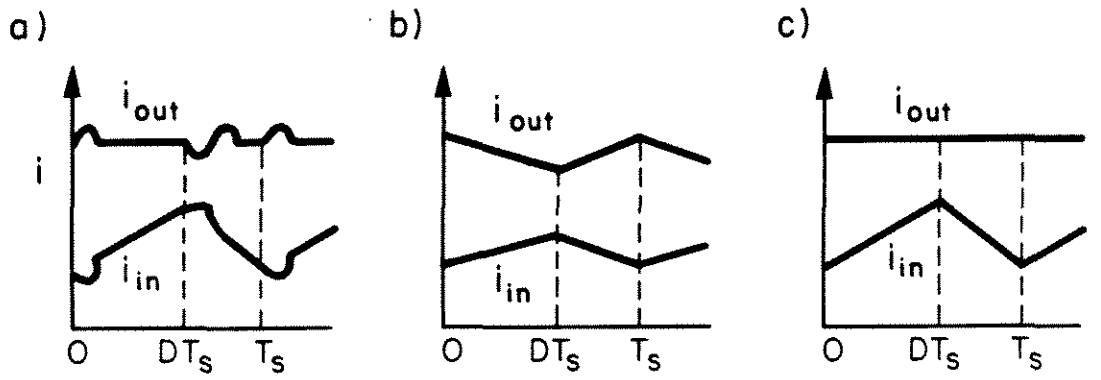

Fig. 1.5 External current waveforms observed for the coupled-inductor Ćuk converter; a) nonlinear behavior, b) negative inductance effect on output current, c) zero output ripple.

current under other conditions. Explanation and exploitation of these phenomena will be the subject matter of the first part of this work.

The coupled-inductor new converter is amenable to transformer isolation in a manner similar to the uncoupled-inductor version. Figure 1.6 shows a transformer-isolated coupled-inductor converter. Again the special case of a 1:1 noninverting isolation transformer is used for illustration even though several options are available. The option of importance to the ripple properties of the converter, as will be described later, is that the coupled inductor and the transformer may both be wound on the same core with the dot convention as shown [11]. Configurations such as this will lead to the possibility of zero current ripple at both the input and the output.

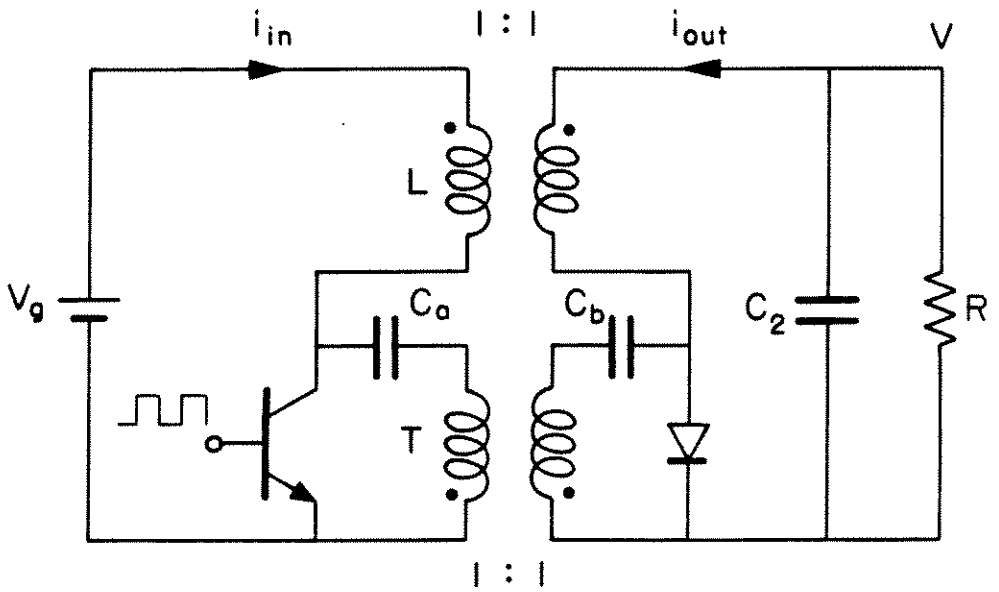

Fig. 1.6 Transformer-isolated coupled-inductor Ćuk converter. The coupled-inductor L and the transformer T may be wound on the same core with the dot convention as shown.

1.3 Review

The four basic converter topologies have been presented with emphasis on their input and output current characteristics. The new converter was discussed in more detail, with inclusion of a few of the extensions on the basic configuration. The only basic topology with nonpulsating input and output currents was found to be the new converter. In fact, the coupled-inductor extension of the new converter was shown to have the potential for a zero-ripple property, in that the output or input current ripple may essentially vanish under as yet unspecified conditions. Determination and discussion of these conditions follows.

CHAPTER 2

BASIC CURRENT RIPPLE CHARACTERISTICS OF THE COUPLED-INDUCTOR ĆUK CONVERTER

In this chapter the coupled-inductor Ćuk converter is modelled in an idealized form for simplicity and analyzed with respect to its current ripple properties. Insight gained from this basic analysis leads to linear circuit models for converter current ripple components. The inductive contribution to the ripples is shown to be of particular importance since very often it dominates. The associated impedance division model developed for inductive ripple behavior suggests several easily implementable coupled-inductor converter configurations with arbitrarily small current ripple at the input and/or output. The fundamental understanding of the converter process and the methods realized from this knowledge are applied to and used in conjunction with more sophisticated techniques discussed in following chapters.

2.1 Linear inductor and transformer

As a prelude to the examination of the coupled-inductor converter, it is of some use to establish relationships between the winding currents for linear inductors and transformers and the core flux. The simple case of the linear inductor is treated first.

Consider an idealized linear inductor consisting of n turns of wire carrying current i linking a well-defined magnetic path of length ℓ, cross section A_c, and constant permeability μ as illustrated in Fig. 2.1.

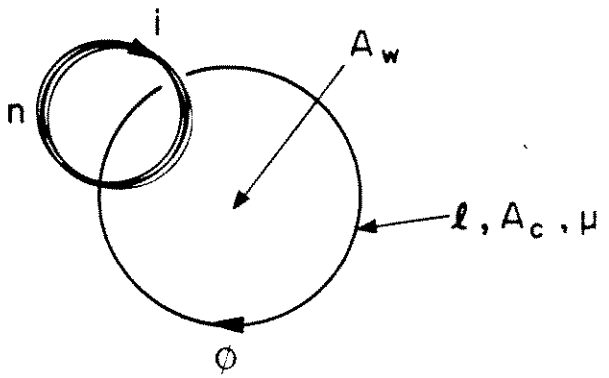

Fig. 2.1 Linear inductor model with a well-defined path for magnetic flux ϕ of length ℓ, cross-section A_c, and permeability μ, is linking n turns of current i passing through window area A_w.

Maxwell's equations in differential form as applied to the linear inductor state that the curl of the magnetic field strength is equal to the current density or, symbolically,

$$\nabla \times \underline{H} = \underline{J} = \frac{ni}{A_w} \tag{2.1}$$

By Stokes' theorem, the area integral of the curl may be evaluated as a closed contour integral. Thus integration of (2.1) yields

$$\int_{A_w} \nabla \times \underline{H} \cdot \underline{n} dA = \oint \underline{H} \cdot d\ell = H\ell \tag{2.2}$$

where $\underline{n}$ is a unit vector normal to the window area. Use of (2.1) and (2.2) results in

$$H\ell = \int_{A_w} \underline{J} \cdot \underline{n} dA = ni \tag{2.3}$$

Application of the constitutive relationship between flux density and magnetic field strength, $B = \mu H$, to (2.3) yields

$$B = \frac{\mu n i}{\ell} \tag{2.4}$$

The total core flux ϕ is $A_c B$, so from (2.4)

$$\phi = \frac{A_c \mu n}{\ell} i$$

or

$$n\phi = \frac{A_c \mu n^2}{\ell} i \tag{2.5}$$

Since $A_c \mu n^2/\ell$ is flux linkages per ampere it is inductance, and (2.5) may be rewritten

$$n\phi = Li \tag{2.6}$$

which is a useful and possibly familiar relationship from linear inductor theory.

Another of Maxwell's equations says for the electric field strength $\underline{E}$ that

$$\nabla \times \underline{E} = \frac{-d\underline{B}}{dt} \tag{2.7}$$

where d/dt indicates the derivative with respect to time. Again by Stokes' theorem

$$A_c \int \nabla \times \underline{E} \cdot \underline{n} dA = \oint \underline{E} \cdot d\underline{\ell} = -A_c \int \frac{d\underline{B}}{dt} \cdot \underline{n} dA \tag{2.8}$$

By definition the electrostatic potential v is given by

$$v = -\int \underline{E} \cdot d\underline{\ell} \tag{2.9}$$

Application of (2.9) to (2.8) yields

$$v = A_c \int \frac{d\underline{B}}{dt} \cdot \underline{n} dA = \frac{d\phi}{dt} \tag{2.10}$$

which prescribes the voltage per turn of wire. The voltage of n turns in series is then

$$v = n \frac{d\phi}{dt} \tag{2.11}$$

which is a statement of Faraday's law. With (2.6) and (2.11) established from basic relationships, we now have firm support for understanding the transformer in terms of its core flux.

Consider the 1:1 linear transformer with its primary winding excited by a voltage source as shown in Fig. 2.2. The transformer model shows all the flux linking both windings which is equivalent to perfect coupling, so in this respect the transformer is assumed ideal. The resistances R_1 and R_2 are included to model effects of winding, source, and load resistance. From the analysis of the linear inductor each winding is seen to possess self-inductance $L = \mu A_c n^2/\ell$, and by extension of (2.6) the flux linkages

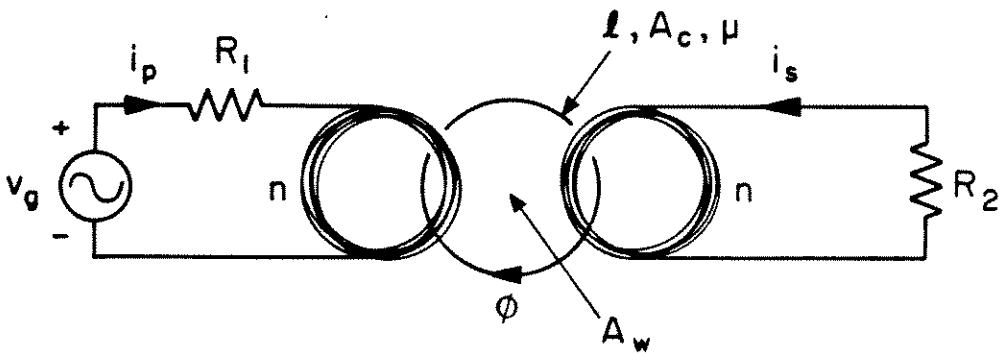

Fig. 2.2 Linear 1:1 transformer model with magnetic flux linked by both windings.

are

$$n\phi = L\,(i_p + i_s) \tag{2.12}$$

Use of Faraday's law (2.11) and Ohm's law to solve for i_p and i_s from Fig. 2.2 yields

$$\begin{aligned} i_p &= \frac{1}{R_1}\left(v_g - n\,\frac{d\phi}{dt}\right) \\ i_s &= \frac{-1}{R_2}\,n\,\frac{d\phi}{dt} \end{aligned} \tag{2.13}$$

Substitution of (2.13) into (2.12) and manipulation of the result gives the state equation for the transformer core flux ϕ:

$$n\,\frac{d\phi}{dt} = -\,(R_1 \,//\, R_2)\,\frac{n\phi}{L} + \frac{R_2}{R_1 + R_2}\,v_g \tag{2.14}$$

where $R_1 \,//\, R_2$ indicates the parallel combination of R_1 and R_2. Equations (2.14) and (2.13) combine to specify i_p and i_s in terms of the core flux.

$$\begin{aligned} i_p &= \frac{R_2}{R_1 + R_2}\,\frac{n\phi}{L} + \frac{v_g}{R_1 + R_2} \\ i_s &= \frac{R_1}{R_1 + R_2}\,\frac{n\phi}{L} - \frac{v_g}{R_1 + R_2} \end{aligned} \tag{2.15}$$

Equations (2.15) represent the attainment of the objective of this section. Extension of these equations to the case of the coupled-inductor new converter will provide understanding of its most basic current ripple characteristics.

2.2 Basic current ripple properties

A coupled-inductor new converter with arbitrary source and load impedance is illustrated in Fig. 2.3. The coupling between the inductors

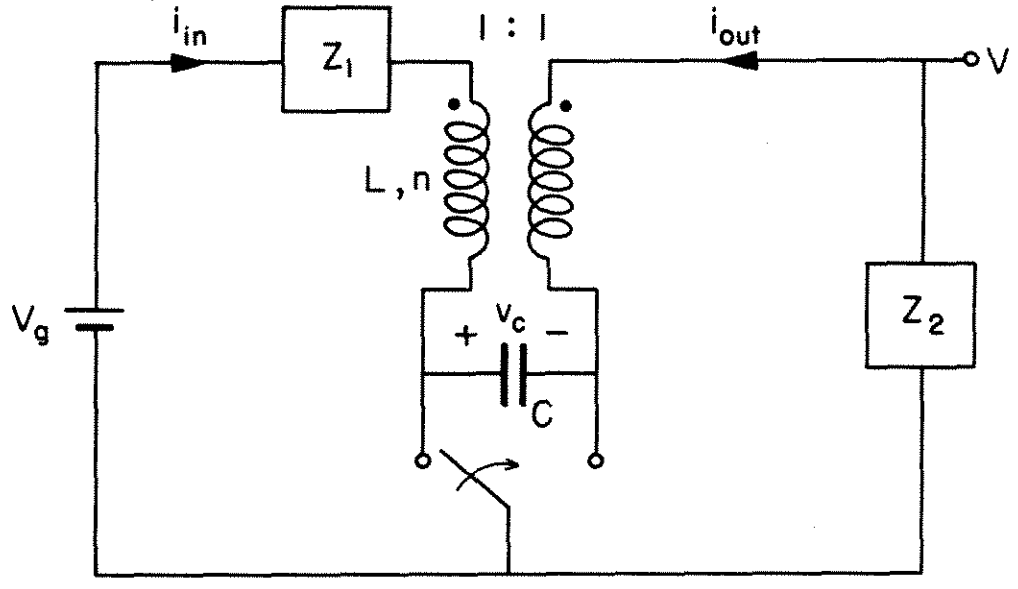

Fig. 2.3 Coupled-inductor converter with arbitrary source and load impedance.

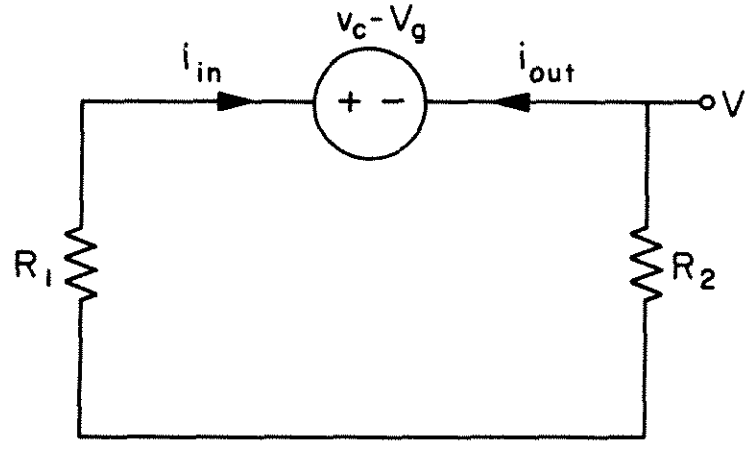

Fig. 2.4 Capacitor-voltage-induced or out-of-phase ripple model for the coupled-inductor converter with resistive source and load impedances.

is assumed perfect in accordance with the simple transformer model developed in the preceding section. Assume for the moment that Z_1 and Z_2 are resistive R_1 and R_2. Then, to examine the currents i_{in} and i_{out}, one may use the principle of superposition and equations (2.15) to find

$$i_{in} = \frac{R_2}{R_1 + R_2} \frac{n\phi}{L} + \frac{V_g - v_c}{R_1 + R_2}$$

$$i_{out} = \frac{R_1}{R_1 + R_2} \frac{n\phi}{L} + \frac{v_c - V_g}{R_1 + R_2} \qquad (2.16)$$

The surprising fact is that equations (2.16) are valid during both fractional periods DT_s and $D'T_s$. Notice that $(i_{in} + i_{out})L = n\phi$ as anticipated, and that current ripple attributable to core flux variation appears in phase on i_{in} and i_{out} according to the dot convention shown in Fig. 2.3. The contribution to the current ripples stemming from fluctuation in capacitor voltage is out of phase. It is fruitful to examine the separate current ripple contributions from the capacitor voltage and from the core flux. Figure 2.4 is an equivalent circuit showing how the capacitor voltage variations show up as input and output current ripples. The out-of-phase ripple on i_{in} and i_{out} is directly proportional to voltage ripple present on the energy transfer capacitance and inversely proportional to the series resistance of R_1 and R_2. This ripple component appears equally on the input and output currents irrespective of choice of R_1 and R_2. Some ripple contribution to both input and output currents due to this source is thus unavoidable. However, choice of a sufficiently large capacitor can easily make this component of ripple much smaller than the inductive component. The model of Fig. 2.4 may be conceptually extended to the case where R_1 and R_2 are again replaced by arbitrary impedances as shown in Fig. 2.5.

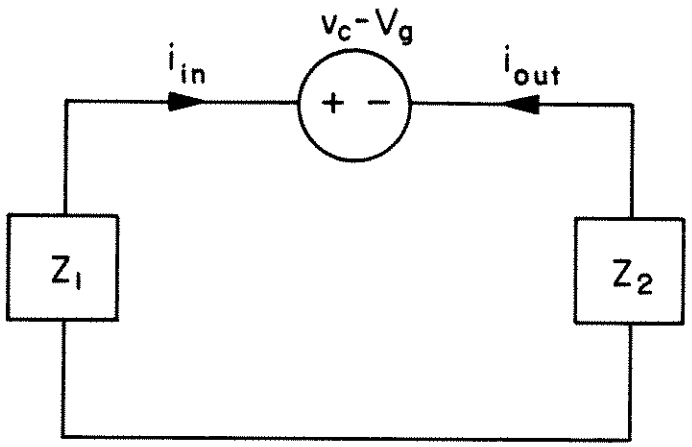

Fig. 2.5 Out-of-phase ripple model for a coupled-inductor new converter with arbitrary source and load impedances.

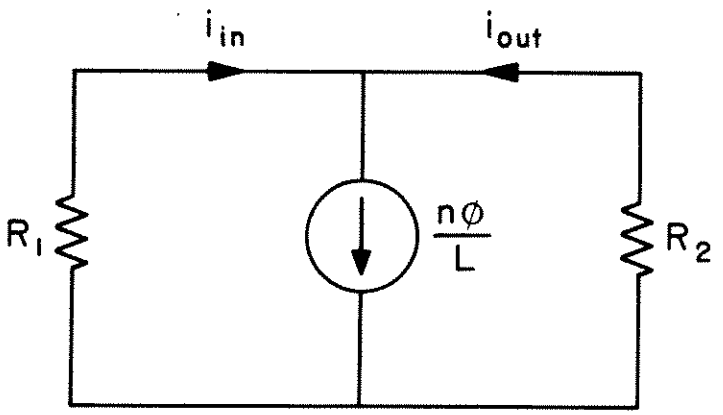

Fig. 2.6 Inductive-current-division or in-phase ripple model for coupled-inductor converter with resistive source and load impedances.

Allowing the presence of complex impedances admits the possibility of frequency dependence. If Z_1 or Z_2 contains series inductance then the impedance presented at the switching frequency, the fundamental frequency on the capacitor voltage, may be great, causing additional attenuation of out-of-phase ripple on both input and output.

In many cases the inductive ripple dominates the current ripple waveforms giving them their characteristic triangular appearance. Figure 2.6 models the in-phase inductive ripple contribution indicated in Eqns. (2.16). It is immediately evident that the core flux induced ripple divides between input and output according to the resistive current divider formed by R_1 and R_2. Experimentally this may be verified by building a converter with small capacitive ripple and with $R_1 = R_2$. The observation is then that the triangular ripple waveform is present in equal amounts on i_{in} and i_{out}. Also if for instance $R_2 >> R_1$, then the preponderance of the current ripple will appear on i_{in}.

As in the case of the out-of-phase ripple model let us extend the model of Fig. 2.6 to include complex impedances. Figure 2.7 illustrates the extended model. With complex impedances admitted to the model the behavior of the current waveforms becomes much more difficult to predict. For example, if Z_1 is a low source impedance and Z_2 is R // C_2, as may be the case for further voltage ripple attenuation, then the inductive ripple may divide about equally between input and output but in a complex frequency dependent fashion that leaves neither i_{in} nor i_{out} triangular in form. These are typical circumstances under which waveforms like those illustrated in Fig. 1.5a are observed. It should be evident that if one wishes to reduce the inductive ripple at either input or output this can

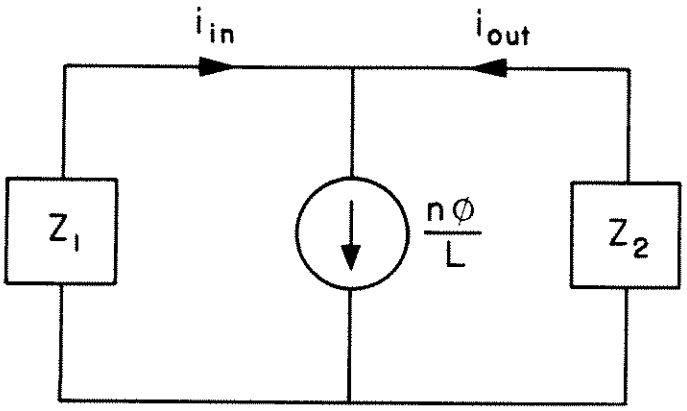

Fig. 2.7 Model of inductive current division for coupled-inductor converter with arbitrary source and load impedances.

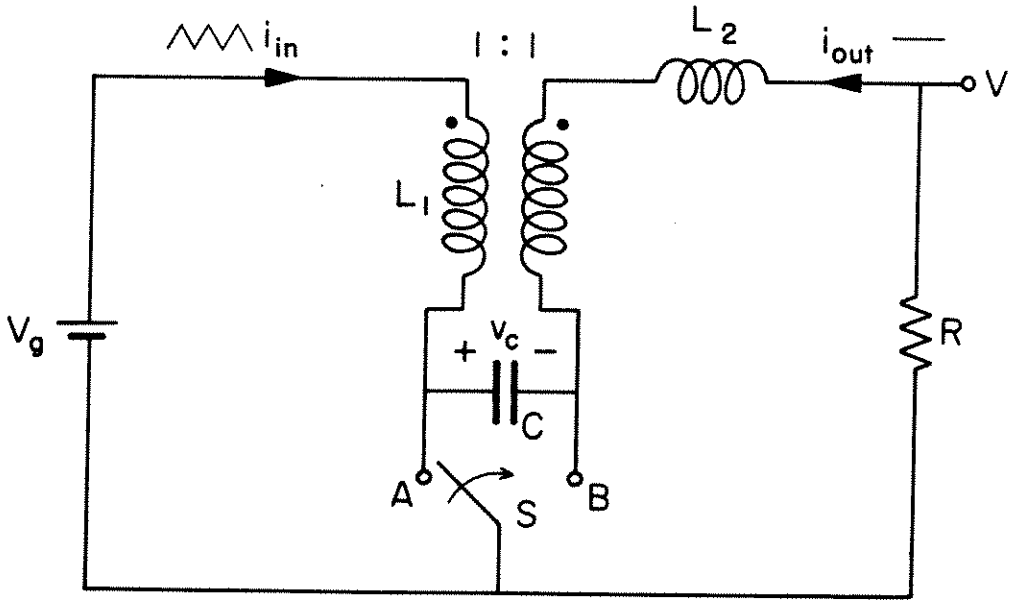

Fig. 2.8 Coupled-inductor new converter with inductance in the output current path using impedance division to render output current ripple-free.

be accomplished by an appropriate inequality in impedance magnitude between Z_1 and Z_2 effective at the switching frequency and higher. This again suggests the inclusion of inductance in one of the current paths.

To shed more light on the effectiveness of including inductive impedance in one of the current paths, let us examine the circuit of Fig. 2.8 where inductor L_2 is placed in the output current path. A simple but useful state-variable model of the circuit of Fig. 2.8 may be obtained by replacing the coupled inductor with an ideal transformer and modelling source impedance as resistive. Then the order of the system is three and the system states may be chosen as i_1, i_2 and v_c as illustrated in Fig. 2.9. If one uses the "zero state response" technique the state equations may be written by inspection of Fig. 2.9. The procedure is to assume all states and forcing functions are zero except for the state or forcing function whose matrix entry is under consideration. The operation relies on the principle of superposition for linear systems to obtain the complete correct result when all states and controls are examined individually. In this manner the state equations may be written for interval DT_s as

$$\frac{d}{dt}\begin{bmatrix} i_1 \\ i_2 \\ v_c \end{bmatrix} = \begin{bmatrix} \frac{-R_g}{L_1} & \frac{R_g}{L_1} & 0 \\ \frac{R_g}{L_2} & -\frac{R + R_g}{L_2} & \frac{1}{L_2} \\ 0 & -\frac{1}{C} & 0 \end{bmatrix} \begin{bmatrix} i_1 \\ i_2 \\ v_c \end{bmatrix} + \begin{bmatrix} \frac{1}{L_1} \\ \frac{-1}{L_2} \\ 0 \end{bmatrix} V_g \qquad (2.17)$$

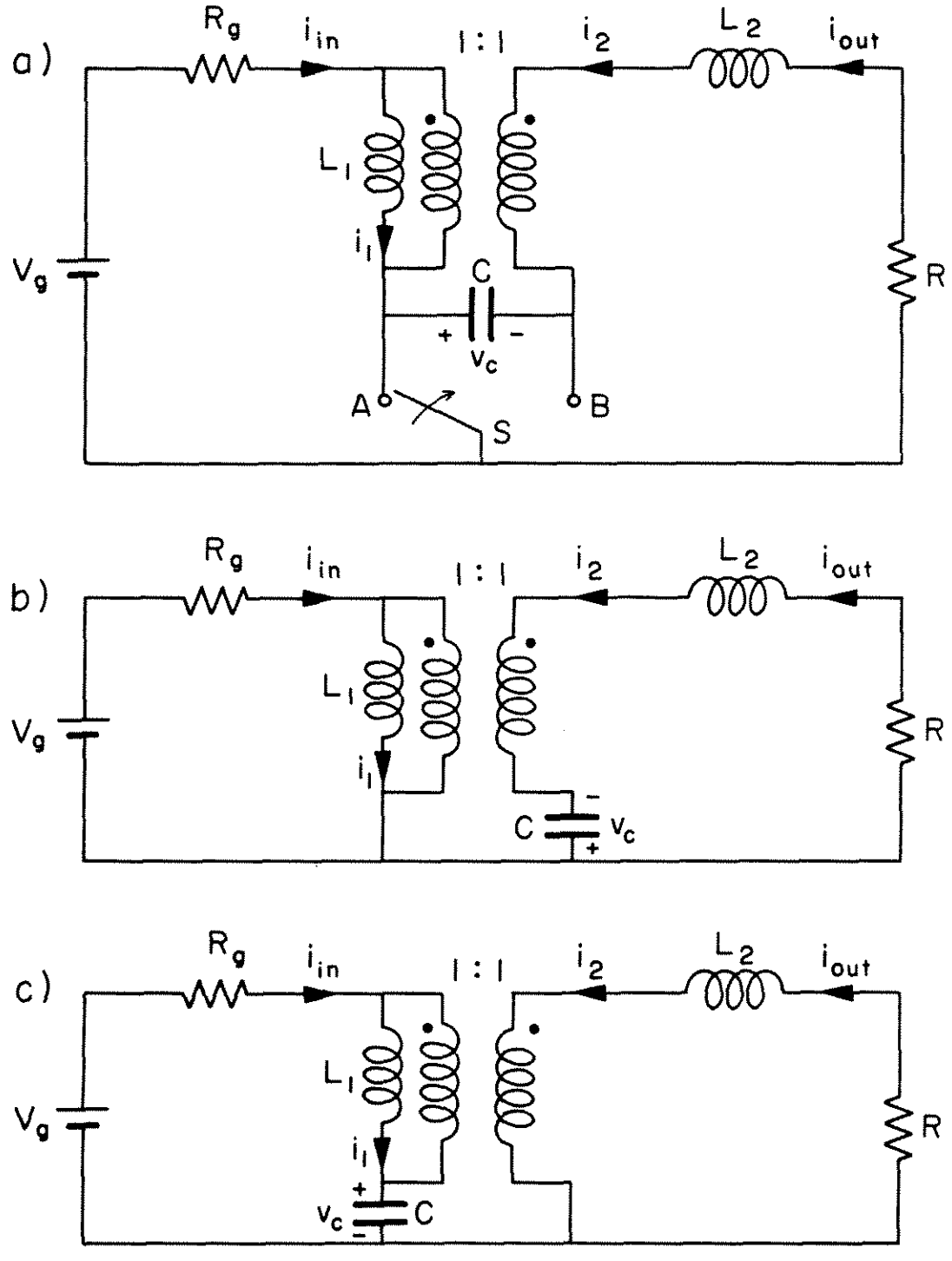

Fig. 2.9 State variable model for a low-output-ripple coupled-inductor converter with impedance imbalance arising from external inductor; a) ideal switch representation, b) switch in position A during DT_s, c) switch in position B during $D'T_s$.

For interval $D'T_s$ the state equations are

$$\frac{d}{dt}\begin{bmatrix} i_1 \\ i_2 \\ v_c \end{bmatrix} = \begin{bmatrix} \frac{-R_g}{L_1} & \frac{R_g}{L_1} & \frac{-1}{L_1} \\ \frac{R_g}{L_2} & -\frac{R + R_g}{L_2} & \frac{1}{L_2} \\ \frac{1}{C} & \frac{-1}{C} & 0 \end{bmatrix} \begin{bmatrix} i_1 \\ i_2 \\ v_c \end{bmatrix} + \begin{bmatrix} \frac{1}{L_1} \\ \frac{-1}{L_2} \\ 0 \end{bmatrix} V_g \qquad (2.18)$$

Notice that in equations (2.17) and (2.18) the expression for di_2/dt is invariant. Since i_2 corresponds to i_{out}, and the output current ripple is the one we desire to attenuate by insertion of L_2, it may prove fruitful to examine the differential equation for i_2 to see how the ripple characteristics on i_{out} agree with the anticipated behavior based on the models of Figs. 2.5 and 2.7. Extraction of the appropriate equation from either (2.17) or (2.18) yields

$$\frac{d}{dt} i_2 = -\frac{R + R_g}{L_2} i_2 + \frac{R_g}{L_2} i_1 + \frac{v_c}{L_2} \qquad (2.19)$$

Equation (2.19) is a first-order linear differential equation and hence the steady-state response of i_2 to excitation from state variables i_1 and v_c is easily obtained in the frequency domain via Laplace transform. With s denoting the transform variable, the behavior of $i_2(s)$ is

$$i_2(s) = \frac{R_g i_1(s) + v_c(s)}{sL_2 + R + R_g} \qquad (2.20)$$

This is precisely the frequency response predicted by the inductive current

division and out-of-phase ripple models developed earlier. The correlation with the models becomes quite apparent when (2.20) is rewritten as

$$i_2(s) = \frac{Z_1(s)\, i_1(s) + v_c(s)}{Z_2(s) + Z_1(s)} \tag{2.21}$$

where $Z_1(s) = R_g$ and $Z_2 = sL_2 + R$. The parallel impedance division of $i_1(s)$ and the series impedance attenuation of $v_c(s)$ are shown quite clearly.

Equation (2.21) and the current ripple models developed earlier are not useful for quantitative predictions because the excitation terms $i_1(s) = n\phi(s)/L_1$ and $v_c(s)$ are not known. In principle the equations (2.17) and (2.18) could be solved subject to matching boundary conditions, and analytic expressions for i_1 and v_c developed. In practice the task is formidable, unilluminating and lacks general application. However, some additional observations of a qualitative nature may be made by noting that $d/dt\ i_1 \propto 1/L_1$ and $d/dt\ v_c \propto 1/C$ where the symbol $\propto$ implies proportionality. Larger values of L_1 and C would reduce current ripple in the absence of L_2 and rather obviously will also aid in ripple reduction when L_2 or other impedance is present. Further, if the ripple present on the system state variables is small compared to their dc components, then the derivatives of the states are approximately constant. Design criteria for switching converters often make this constant slope or straight line approximation to the state variable behavior very accurate. (This point will be further discussed in Chapter 7.) Using the straight line approximation the magnitude of the peak-to-peak ripple on v_c and i_1 may be estimated from the state equations, the steady state duty ratio D, and

the switching period T_s. Then equations of the form of (2.20) may be employed with $s = j\omega_s$, ω_s the radian switching frequency , $j = \sqrt{-1}$, to obtain an estimate for the magnitude of the fundamental frequency component of the ripple. Such an estimate is often sufficient for engineering purposes since "second-order" effects such as capacitance esr and switch nonidealities not included in a tractable model become dominant when very small ripple is sought, and thus render mathematically precise analysis ineffectual.

2.3 Extensions of the impedance division principle

As mentioned in Section 2.2, the inductive $n\phi/L$ contribution to the converter current ripple often dominates the out-of-phase capacitive contribution, or may be made to do so by choice of sufficiently large capacitance. Under such circumstances control of inductive current ripple by utilization of the impedance division principle illustrated in Fig. 2.7 can make very significant improvement of the converter input and/or output current ripple characteristics. The model of Fig. 2.5 suggests that while increasing Z_1 or Z_2 for inductive ripple control one simultaneously diminishes the effects of voltage ripple on the energy transfer capacitor. With these facts in mind one is motivated to develop further applications of the impedance division principle.

Since input or output current ripple can easily be controlled by design of an appropriate impedance division of the $n\phi/L$ current, one is led to consider the existence of techniques for reducing input and output ripple. Equations (2.12) and the inductive ripple model insist that the currents in the two windings must sum to $n\phi/L$. Since storage in and dis-

charge of energy from the magnetic flux ϕ is part of the heartbeat of the converter, there must be ripple on ϕ and hence on the sum winding current. Therefore one cannot simultaneously prevent ripple from flowing in the input and output windings of the coupled inductor unless a third winding is present.

The question that immediately arises is whether or not the impedance division model is directly extendable to three or more windings on the coupled-inductor core. The answer is yes, and the justification simple. Faraday's law (2.11) tells us that the voltages around each winding must be the same when n, the number of turns, is constant. The voltage and sum current constraints on the windings lead immediately to the extension of the inductive current ripple model (Fig. 2.7) to a similar one with an arbitrary number of current loops all sourced from one current generator whose current is $n\phi/L$. Each current loop represents one winding on the core and the impedance associated with it. Such a model is illustrated in Fig. 2.10.

From Fig. 2.10 one may see that by adding a winding to the core which has a low impedance path to ground such that Z_3 is much less in magnitude than Z_1 or Z_2 for excitations at the switching frequency or higher, the inductive ripple may be diverted from input and output. One practical realization of a third winding technique is shown in Fig. 2.11. Such a configuration as shown was constructed in the laboratory and observed to give good performance. This configuration however, does not differ significantly from the application of LC filter sections to the input and output leads, a conventional approach. Even though the third winding on the core need only be large enough to handle the rms ripple current, it seems

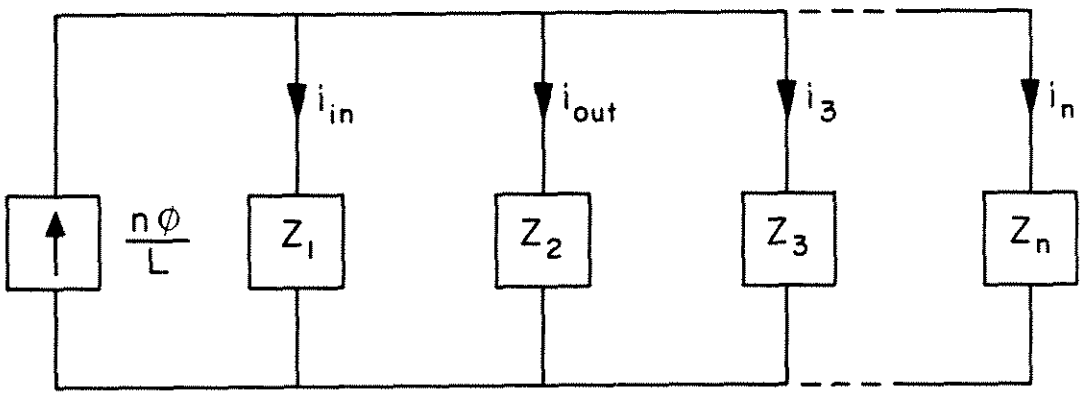

Fig. 2.10 Impedance division inductive current ripple model for the coupled-inductor Ćuk converter with an arbitrary number of windings on the inductor core.

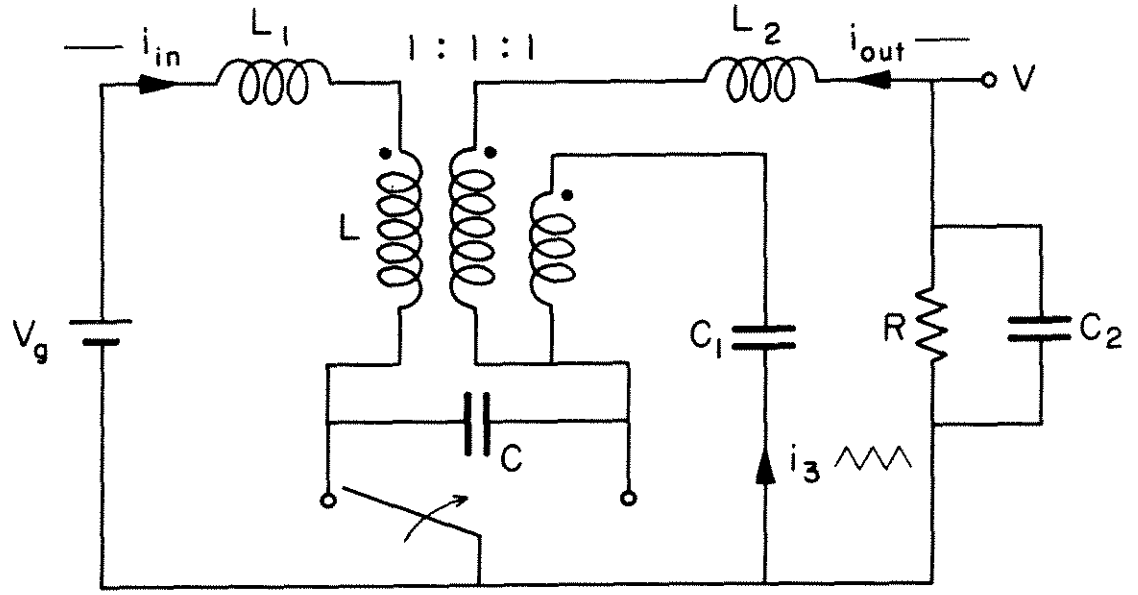

Fig. 2.11 Converter with small input and output current ripple utilizing a third winding with low ac impedance to sink inductive current ripple.

superfluous since C_1 could just as well be connected from the input or output lead on the coupled inductor to ground.

A more fruitful application of the impedance division principle is adding input and output inductances to the transformer-isolated coupled-inductor single-core Ćuk converter. This configuration already has two additional dc blocked low impedance windings to ground which provide the transformer isolation. Figure 2.12 shows a possible bipolar implementation of this topology. The preponderance of the $n\phi/L$ ripple will exist in the isolation transformer windings. The technique of Fig. 2.12 has good component utilization. The only added elements to the basic configuration of Fig. 1.6 are L_1 and L_2, which typically need not be very high in inductance to provide substantial reduction in ripple. It should also be evident that ripple attenuation is not very sensitive to component tolerance when this technique is used. Again we may note that this technique is tantamount to application of input and output LC sections to the converter, with the significant advantage that the isolation windings and the energy transfer capacitors C_1 and C_2 have dual roles with little additional stress.

One drawback to the circuit of Fig. 2.12 is that even though L_1 and L_2 are present to control the ac current waveform they must be made to stand a dc bias without saturating magnetically. The dc bias requirement makes L_1 and L_2 larger than a bias-free inductor of the same value. A size and weight advantage may be gained if one were to envision a way of reducing ripple without using inductors in the path of dc current. Considerations of improved topologies that circumvent the dc bias difficulty is reserved for the next chapter.

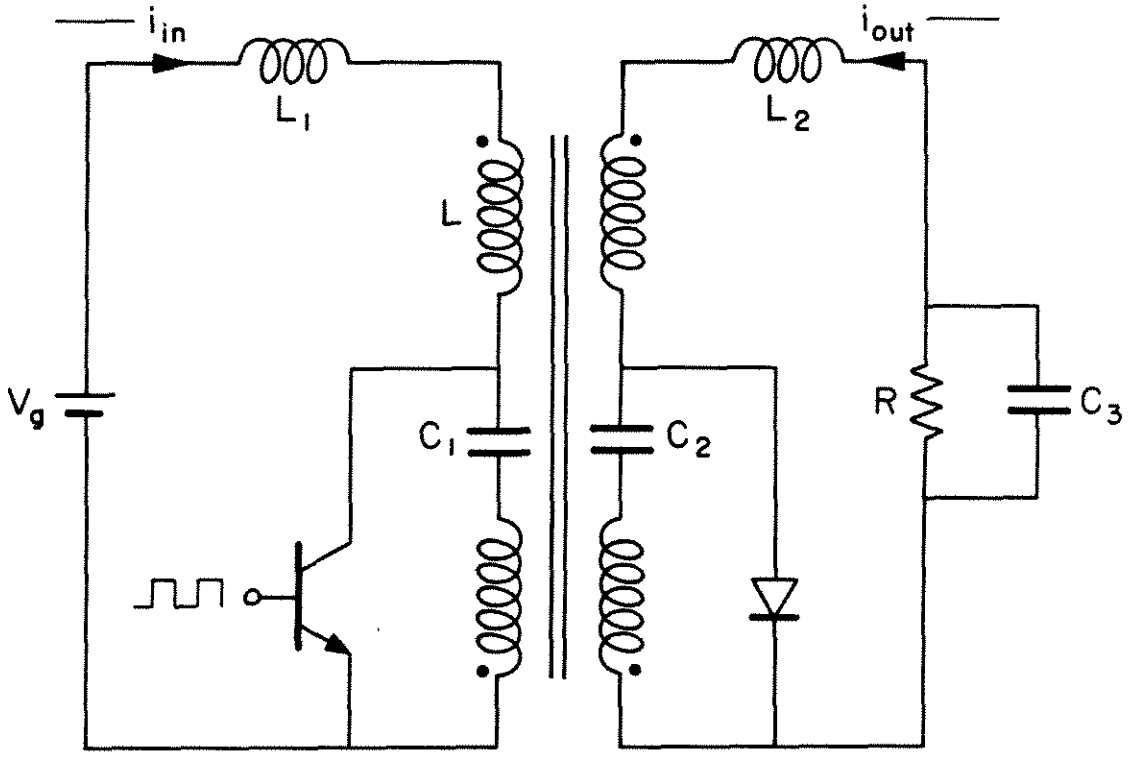

Fig. 2.12 Isolating new converter with small ripple on external currents utilizing isolation windings and energy-transfer capacitors as low impedance paths for current ripple.

2.4 Review

In this chapter fundamental results from basic electromagnetic relationships were used with an idealized model for the new converter to generate basic information concerning its current ripple characteristics. It was found that the input or output currents on the coupled-inductor converter could be made to have arbitrarily small ripple components by design of an appropriate impedance inequality between the two windings. The model of the division of inductive ripple current was further extended to embrace multiple windings on the coupled inductor core. Insight gained permitted one to envision converter topologies with arbitrarily small input and output current ripple. These extensions to the basic coupled-inductor converter are easily constructed and reproduced owing to their relative insensitivity to component tolerances. Finally, some observations about the new circuits were made which suggest possible goals for subsequent chapters.

CHAPTER 3

THE NEGATIVE INDUCTANCE EFFECT

The basic modelling of the coupled inductor as a 1:1 transformer developed in the preceding chapter is augmented to include arbitrary winding ratio. In this manner the extended model gains the additional degree of freedom needed to explain the zero ripple and negative inductance effects not predicted by the elementary impedance division model. In contrast with the methods of Chapter 2 the developments of this chapter show how the ripple may be made to flow in a winding with high impedance, if that impedance is inductive and of the appropriate size. Since the inductance value must be chosen precisely as a function of other circuit parameters, this method may be referred to as the impedance matching technique. Once established, the impedance matching concept is used to advantage to generate alternative coupled-inductor topologies with very desirable ripple characteristics. Some are configured in ways that result in reduced hardware size and weight by circumventing the need for additional inductors which carry dc current, as are used in the impedance division technique. The results are substantiated by hardware realization and laboratory verification demonstrating that the analysis is correct as well as practically applicable.

In the next two chapters the impedance matching method is applied to other converter topologies and analyzed in more detail. The detailed analysis leads to greater understanding of the ripple attenuation process and consequently to even further improvements in performance.

3.1 Arbitrary inductor turns ratio

Consider a transformer with arbitrary turns ratio excited by a voltage source. Figure 3.1 depicts a simple model of such a situation where R_1 and R_2 account for any resistance in the primary and secondary circuits. The model is idealized in that all the magnetic flux ϕ is assumed to link both primary and secondary windings. Application of Ohm's and Faraday's laws to the circuit of Fig. 3.1 to solve for i_p and i_s yields

$$i_p = \frac{1}{R_1}\left(v_g - n_1 \frac{d\phi}{dt}\right) \qquad \text{and} \tag{3.1}$$

$$i_s = \frac{-1}{R_2} n_2 \frac{d\phi}{dt} \tag{3.2}$$

Extension of (2.12) to embrace unequal turns ratios produces

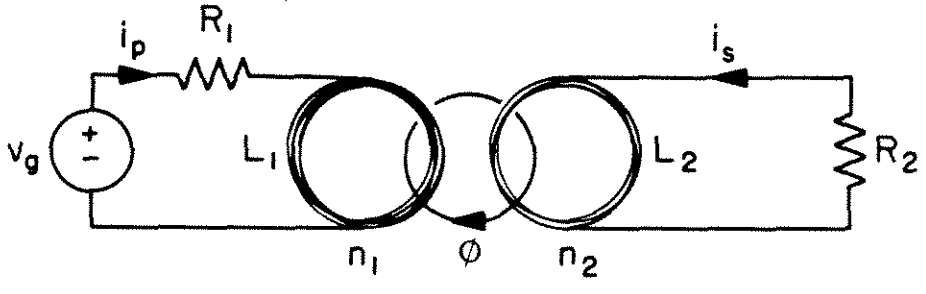

Fig. 3.1 Model of an idealized linear transformer with arbitrary winding turns ratio.

$$\frac{i_p L_1}{n_1} + \frac{i_s L_2}{n_2} = \phi \qquad \text{where} \tag{3.3}$$

$$\frac{L_1}{L_2} = \left(\frac{n_1}{n_2}\right)^2 \tag{3.4}$$

Substituting from (3.4) into (3.3) and utilizing (3.1) and (3.2), one may generate the equation of state for the primary flux linkage $n_1\phi$.

$$n_1 \frac{d\phi}{dt} = -\left[R_1 // \left(\frac{n_1}{n_2}\right)^2 R_2\right] \frac{n_1\phi}{L_1} + \frac{\left(\frac{n_1}{n_2}\right)^2 R_2}{R_1 + \left(\frac{n_1}{n_2}\right)^2 R_2} v_g \tag{3.5}$$

Equations (3.1) and (3.2) may be recast to show the dependence of the current upon the state $n_1\phi$, instead of upon the state derivative terms to obtain expressions similar to (2.15):

$$i_p = \frac{\left(\frac{n_1}{n_2}\right)^2 R_2}{R_1 + \left(\frac{n_1}{n_2}\right)^2 R_2} \frac{n_1\phi}{L_1} + \frac{v_g}{R_1 + \left(\frac{n_1}{n_2}\right)^2 R_2} \tag{3.6}$$

$$i_s = \frac{R_1\left(\frac{n_1}{n_2}\right)}{R_1 + \left(\frac{n_1}{n_2}\right)^2 R_2} \frac{n_1\phi}{L_1} - \frac{\left(\frac{n_1}{n_2}\right) v_g}{R_1 + \left(\frac{n_1}{n_2}\right)^2 R_2} \tag{3.7}$$

If in (3.7) the secondary current is reflected to its equivalent primary current value and labeled with a prime to denote the transformation,

(3.7) becomes

$$i'_s = \frac{R_1}{R_1 + \left(\frac{n_1}{n_2}\right)^2 R_2} \frac{n_1\phi}{L_1} - \frac{v_g}{R_1 + \left(\frac{n_1}{n_2}\right)^2 R_2} \quad . \tag{3.8}$$

The parallel between equations (2.15) and the pair (3.6) and (3.8) is evident. The latter shows the non-unity turns ratio by reflecting secondary impedance by the usual turns ratio squared, but preserves the same functional form. Let us apply these results to the coupled-inductor converter as before to see what differences arise owing to the introduction of arbitrary turns ratio.

3.2 Zero ripple and the negative inductance effect

Figure 3.2 shows the coupled-inductor converter with an arbitrary turns ratio, source and load impedance. Taking Z_1 and Z_2 real and equal to R_1 and R_2 allows one to use (3.6) and (3.8) to write equations for the input and reflected output currents for the two switch states by inspection of Fig. 3.2.

$$i_{in} = \frac{\left(\frac{n_1}{n_2}\right)^2 R_2}{R_1 + \left(\frac{n_1}{n_2}\right)^2 R_2} \frac{n_1\phi}{L_1} + \frac{V_g - v_c\left(\frac{n_1}{n_2}\right)}{R_1 + \left(\frac{n_1}{n_2}\right)^2 R_2} \qquad \text{during } DT_s \tag{3.9}$$

$$i'_{out} = \frac{R_1}{R_1 + \left(\frac{n_1}{n_2}\right)^2 R_2} \frac{n_1\phi}{L_1} + \frac{\left(\frac{n_1}{n_2}\right) v_c - V_g}{R_1 + \left(\frac{n_1}{n_2}\right)^2 R_2}$$

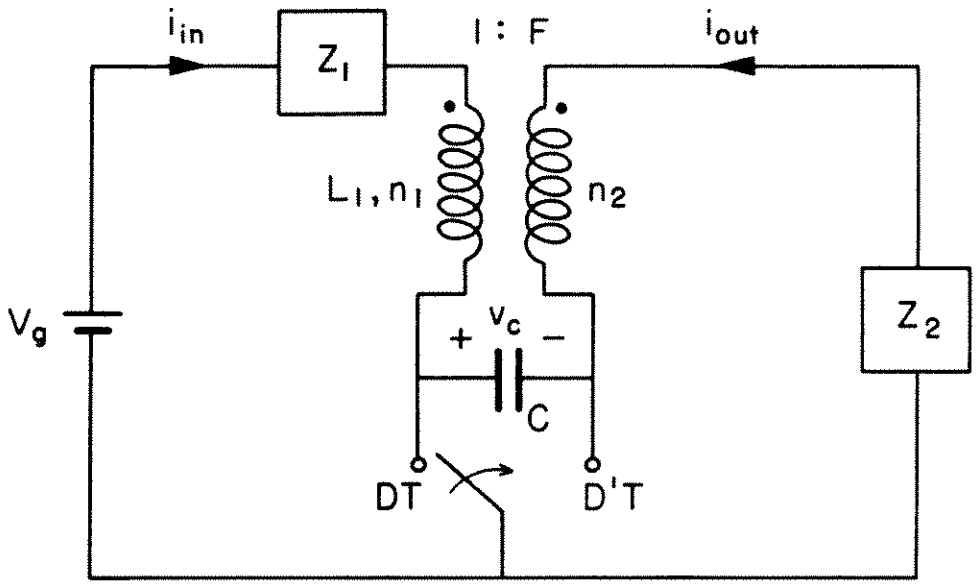

Fig. 3.2 Ćuk converter with arbitrary impedances placed in input and output current paths.

and

$$i_{in} = \frac{\left(\frac{n_1}{n_2}\right)^2 R_2}{R_1 + \left(\frac{n_1}{n_2}\right)^2 R_2} \frac{n_1\phi}{L_1} + \frac{V_g - v_c}{R_1 + \left(\frac{n_1}{n_2}\right)^2 R_2} \quad \text{during } D'T_s \quad (3.10)$$

$$i'_{out} = \frac{R_1}{R_1 + \left(\frac{n_1}{n_2}\right)^2 R_2} \frac{n_1\phi}{L_1} + \frac{v_c - V_g}{R_1 + \left(\frac{n_1}{n_2}\right)^2 R_2}$$

Introduction of the turns ratio other than unity makes the current equations (3.9) and (3.10) different for different switch positions,

whereas previously the parallel equations (2.16) were found to be invariant with switch position. Notice that the impedance division of the $n_1\phi/L_1$ ripple is still evident in (3.9) and (3.10) so that a model very similar to the previous impedance division model may be generated as shown in Fig. 3.3. As usual the prime indicates that the output current has been reflected to the input via the turns ratio. The essential difference lies in the fact that in (3.9) and (3.10) v_c can be seen to enter into the input and output current equations either directly or modified by the turns ratio (n_1/n_2). In effect, even if v_c can be considered constant as before, an ac excitation to the input and output currents at the switching frequency in the form of a square wave is present. Thus with non-unity turns ratio the capacitor voltage contribution to the current ripples cannot be ignored. A simple model, again

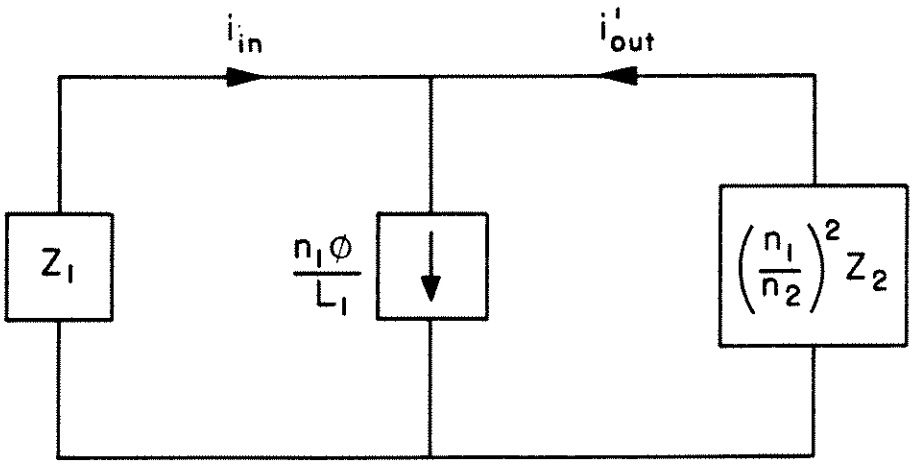

Fig. 3.3 Impedance division model with unequal turns on the primary and secondary windings of the coupled inductor.

with use of the extension to complex impedances is shown in Fig. 3.4. It seems as though the disturbance of the unity turns ratio has added to the input and output current ripples with no advantage gained. This would indeed be the case if Z_1 and Z_2 were purely resistive, but if one exercises some imagination with the possibility of complex impedances, a potential advantage to the additional "disturbance" depicted in Fig. 3.4 may arise. For sake of simplicity, consider for the moment that Z_1 in Fig. 3.4 is zero. Then, the square wave generator is impressed directly across $(n_1/n_2)^2 Z_2$. If Z_2 is primarily inductive, the current flowing in it will have a similar triangular waveform shape to $n_1\phi/L_1$, with the same phase and duty ratio effects. Realizing this, one may seek to define an appropriate Z_2 and turns ratio such that the v_c induced

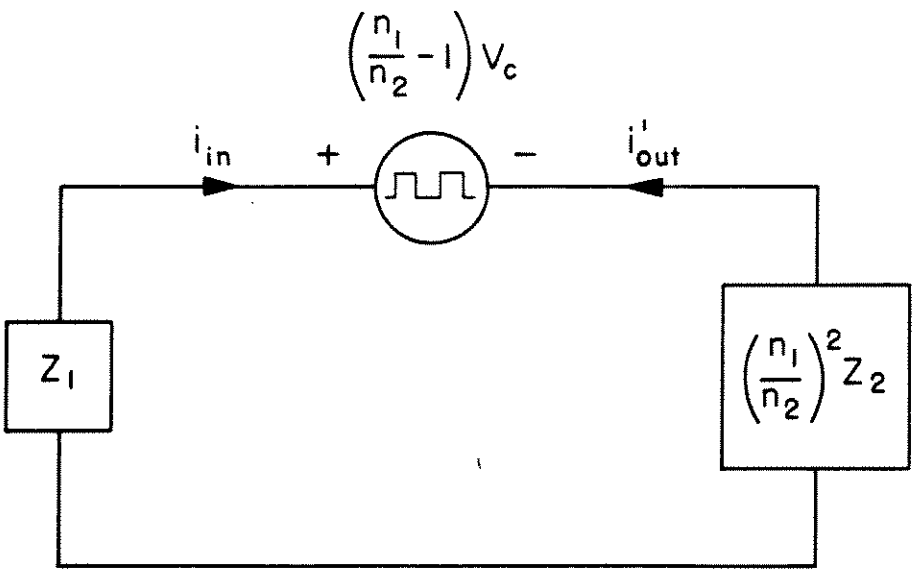

Fig. 3.4 Capacitor-voltage-induced ripple model with unequal turns on coupled inductor.

i'_{out} is precisely what is needed to sink the $n_1\phi/L_1$ current source of Fig. 3.3. If this current sinking effect can be made independent of duty ratio then the input ripple could be made to vanish irrespective of operating condition. Examination of the ac excitation on the coupled-inductor primary shows v_c entering there also as the square wave excitation magnitude. Since the time relationships and polarities of excitation of v_c on the inductor primary and $(n_1/n_2 - 1)v_c$ on the reflected output impedance are such that $n_1\phi/L_1$ could be made to flow through Z_2, the desired equality of current derivatives is

$$\frac{v_c}{L_1} = \frac{(n_1/n_2) - 1}{(n_1/n_2)^2 L_0} v_c \tag{3.11}$$

where L_0 is the required secondary inductance. From (3.11) we may solve for L_0 normalized to L_1 as

$$L_0/L_1 = F(1 - F);\ F = n_2/n_1 \tag{3.12}$$

Equation (3.12) specifies the secondary inductance and appropriate turns fraction necessary to generate an output current waveform virtually identical to the waveform produced if all the $n_1\phi/L_1$ ripple were to flow in the output winding. Perhaps an example circuit would serve to clarify the present development.

Figure 3.5 is a sketch of a coupled-inductor Ćuk converter with unequal turns on the inductor and an inductive impedance in the secondary. The inductor L_0 in the secondary is chosen in conjunction with R_2 and C_2 such that at the switching frequency the secondary impedance is essentially $j\omega_s L_0$. Then the apparent square wave produced by C switching between the primary and secondary circuits induces a triangular ripple in the output winding. If F and L_0 are chosen in accordance with (3.12), then the

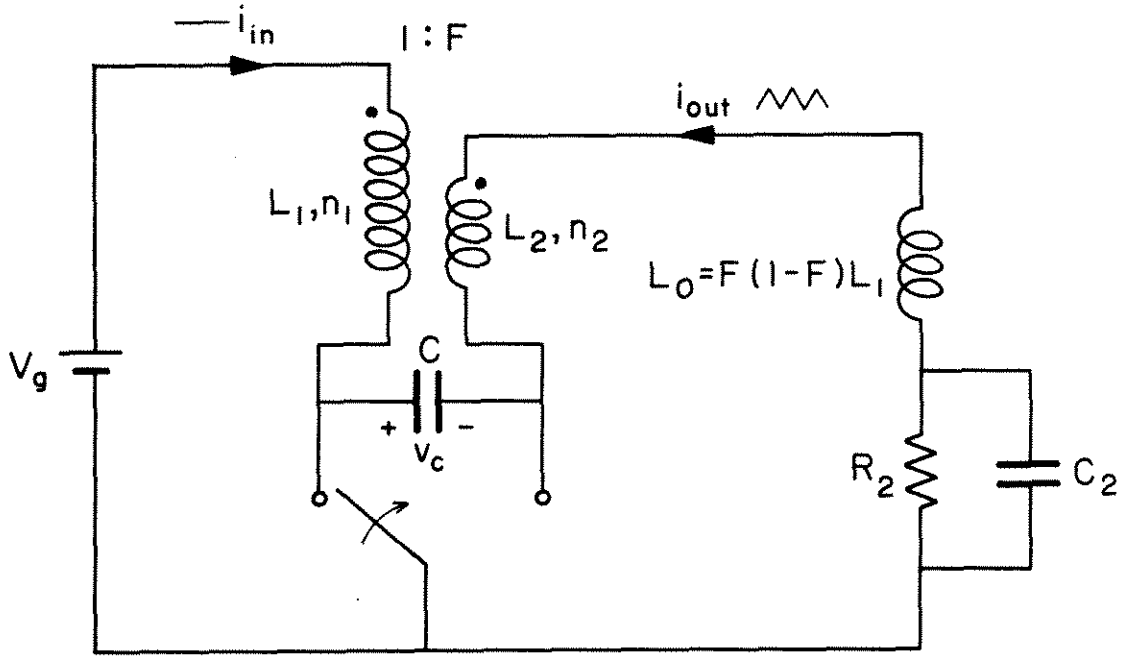

Fig. 3.5 Zero input ripple configuration with matching inductor L_0 in output current path whose value is related to the turns fraction F by the matching condition $L_0/L_1 = FF'$.

magnitude of the ripple is such that

$$\tilde{i}_{out} = \frac{n_2\tilde{\phi}}{L_2} \tag{3.13}$$

where $\sim$ indicates ac terms. Since we have

$$\frac{\tilde{i}_{in}L_1}{n_1} + \frac{\tilde{i}_{out}L_2}{n_2} = \tilde{\phi} \tag{3.14}$$

from (3.3) it may be seen that (3.13) implies $\tilde{i}_{in} = 0$ or the input current is dc only. Reduction of L_0 from its value prescribed in (3.12) will make the output ripple greater than $n_2\tilde{\phi}/L_2$, and thus will result in a ripple on i_{in} of inverted form to satisfy (3.14). Conversely, if L_0 is too large the ripple on i_{in} will be of normal form to preserve the equality in (3.14). Thus by varying L_0 for a given F the ripple at the input may be made to pass from a normal positive polarity, ramping upward during DT_s and downward during $D'T_s$, to a negative polarity with opposite sense. The fact that the ripple may be made continuously adjustable from positive to negative polarities gives rise to the notion that, to the extent that the waveform is purely triangular, it must pass through a zero condition in between. Hence, when a negative inductance effect can be demonstrated, the configuration may be termed a "zero ripple" configuration subject to qualifying assumptions noted in the development.

It is appropriate at this point to pause and compare the developments of this chapter with those of the previous one. The impedance division technique sought to inhibit the ripple in a prescribed winding by placing a large switching-frequency impedance in that winding. This chapter's

impedance matching technique seeks to enhance the ripple in a prescribed winding by placing a calculated high impedance there corresponding to a chosen turns ratio. The impedance matching technique may generate positive or negative ripple characteristics as the matching inductor is varied about the value prescribed in (3.12). The impedance division technique will not exhibit negative ripple and may be demonstrated with arbitrary impedances not necessarily inductive.

One may comment on the preceding development before proceeding to exploit the matching technique. Even though Z_1 was assumed zero in the generation of the matching conditions, this is not required in general. With $\tilde{i}_{in} = 0$ there will be no ac voltage impressed across Z_1 and hence its value is of no concern. Actually a large Z_1 may be desirable in desensitizing the matching condition by simultaneously using the impedance division principle with the matching technique. There is no apparent conflict between the two methods and in fact the matching condition may be viewed as making the high impedance in the matched winding a very low impedance to inductive current ripple. The compatibility of the two methods increases the value of each.

The circuit of Fig. 3.5 still has the disadvantage previously noted for the impedance division technique. That is, the inductor L_0 must be designed as a dc biased component with attendant additional size. Since the matching technique can cause the ripple to flow in a desired winding, one is immediately led to consider application of a third winding, with the appropriate ripple frequency impedance and turns ratio, to act as an ac ripple sink for the converter. Figure 3.6 depicts such a

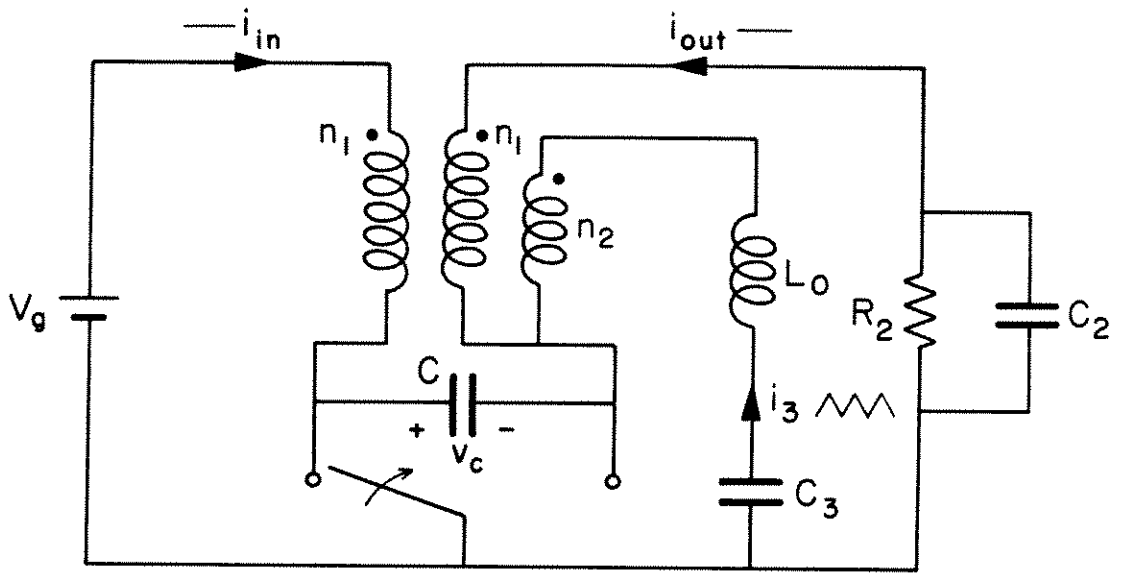

Fig. 3.6 Matching inductor L_0 in third winding with step down fraction $F = n_2/n_1$ sinks the ripple current from the coupled inductor.

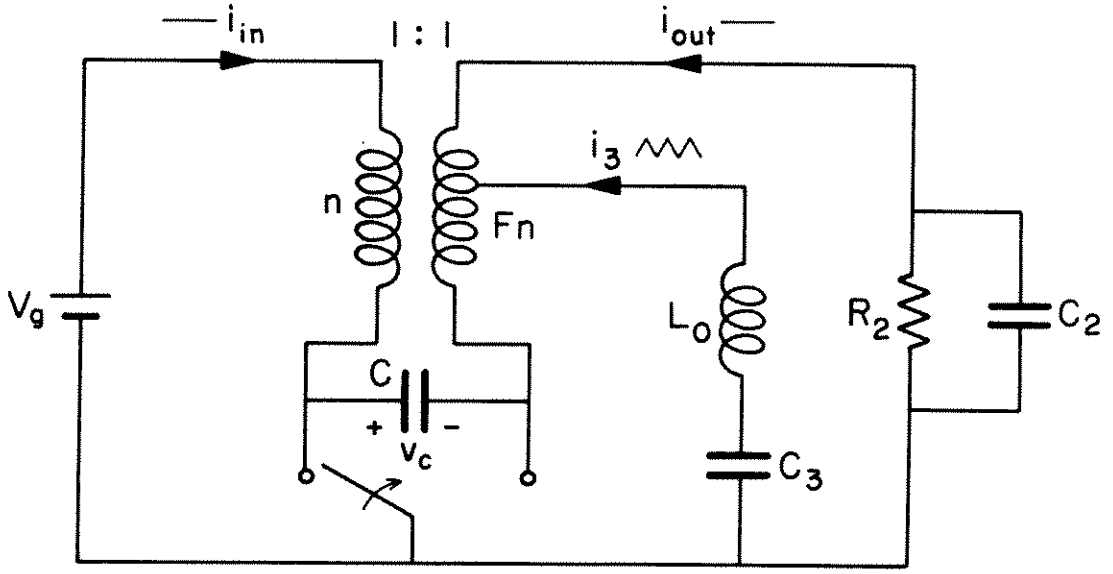

Fig. 3.7 Application of the impedance matching technique using an electrical tap at turns fraction F to absorb the inductive ripple current.

configuration. As before L_0 is determined in conjunction with $F = n_2/n_1$ by (3.12). Also C and C_3 are large enough so that their voltages are essentially constant. In the circuit of Fig. 3.6 all of the in phase $n\tilde{\phi}/L_1$ ripple will flow in the third winding with the sum current into the other two dots showing "zero" ac component of ripple.

Looking at Fig. 3.6 one realizes that the third winding here is superfluous and that an equivalent condition can be obtained by tapping the secondary (or primary) of the coupled inductor. Figure 3.7 shows such an improved topology.

When one builds circuits of the types shown in Figs. 3.6 and 3.7 it can be observed experimentally that $(\tilde{i}_{in} + \tilde{i}_{out})$ shows zero $n\tilde{\phi}/L$ ripple, that is the in-phase current ripple may be removed entirely by application of the tap inductance. However, out-of-phase oscillations of i_{in} and i_{out} are not prevented by any circuit impedance and in practice do occur as a result of component nonidealities. Since the impedance matching and division techniques are compatible, the out-of-phase ripple can be reduced by impedance in the input and/or output windings. One is again faced with the possibility of having to apply inductors which must stand dc bias. If the converter is being used as a voltage source operating from a nominal input voltage, then i_{in} and i_{out} have a fixed relationship. Consideration of 100% efficiency implies $V_g\ i_{in} = V\ i_{out}$ and shows that the currents are related precisely in this special case. Since actual converter configurations can have nearly 100% efficiency, or an estimatable lower efficiency, then an out-of-phase filter may be designed for the circuit in such a manner that

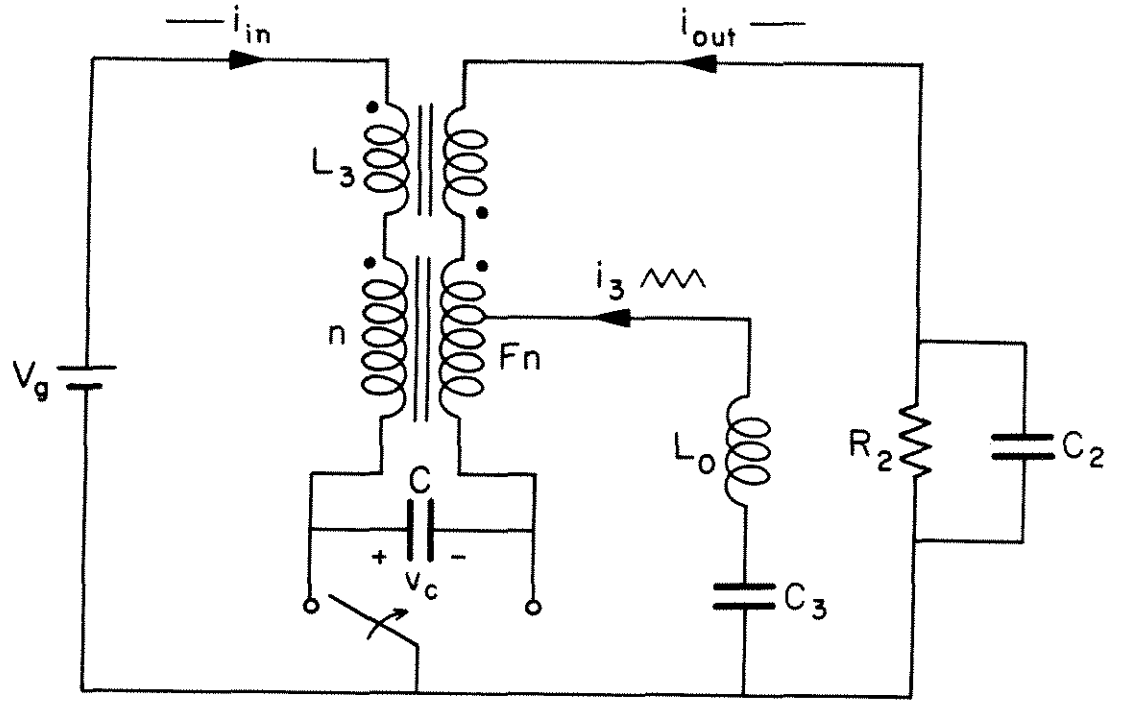

Fig. 3.8 Simultaneous application of impedance division and matching techniques eliminates both in-phase and out-of-phase ripple without using dc biased inductors.

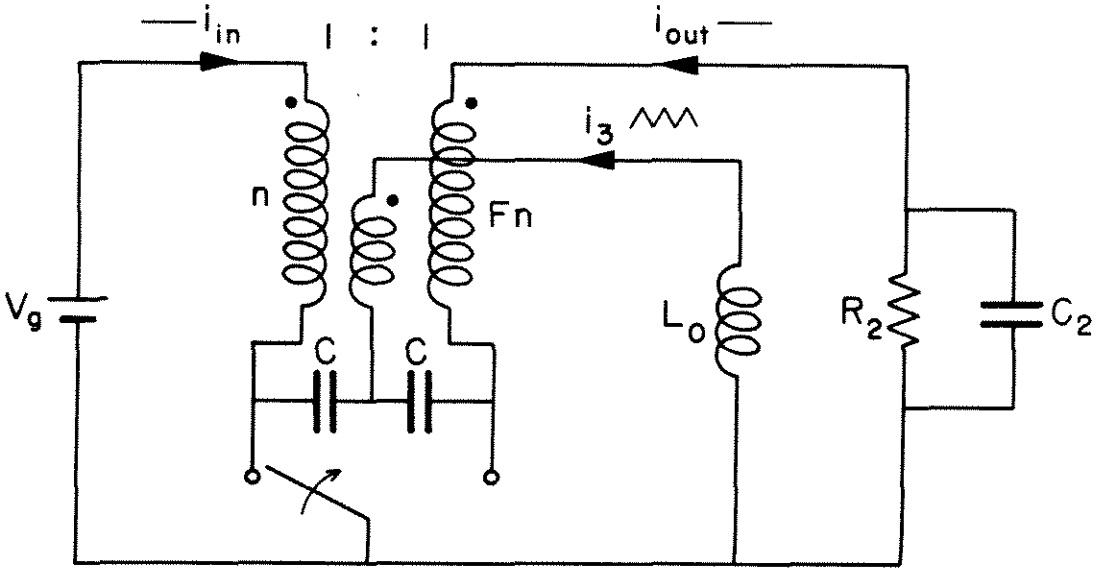

Fig. 3.9 Alternative implementation of matching condition to eliminate external current ripple utilizes split energy transfer capacitor and a magnetic tap at turns fraction F on the coupled inductor.

it stands a minimal dc bias. Figure 3.8 shows such a configuration.

If one reexamines Fig. 3.6 a possible circuit topology manipulation may come to mind. The blocking capacitor C_3 may be used to share the duties of the energy transfer capacitor. Figure 3.9 shows this split-capacitor zero-ripple topology. This configuration has the third (possibly small) magnetic tap winding in a similar position to the isolation transformer windings as shown in Fig. 1.6. Note however, that this winding is not an isolation winding, and could not be with the unequal turns ratio. Further the inductor L_0 would be subjected to attempted square wave current excitation which would disrupt the converter operation and destroy components. Of course a tap could be placed on the isolation transformer, and a configuration equivalent to Fig. 3.9 realized with only the addition of the ac choke L_0.

3.3 Demonstration circuit

A demonstration circuit was constructed in the configuration of Fig. 3.9 with the split capacitor. Figure 3.10 is a circuit diagram of this demonstrator with actual component values indicated. The circuit exhibits 0.2% rms output ripple when L_0 is adjusted to L/4 in accordance with F = 1/2. When L_0 is maladjusted, the ripple visible on the input or output may be made to appear with positive or negative slope. As mentioned earlier, an out-of-phase choke is included in the circuit to prevent $(i_{in} - i_{out})$ ripple spurred by circuit nonidealities.

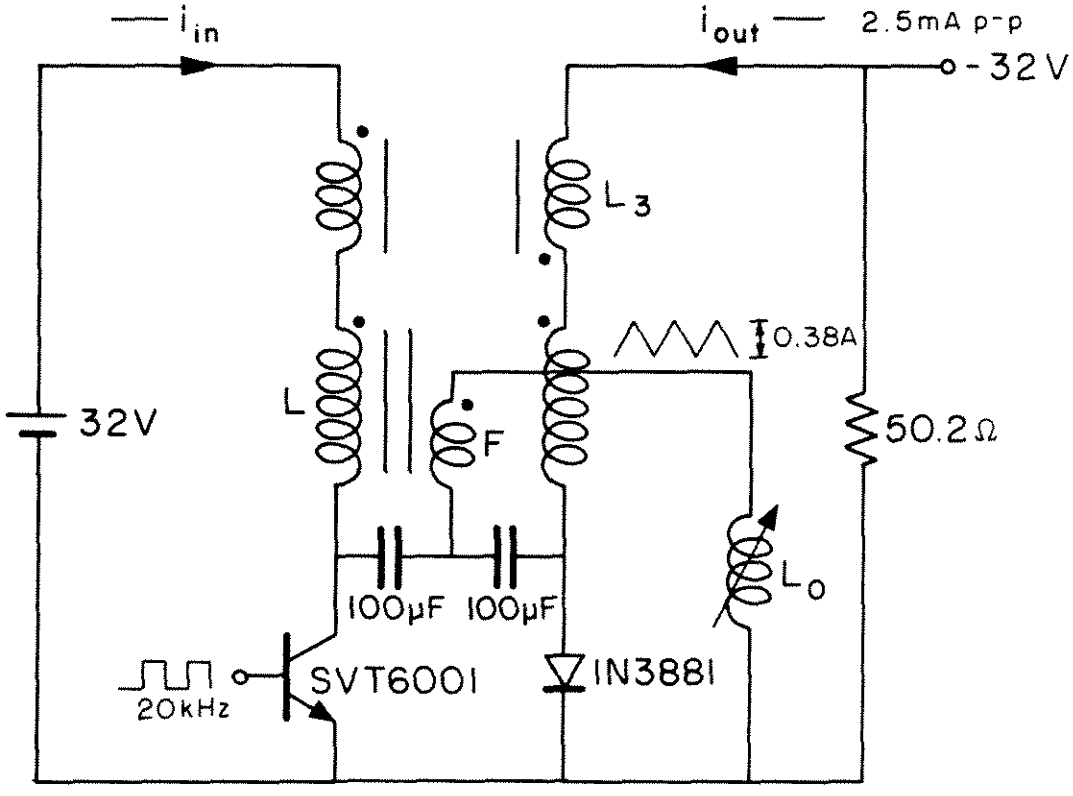

Fig. 3.10 *Zero ripple demonstration circuit*

L = 2.24 mH on Magnetics Inc. square permalloy 80 core with 170 turns #23 AWG and 0.13" air gap.

L_0 = 0.56 mH on Ferroxcube 1811PA2503B7 pot core with 47 turns #26 AWG.

L_3 = 7.4 mH on Arnold Engineering CL-3 c-cores of 0.002" 3% silicon iron.

3.4 Review

In this chapter the basic models developed in Chapter 2 were extended to include an arbitrary turns ratio on the coupled inductor. It was found that an appropriate inductive impedance in a winding with a turns ratio less than unity could serve as a sink for the $n\phi/L$ ripple that exists in the coupled-inductor windings. Novel features of this technique are that the ripple is made to flow into a high impedance by means of a matching condition between turns ratio and the winding inductance. If the matching condition is perturbed, positive or negative polarity ripple currents are observed on the converter input and/or output. A principal advantage sported by some of the topologies using the impedance matching technique is that the ripple may be diverted from the input and output ports of the converter without using dc biased inductors as was necessary when using the impedance division principle. Equally as important for practical considerations, the developments of this chapter were found to be compatible with the techniques of the preceding chapter and were used in conjunction for practical demonstration purposes.

Thus far all the work has been concerned with the coupled-inductor Ćuk converter. The results have been so encouraging with this topology that one may be stimulated to try to extend the principles perceived to alternative configurations.

CHAPTER 4

UNCOUPLED ZERO-RIPPLE CONFIGURATIONS

The preceding chapter developed techniques for demonstrating the zero-ripple phenomenon in the coupled-inductor Ćuk converter. That is, topologies were realized which exhibit ripple characteristics continuously adjustable from positive to negative slope with essentially a "zero-ripple" condition in between. Thus far the analysis has been solely concerned with the coupled-inductor converter's ripple behavior, which now may be explained and exploited in a number of ways. One is naturally led to extend the results of the previous chapters to include other converter topologies if possible. In this chapter it is found that the negative inductance effect, and hence the zero ripple condition, may be demonstrated with any of the basic converters that have a nonpulsating current waveform at the port of interest. The basic Ćuk converter without coupled inductors has nonpulsating currents at both input and output, and as such may be made to exhibit zero ripple at both ports. Of the several new ways suggested for making such a veritable dc-to-dc converter, one is selected and used for demonstration purposes.

The results of this chapter not only lead to several new and useful zero-ripple configurations but also identify a particular arrangement of elements that exhibits the negative inductance effect without the complication of a switched topology. The new filter first seen in this chapter will be the subject of more precise analysis in the next chapter, which will add even further refinements to the subject of ripple attenuation.

4.1 The uncoupled-inductor converter

The development of the coupled-inductor new converter was spawned by the realization that the voltage excitation waveforms on both inductors of the uncoupled version were identical [3]. Since the uncoupled version has strong similarities to the coupled-inductor converter one may naturally inquire whether similar techniques of ripple suppression are applicable to the basic new converter. In pursuit of the answer to this question, one may examine the circuit of Fig. 4.1 to see what useful parallels exist with the coupled-inductor version. A cursory examination of Fig. 4.1 reveals that when the inductors are not coupled the ac properties of the input and output currents are independent. Thus it should be manifest that the impedance division principle and the accompanying models do not apply to the basic new converter. However, knowledge that the voltage waveforms on the two inductors are identical to the waveform present on the coupled inductor, and the fact that any inductor can be viewed as an autotransformer leads one to consider the possibility of applying the impedance matching technique to the inductors of the basic new converter.

Consider the new converter of Fig. 4.1 with the tap point on the input inductor at tap fraction F as shown. The voltage v_t present at the tap point is approximately a square wave fluctuating between FV_g and $FV_g + (1 - F)v_c$ as illustrated in Fig. 4.2. Again the assumption of constant capacitor voltage is needed to justify the square wave approximation to the tap voltage waveform. The constant value v_c will assume is essentially $V_g - V$ so the tap waveform may be reformulated as

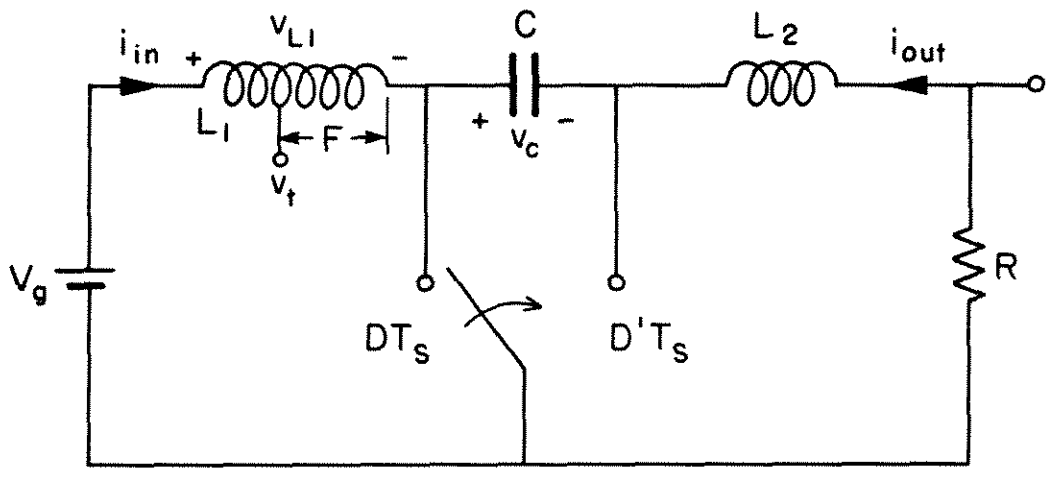

Fig. 4.1 Basic Ćuk converter with tap point on input inductor.

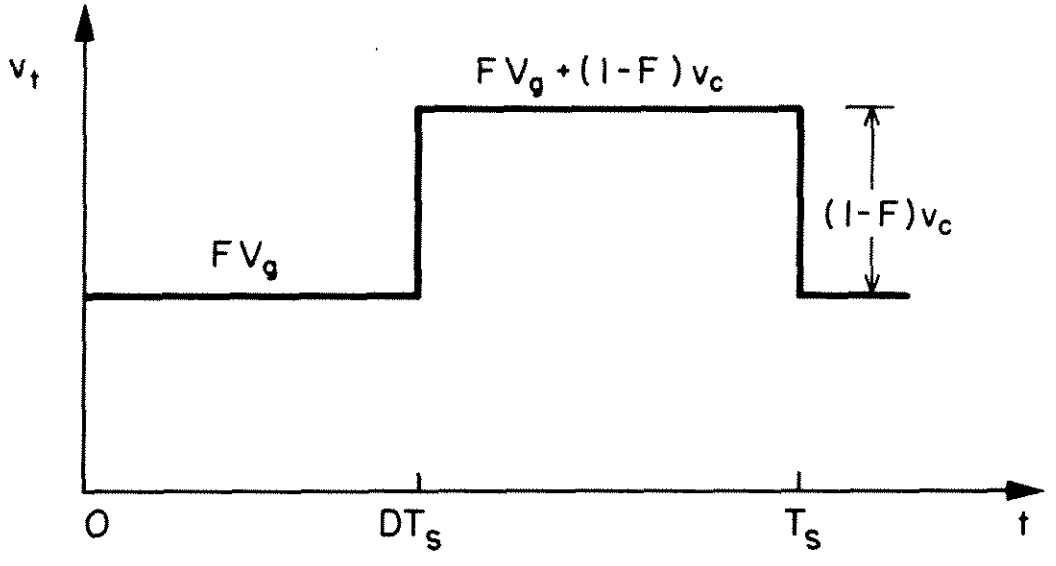

Fig. 4.2 Inductor tap voltage waveform with dc bias evident.

in Fig. 4.3. The voltage v_{L1} exciting current in the inductor is also well approximated by a square wave as shown in Fig. 4.4. Note that v_{L1} and v_t have 180° phase difference and that their ac magnitudes are v_c and $(1 - F)\, v_c$ respectively. If the ac component of the tap voltage in Fig. 4.3 were impressed across an inductor L_0 then the current flowing out of that inductor (and into the tap point) would be in correct phase to satisfy the current ripple input requirements of L_1 excited by v_{L1}. From Fig. 4.1 one may ascertain that the dc value present at the tap must equal the source voltage since no dc blocking elements exist between the tap and the source. Thus to obtain only ac excitation from the tap point the dc source voltage must somehow be subtracted out. If the dc shift is by any means accomplished, one may then proceed to calculate the value of tap inductance that will effect a matching condition in this case. In order to satisfy the ripple current requirements of L_1 at the tap point, a current "injected" there should be 1/F times the current ripple normally flowing in i_{in}. Equivalently from Figs. 4.3 and 4.4 we desire that the value of L_0 be such that

$$\frac{(1 - F)v_c}{L_0} = \frac{1}{F}\frac{v_c}{L_1} \tag{4.1}$$

so that the current flowing in L_0 would be a source of ripple current for L_1 of appropriate magnitude. The relation (4.1) is satisfied independently of v_c, or equivalently of the operating condition, if

$$\frac{L_0}{L_1} = F\,(1 - F) \tag{4.2}$$

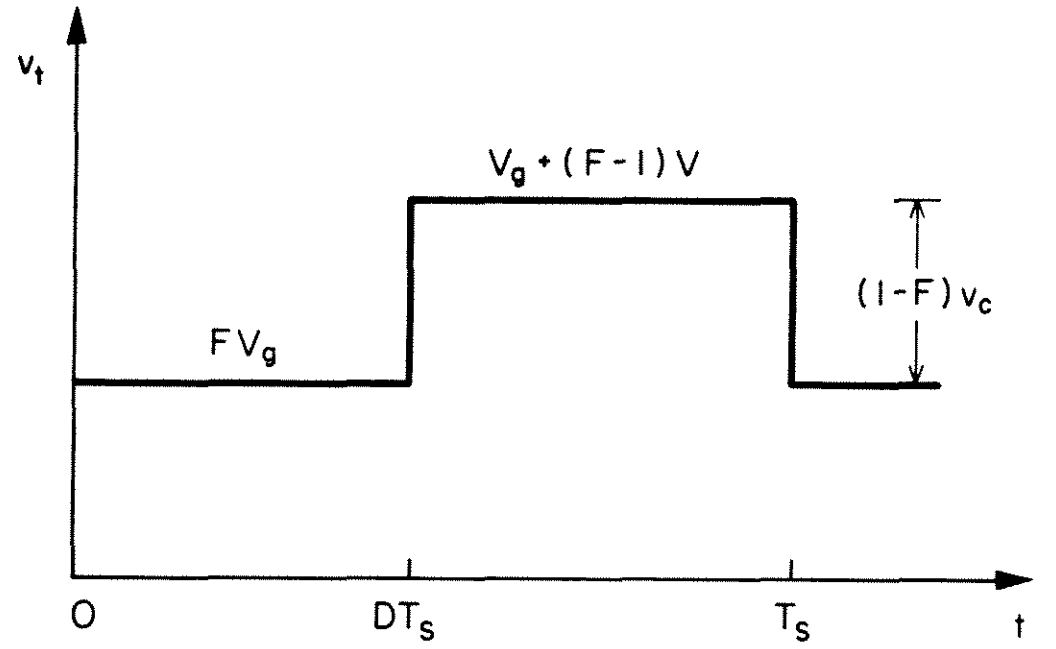

Fig. 4.3 Inductor tap voltage reformulated in terms of input and output voltages.

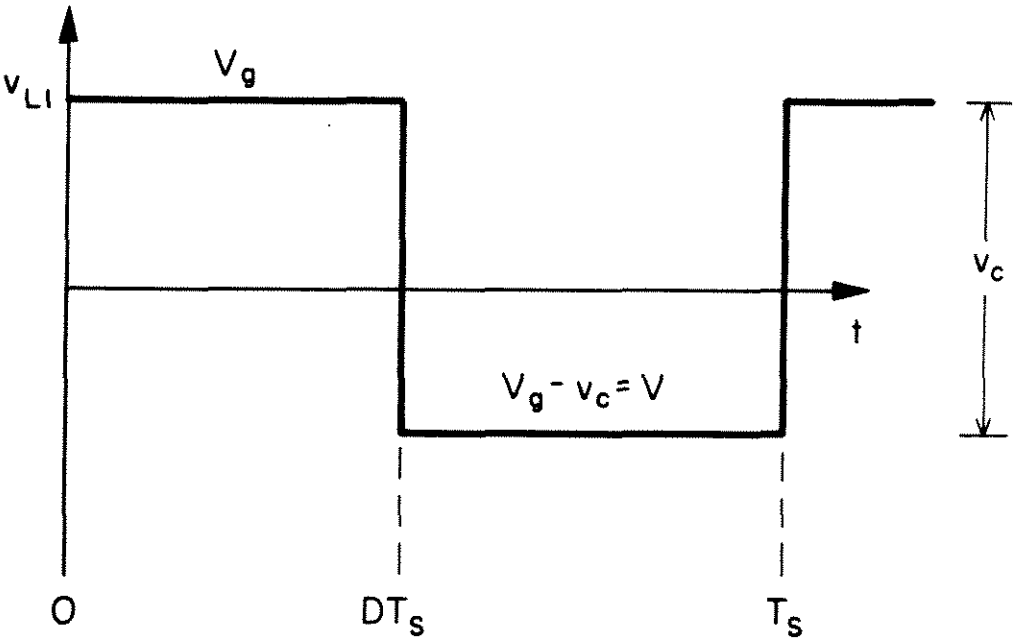

Fig. 4.4 Voltage waveform across the input inductor shown with no dc component in accordance with volt-second balance requirement.

Equation (4.2) is identical to the matching condition for the coupled inductor given in (3.12). This should not be surprising granted the similarity between the converters.

All that remains to be determined is how to locate L_0 such that it may feed current into the tap point and experience a voltage of $v_t - V_g$, the tap voltage with dc bias removed. There are several ways of achieving this end. One obvious way is shown in Fig. 4.5. The ripple normally present on i_{in} now will flow through L_0 magnified by 1/F. This configuration is useless since the ripple is still drawn from the source and its magnitude is even increased, circumstances we hope to avoid. Instead of returning L_0 to the source one may employ a blocking capacitor to ground as shown in Fig. 4.6. The average voltage across C_0 is V_g so the voltage across L_0 is the desired $v_t - V_g$ and the ripple current in L_1 will flow into the tap point and not out of the source. Again the assumption is that C_0 is large enough so that its voltage is essentially constant. The derivation of the configuration that removes the output current ripple is quite similar to that just preceding, and the result is the same. It is then possible to envision a topology based on the uncoupled-inductor new converter that will exhibit the zero ripple or negative inductance properties on both the input and the output currents. Figure 4.7 illustrates one basic approach. The circuit of Fig. 4.7 has been constructed and found to exhibit the zero ripple properties at input and output. Maladjustment of L_{01} or L_{02} can cause positive or negative ripple to appear at the corresponding port. Several extensions of this configuration follow easily.

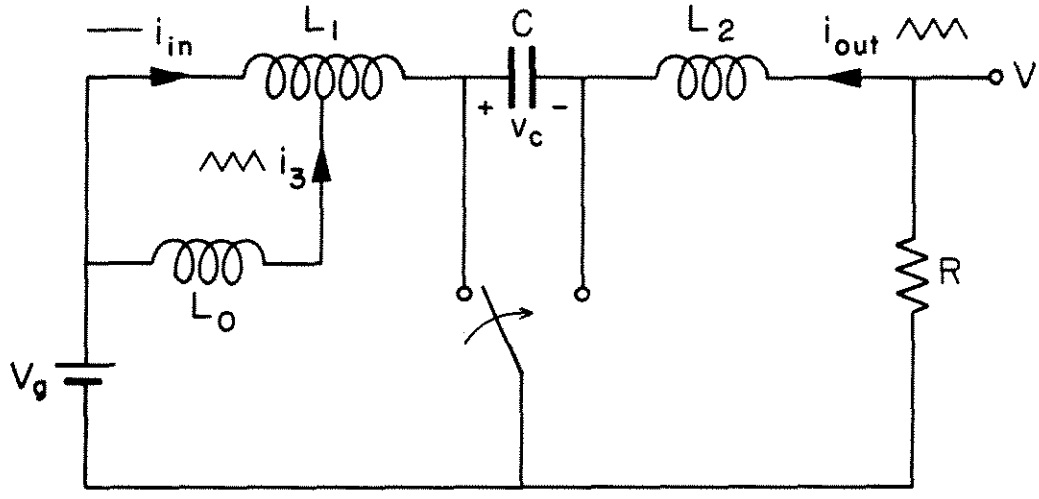

Fig. 4.5 Use of source voltage to remove dc bias from matching inductor returns ripple current to the source defeating the purpose of the impedance matching.

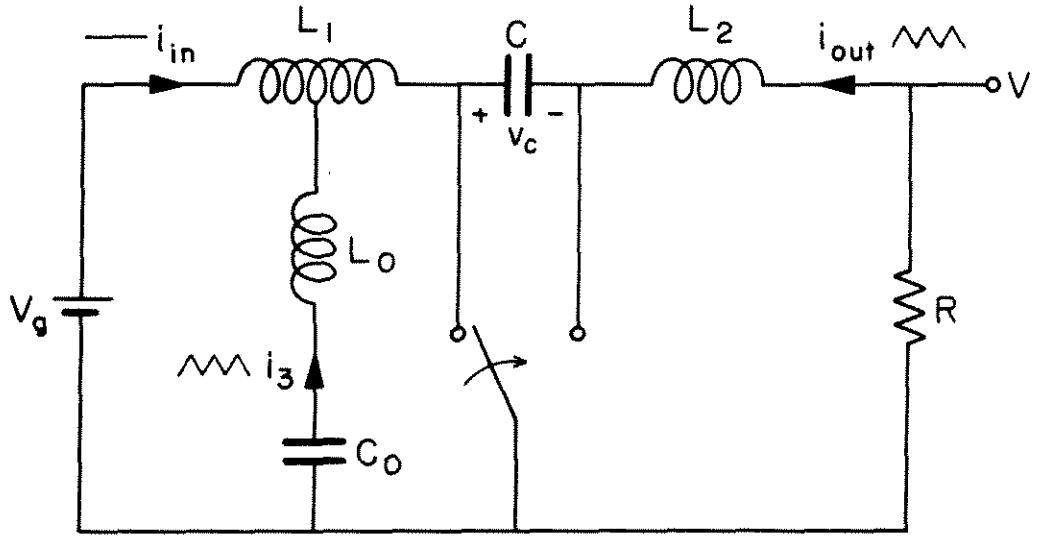

Fig. 4.6 A practical implementation of impedance matching to remove the input current ripple from the basic Ćuk converter relies on capacitor C_0 to maintain a voltage equal to V_g.

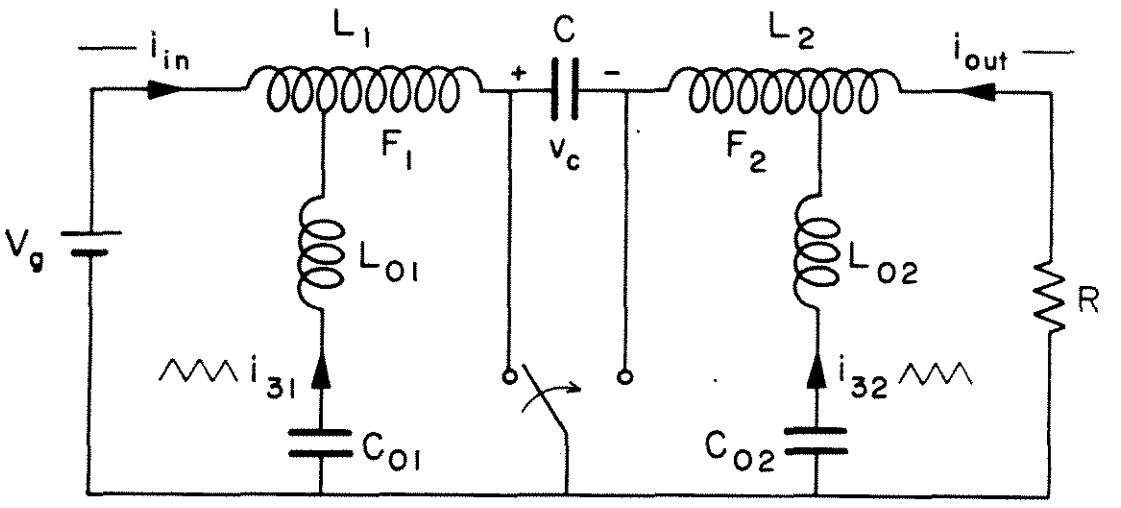

Fig. 4.7 Basic Ćuk converter with zero input and output current ripples.

It should be apparent that the boost-buck new converter in Fig. 4.7 can be "dissected" to yield a boost circuit and a buck circuit. Thus a boost circuit with only dc input current or a buck circuit with only dc output current can be envisioned. The problem remains with both of these circuits that one of the currents is pulsating, a circumstance often requiring external filtering.

The most fruitful extensions are those involving the new converter. The important step in conceiving some useful developments is to utilize the split capacitor concept [2] in conjunction with the notion of a "magnetic tap" on the input and output inductances. The basic idea is shown applied in the circuit of Fig. 4.8. Here the energy transfer capacitors C_1 and C_2 serve to remove dc bias from L_{01} and L_{02}. The electric tap of Fig. 4.7 is replaced with an additional, possibly small

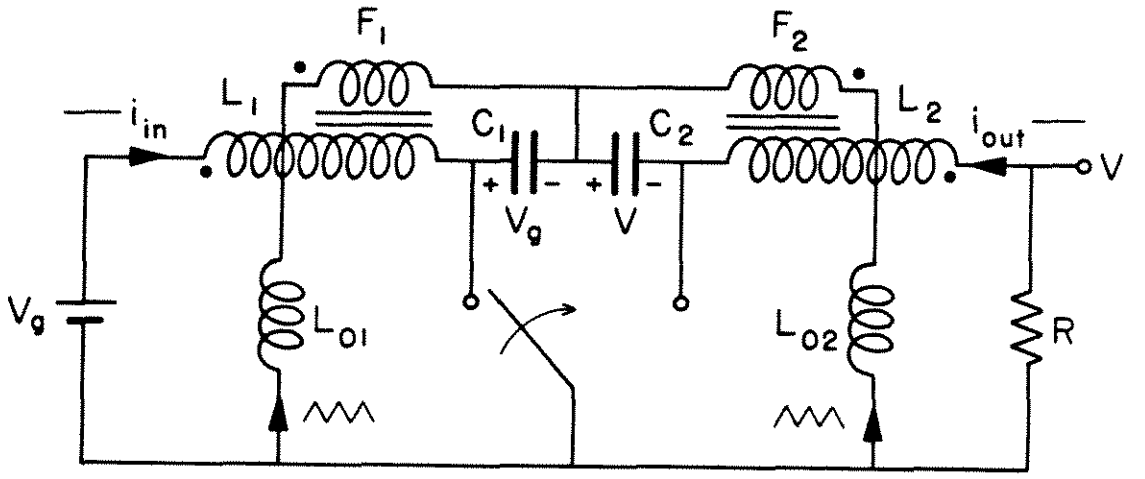

Fig. 4.8 Split-capacitor zero-ripple topology utilizes magnetic taps on the input and output inductors of the basic Ćuk converter.

cross section, winding which may be viewed as a magnetic tap. Two capacitors are eliminated at the expense of two small windings. The circuit of Fig. 4.8 has been constructed and found to perform well. An alternative to the circuit of Fig. 4.8 involves coalescing L_{01} and L_{02} into a single L_0 at the split capacitor whose value is given by $L_0 = L_{01} \,//\, L_{02}$. Experimentally this option is found to be less effective since independent nulling of the input and output current is sacrificed.

For the final example modification to the circuit of Fig. 4.7, a demonstration circuit was constructed.

4.2 Demonstration circuit

The demonstration circuit is a natural outgrowth of the split-capacitor zero-ripple configuration. The transformer isolated versions of the new converter all have a split capacitor to accommodate the isolation transformer. With minimal penalty in terms of parts count and complexity the isolating uncoupled-inductor converter is rendered zero-ripple through use of magnetic taps as shown in Fig. 4.9. The demonstration circuit was found to give excellent ripple performance having less than 0.1% rms current ripple.

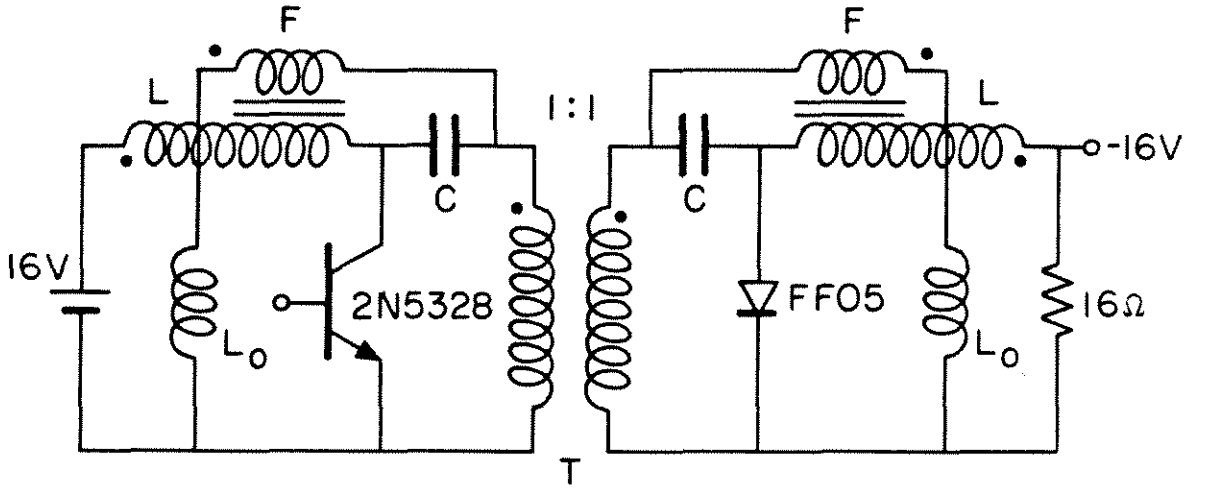

Fig. 4.9 Uncoupled-inductor zero-ripple demonstrator circuit.

Switching frequency = 20 KHz

L = 2.29 mH L_0 = 573 μH

F = 0.5 C = 900 μF

4.3 Review

The zero-ripple and negative-inductance phenomena are found to exist in other topologies than the coupled-inductor Ćuk converter. The basic Ćuk converter, the boost, and the buck all can be made to show negative inductance and hence zero ripple. Of these three only the Ćuk converter lends itself to the possibility of zero input and output ripple. Three practical methods of arriving at this condition are presented concluding with a specific circuit example.

CHAPTER 5

THE NEW FILTER

In the previous chapter several topologies with the zero-ripple properties were introduced. A fundamental building block for these new configurations is a tapped inductance with an LC network from the tap to ground. Previously, for the sake of convenience and ease of understanding the operation of the zero-ripple topologies, constant capacitor voltage assumptions have been made. In this chapter the analysis of the new filter gains added accuracy by including the effect of fluctuating capacitor voltage. Since the tapped-inductor configuration has no switched elements it is particularly amenable to linear analysis and may readily be described in the frequency domain via its state-space model, including the capacitor voltage as a state. The power of this precise description of the new filter is conspicuous in its ability to explain the negative inductance effect. Moreover, the designer's ability to synthesize in the Laplace transform domain is supported by a great wealth of classical design technique. Some of these methods are used to design a third-order elliptic-function filter with its complex-conjugate zero pair at the switching frequency. Example circuits are built and tested in the laboratory to show that the ripple attenuation can be extreme even for relatively small filter elements. To illustrate the sharp cutoff of the elliptic, a switching audio amplifier is constructed with the switching frequency just two octaves above the audio band. The laboratory tests on this circuit clearly indicate the utmost selectivity of

this electric power filter in rejecting switching noise while allowing audio frequencies to pass.

The development of the elliptic filter in a form suitable for power processing applications culminates the effort of Part 1 of this work. The relative merits of the techniques developed for improving converter noise characteristics will be discussed in the review section for this chapter.

5.1 State-space analysis

The new filter is an outgrowth of the impedance matching technique which has been discussed in various forms in Chapters 3 and 4. However in Chapter 4 the zero ripple filtering effect was realized with constant topology components. That is, the elements of the new filter were in a fixed physical relationship to one another with none of the components being switched in and out by the converter operation. Thus, ripple analysis on such filters may be performed by classical techniques. The output section of the circuit of Fig. 4.7 is a non-switched zero-ripple filter that here will be subjected to analysis.

Consider the zero-ripple filter with an ac voltage generator on its input as depicted in Fig. 5.1. In order to proceed with the analysis of Fig. 5.1 it is convenient to choose a suitable equivalent circuit model with state variables identified. The tapped inductor can be modeled as an ideal transformer and parasitic resistances in the circuit ignored without loss of accuracy to the extent that fundamental understanding of the circuit operation will be sacrificed. With these

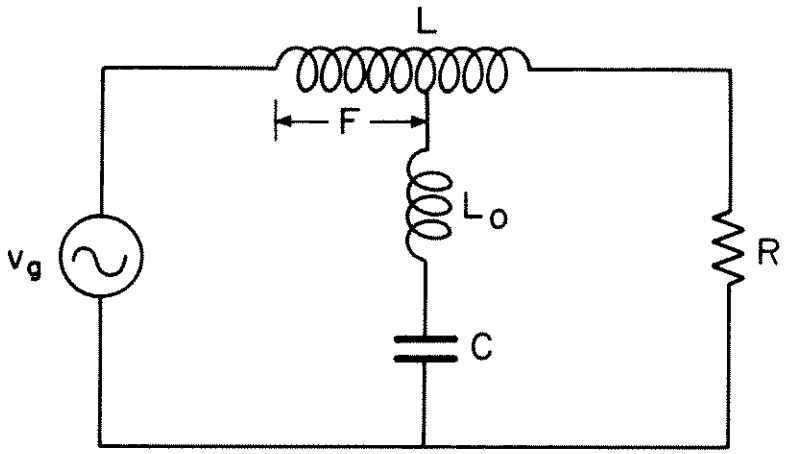

Fig. 5.1 The new power processing filter shown with ac voltage source excitation.

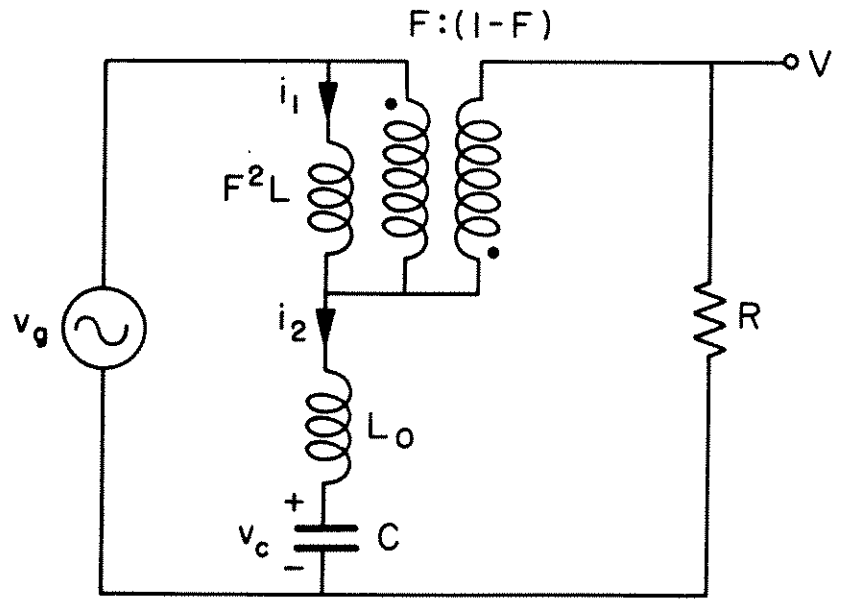

Fig. 5.2 A state-variable model for the new filter represents the power inductor as an inverting transformer.

assumptions an appropriate state-variable model of the new filter is shown in Fig. 5.2. Notice that the tapped inductor is replaced by an inverting F:(1-F) transformer with magnetizing inductance F^2L. The choice of states is not unique but in this case a convenient selection is the transformer magnetizing current i_1, the tap inductor current i_2, and the blocking capacitor voltage v_c. With this choice the first order vector differential equation describing the system dynamics may be written by inspection of Fig. 5.2 as

$$\frac{d}{dt}\begin{bmatrix} i_1 \\ i_2 \\ v_c \end{bmatrix} = \begin{bmatrix} -\frac{R}{L} & \frac{R}{L} & 0 \\ \frac{F^2R}{L_0} & -\frac{F^2R}{L_0} & -\frac{1}{L_0} \\ 0 & \frac{1}{C} & 0 \end{bmatrix} \begin{bmatrix} i_1 \\ i_2 \\ v_c \end{bmatrix} + \begin{bmatrix} \frac{1}{FL} \\ \frac{1-F}{L_0} \\ 0 \end{bmatrix} v_g \qquad (5.1)$$

Equation (5.1) is of the standard form $\dot{x} = Ax + bv_g$ and as such is readily solved by Laplace transform. The general steady-state solution is given in terms of the transform variable s as

$$x(s) = (sI - A)^{-1}b\, v_g(s) \qquad (5.2)$$

As it is sufficient to know the filter response for sinusoidal excitations of all frequencies $v_g(s)$ may be taken to be unity, the transform of the impulse function which has unity strength for all frequencies. Then x(s) with $s = j\omega$ will indicate the magnitude and phase of the state-vector response to a sinusoidal input with radian frequency ω. Knowledge of the frequency response is tantamount to knowledge of the filter response to any function that possesses an eigenfunction expansion in sines and

cosines. Since we are ultimately interested in the response of the system to square-wave switching excitation with its well-known Fourier series expansion, a frequency response analysis is entirely adequate for present purposes. However, in this case the transfer function of interest is $v/v_g(s)$ and v is not a state variable but a linear combination of state variables chosen. Thus the answer sought is not given directly by (5.1), but instead may be written as

$$\frac{v}{v_g}(s) = h^T(sI-A)^{-1}b \tag{5.3}$$

where $h^T = [FR, -FR, 0]$, and T indicates transpose. Equation (5.3) shows that the steady-state solutions to system transfer functions are available from the state equations (5.1) by straightforward matrix manipulations provided h is known and $|sI-A| \neq 0$ ($|A|$ indicates the determinant of A). In accordance with standard technique, (5.3) may be expanded as

$$\frac{v}{v_g}(s) = \frac{h^T Cof^T(sI-A)b}{|sI-A|} \tag{5.4}$$

where Cof(sI-A) is the matrix of cofactors of sI-A. The desired transfer function is obtained from (5.4). The expansion and subsequent coalescing of terms in (5.4) is a few pages of simple algebra resulting in

$$\frac{v}{v_g}(s) = \frac{(L_0 - F[1-F]L)Cs^2 + 1}{\frac{LL_0C}{R}s^3 + (L_0 + F^2L)Cs^2 + \frac{L}{R}s + 1} \tag{5.5}$$

One may notice that the leading coefficient in the numerator of (5.5) may be positive, negative or zero depending on the values of L_0, F and L. For sufficiently large s the transfer function approaches

$$\left.\frac{v}{v_g}(s)\right|_{s \to \infty} = \frac{(L_0 - F(1-F)L)R}{LL_0 s} \tag{5.6}$$

The high frequency response of the system may appear as an integrator with or without an additional 180° phase shift depending upon the sign of the numerator. This explains the observed negative inductance effect in the new filter.

When the leading coefficient in the numerator of equation (5.5) is zero, the maximum high frequency attenuation is obtained. The criterion is independent of R and C and is given by

$$\frac{L_0}{L} = F(1-F) \tag{5.7}$$

precisely the matching condition first expressed in (3.12). Figure 5.3 is a sketch of the normalized tap inductor versus the tap fraction. Notice that for F = 0.5 the value of L_0 is maximized at 0.25 L. If one rewrites equation (5.5) with L_0 determined by (5.7) as sketched in Fig. 5.3, the result is

$$\frac{v}{v_g}(s) = \frac{1}{\frac{F(1-F)L^2C}{R}\, s^3 + FLCs^2 + \frac{L}{R}s + 1} \tag{5.8}$$

Equation (5.8) shows that ideally, when the matching condition is in effect, the high frequency ripple attenuation is third order and that the term "zero ripple" is somewhat of a misnomer. The leading coefficient in

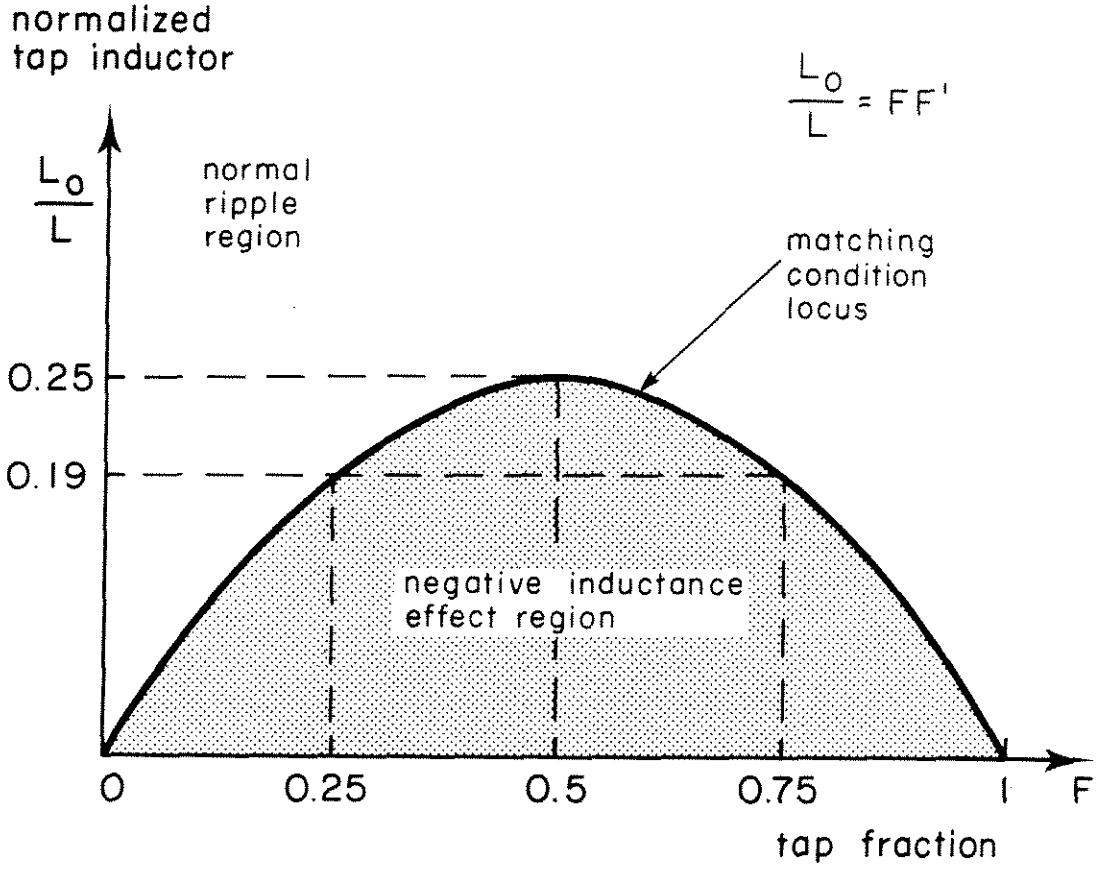

Fig. 5.3 Sketch of normalized tap inductor versus tap fraction showing the matching condition and areas where mismatch produces positive or negative ripple sense power inductor current.

the denominator is maximized when F(1-F) is, and thus the tap fraction of 0.5 leads to the greatest high frequency attenuation corresponding to the largest matching L_0 for a given choice of L.

Any hardware realization of the new filter of Fig. 5.1 will be affected by component non-idealities. One parasitic worthy of consideration is the resistance in the tap impedance comprised of the capacitor's esr and the inductor's series resistance. For convenience these two resistances may be added and attributed in name to the capacitor esr by labelling the resistance R_c. With R_c placed in series with L_0 and C in the state-variable model of Fig. 5.2, the expression equivalent to (5.5) obtained in a like manner is

$$\frac{v}{v_g}(s) = \frac{\left[L_0 - F(1-F)L\right]Cs^2 + R_cCs + 1}{\frac{LL_0C}{R}s^3 + \left[L_0 + \left(\frac{R_c}{R} + F^2\right)L\right]Cs^2 + \left(R_cC + \frac{L}{R}\right)s + 1} \tag{5.9}$$

which becomes

$$\frac{v}{v_g}(s) = \frac{R_cCs + 1}{\frac{F(1-F)L^2C}{R}s^3 + \left(F + \frac{R_c}{R}\right)LCs^2 + \left(R_cC + \frac{L}{R}\right)s + 1} \tag{5.10}$$

when the matching condition is in effect. The presence of the zero in (5.10) indicates degraded high-frequency attenuation owing to the parasitics as one would expect. Equation (5.10) may be factored approximately as

$$\frac{v}{v_g}(s) = \frac{\tau_z s + 1}{(\tau_p s + 1)\left[\left(\frac{s}{\omega_o}\right)^2 + \frac{s}{\omega_o Q} + 1\right]} \tag{5.11}$$

where $\tau_z = R_c C$, $\tau_p = \frac{(1-F)L}{R}$, $\omega_o = \frac{1}{\sqrt{FLC}}$, and $Q = \sqrt{FLC}/(FL/R + R_c C)$. The approximate factoring is quite accurate when $R_c << R$ and $RC >> \tau_p$ or, equivalently, when the pole and zero break well after ω_o.

5.2 Experimental verification

Two configurations were subjected to laboratory frequency analysis. In the first circuit the pole and the zero nearly cancelled, while in the second the pole's time constant was approximately twice that of the zero. Figures 5.4 and 5.5 show the laboratory data indicated by dots alongside the predicted asymptotes. The asymptotes, and Q of the double break, are calculated by means of the equation (5.11) using the circuit element values indicated on the figures. For sake of completeness, the phase of the transfer functions was measured and included on the plots. It may be seen that there is a high degree of corellation between predicted and measured values, supporting the analysis and substantiating the accuracy and usefulness of the approximate factoring in (5.11) for these cases.

5.3 Enter the elliptic

Again with neglect of R_c, the filter transfer function zeroes may be obtained from equation (5.5) and are given by the values of s that satisfy

$$\left[L_0 - F(1-F)L\right]Cs^2 + 1 = 0 \qquad (5.12)$$

The zeros may be either real or imaginary depending on whether $L_0 - F(1-F)L$ is less than or greater than zero respectively. In either case the transmission zeroes are symmetric about the origin of the s-plane.

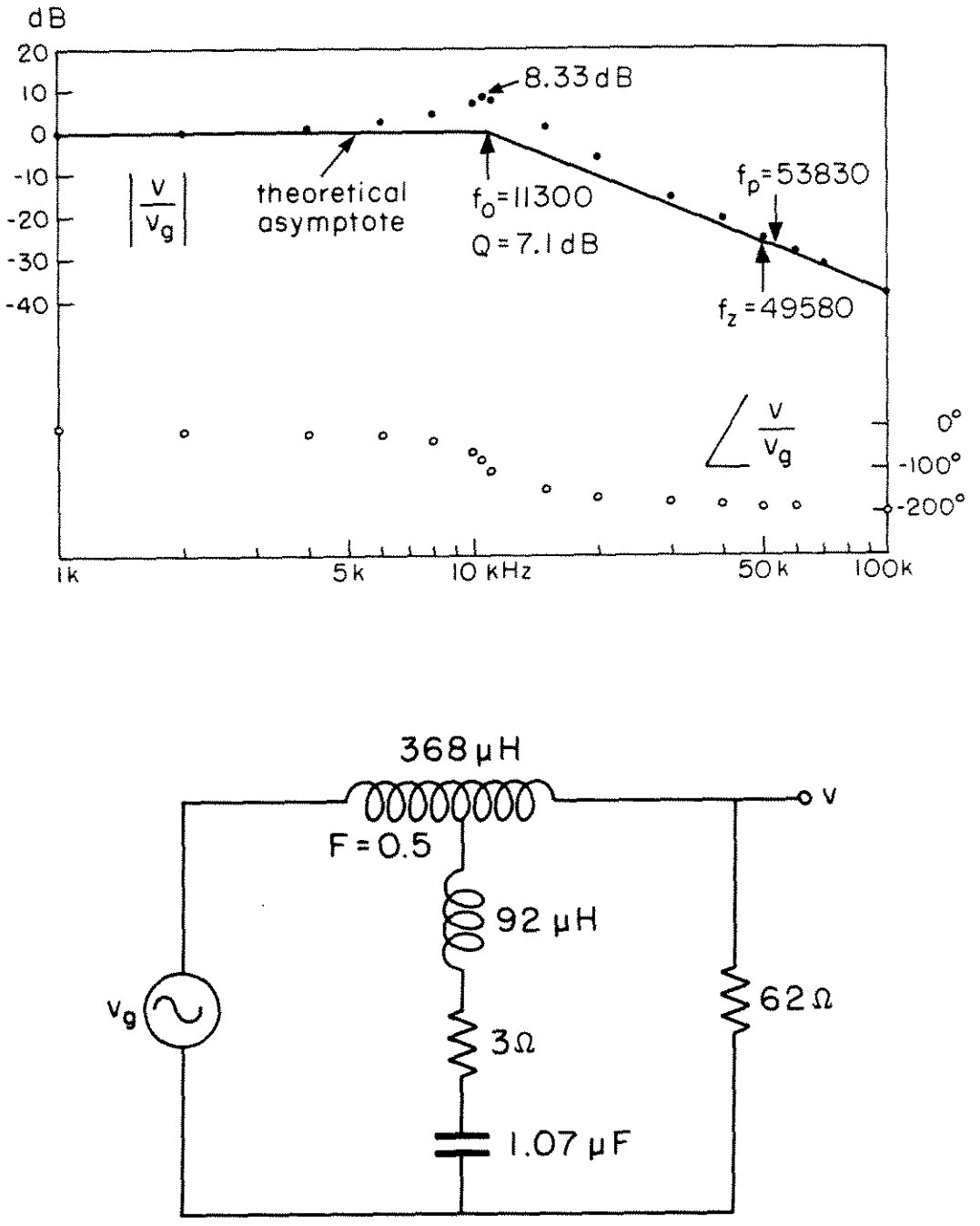

Fig. 5.4 A new filter configuration with its theoretical and empirical frequency response compared for a case of approximate pole-zero cancellation.

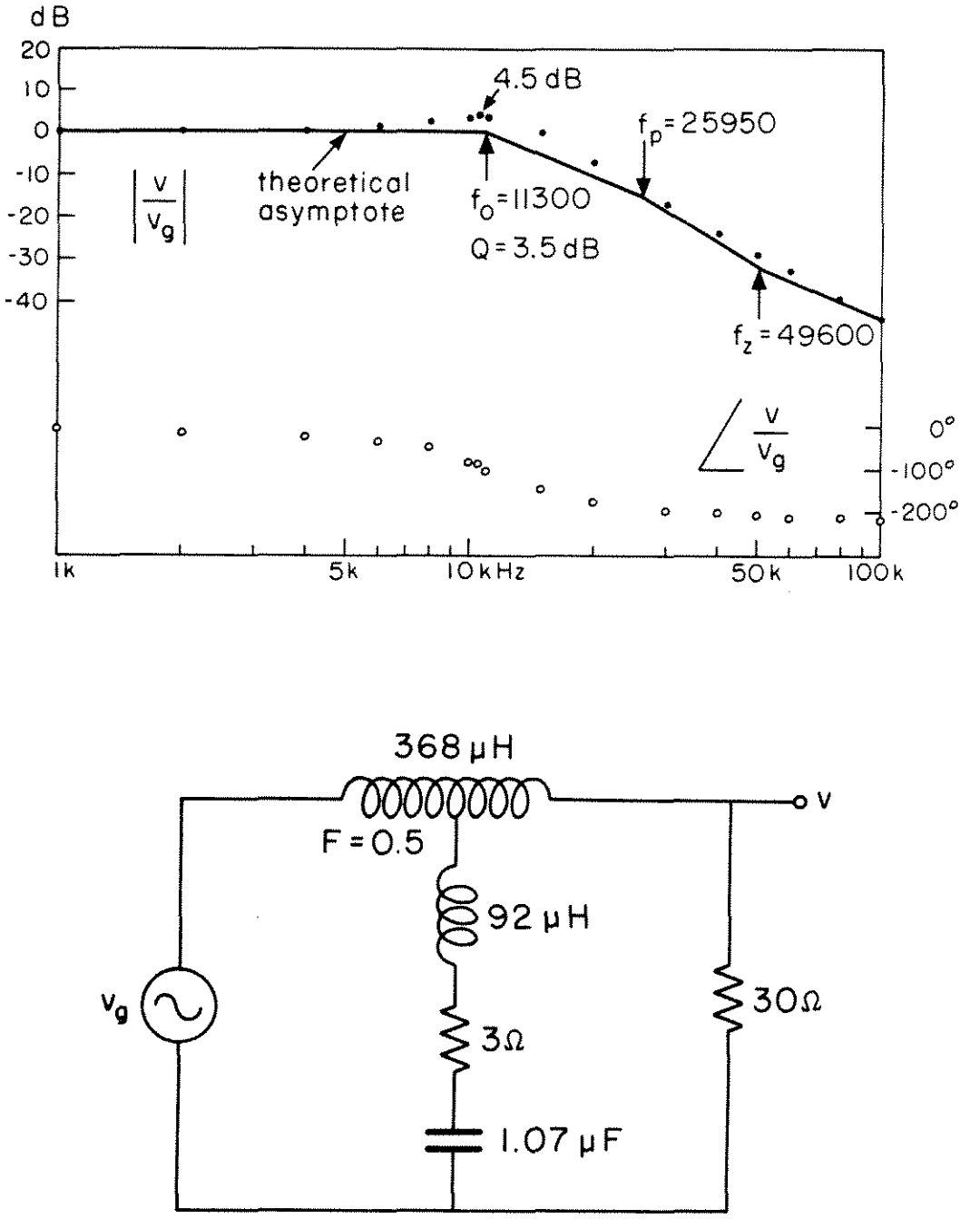

Fig. 5.5 A new filter configuration with experimental frequency response data shown by dots adjacent to the theoretical asymptote for a case with the pole and zero well-separated.

It can be seen that for the zeroes near the point at infinity the two situations differ in that the imaginary pair has no phase contribution, while the real pair produces 180° of phase. This provides an alternative view of the cause of the observed negative inductance effect in the new filter. By adjustment of L_0 about the matching value, two zeroes may be made to pass through the point at infinity from the imaginary axis to the real axis, changing the filter response from minimum phase to non-minimum phase with one zero in the right-half plane.

When the new filter is used in a switching dc-to-dc converter such as a buck converter, shown in Fig. 5.6, or in a switching dc-to-ac converter such as the switching audio amplifier shown in Fig. 5.7, it is often desired that the filter attenuate the fundamental component of the switching waveform as fully as possible. The previous derivation of the matching condition was postulated on the assumption that the capacitor voltages were constant, or equivalently, that the switching frequency was high compared to the system's natural break frequencies. In fact we know the form of the disturbance provided to the filter, and have more precise knowledge of the fundamental frequency than that it is high. Indeed, in absence of knowledge of the switching frequency the matching condition which provides the greatest attenuation at high frequencies gives the natural choice for the filter components. Knowledge of the switching frequency and the precise nature of the filter response, given in equation (5.5), allows the designer to make a more judicious choice of component values than might otherwise be selected.

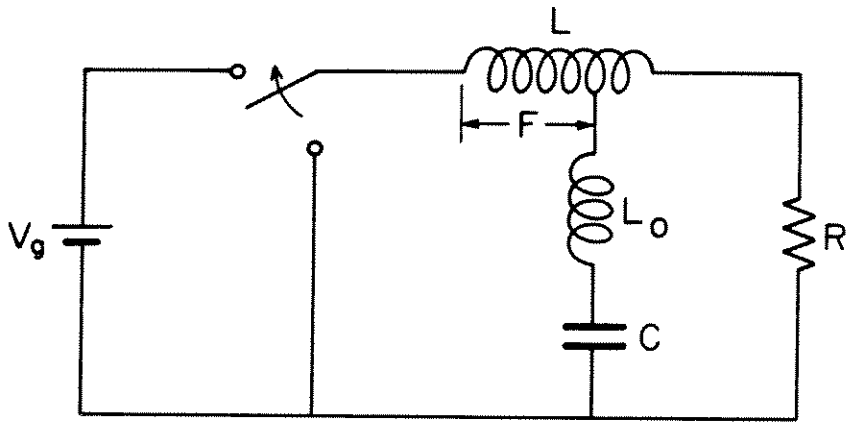

Fig. 5.6 New filter buck-type converter may be made to exhibit negative-inductance and hence zero-ripple behavior.

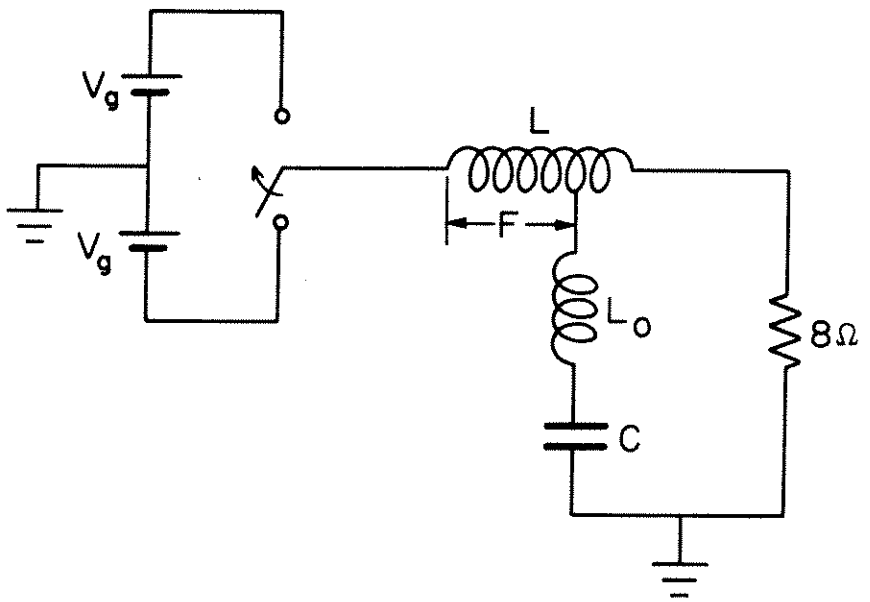

Fig. 5.7 A new filter buck-derived switching audio amplifier with an 8 Ω load representing the speaker.

When $L_0/L = F(1-F)$ we know that we obtain some sort of second or third order attenuation on the switching frequency depending on the circuit's parasitics. Equation (5.12) and the discussion call attention to the fact that if $L_0 - F(1-F)L$ is greater than zero the transfer function of (5.5) has complex conjugate zeroes on the imaginary axis. If there is a particular frequency we wish the filter to reject, the zero pair could be made to lie at $\pm j\omega$ where ω is the undesired frequency. To accomplish this one sets

$$\sqrt{(L_0 - F(1-F)L)C} = \frac{1}{\omega} \tag{5.13}$$

with $L_0 > F(1-F)L$. Then, at least to the extent that $R_c = 0$, the radian frequency at ω is entirely attenuated. Choice of ω to correspond to the switching frequency will provide nearly complete attenuation of the fundamental component of a switching square wave.

It is also desirable that higher harmonics from the switching are not passed to the load. In equation (5.5) it is plain that the transfer characteristic has 3 poles and 2 complex zeroes. This is similar to the s-plane locus for a third-order elliptic-function filter. Recall from filter theory that an elliptic filter has an equiripple pass and stop band transfer function which leads to the sharpest possible cutoff for a filter with a given order denominator. If the elliptic filter pole and zero locations are known then (5.5) gives rise to four equations in five unknowns, L, L_0, F, C and R. If the load R is known, then the ambiguity is resolved and the element values that make (5.5) the elliptic filter transfer function are uniquely specified. The new filter when properly

configured may approximate the sharp cutoff of the elliptic, and in addition may have complex conjugate zeroes at the fundamental excitation frequency. The sharp cutoff has the advantage of allowing the filter natural frequencies to be high, and hence the component values relatively small, and still maintain an acceptable stop band attenuation. The zeroes on the fundamental excitation frequency cause the filter to specifically discriminate against the switching waveform, further enhancing its performance.

A computer program was written to solve for the circuit element values for the new filter in its elliptic function form with specified passband ripple and transition bandwidth (see the Appendix). With 2 dB of passband frequency response fluctuation allowed from dc to 20 kHz, and the transition bandwidth such that the transmission zeroes are at 80 kHz, the circuit element values are those given in Fig. 5.8 accompanying the experimentally measured frequency response. Insight is gained into the relationship between the equiripple passband property and the sharpness of the cutoff by examination of the theoretical asymptotes sketched adjacent to the data points. There is a pole at 7560 Hz that causes the passband to drop a little more than 2 dB at 10 kHz. The transfer characteristic does not drop more because a resonant pole pair exists at 18,900 Hz which causes upward deviation from the asymptote plot in such a manner as to hold up the transfer function until the desired bandwidth of 20 kHz is reached. After 20 kHz the resonance drops off sharply, and simultaneously the attenuation from the low frequency pole is evidenced. In addition, the deviation from

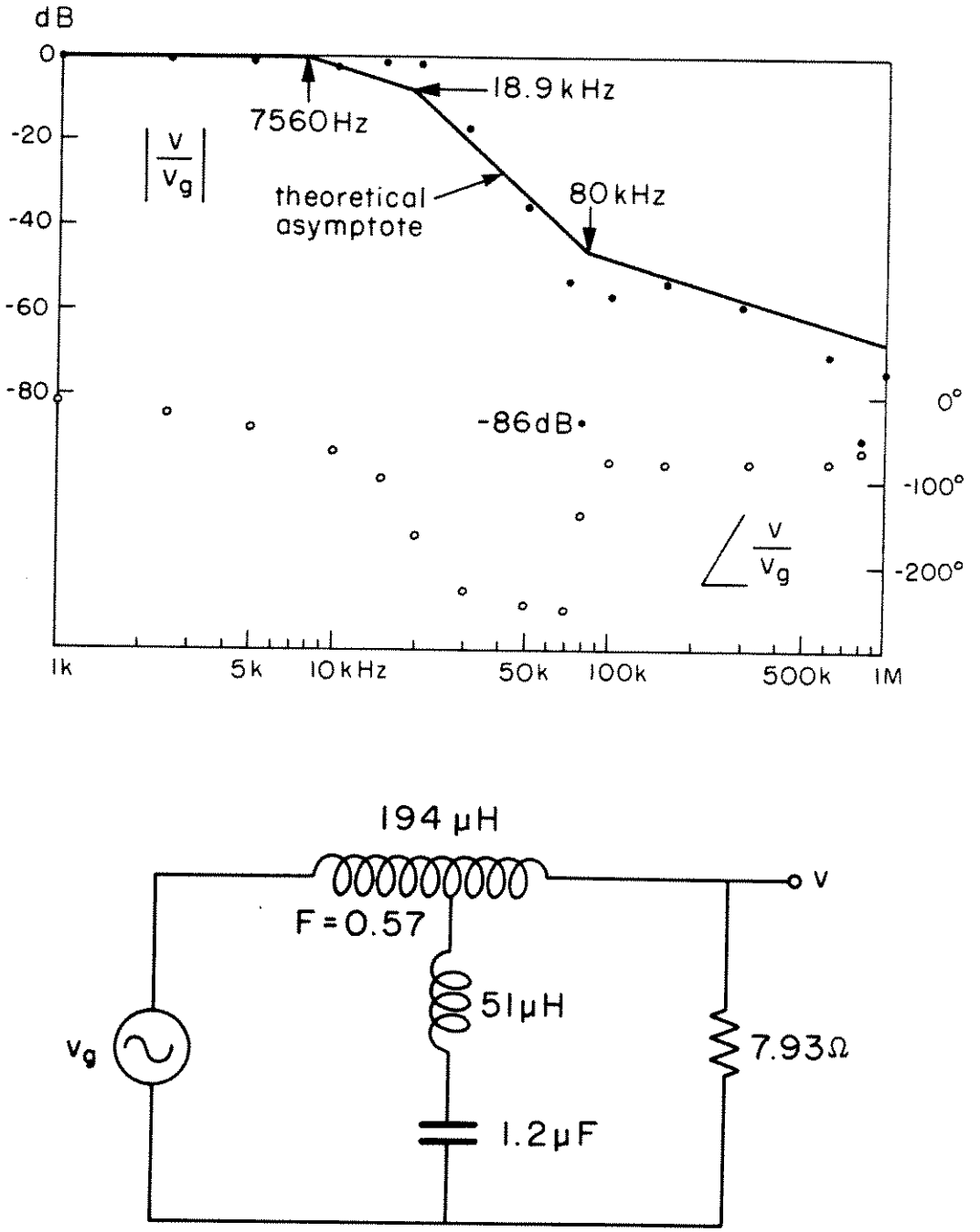

Fig. 5.8 Frequency response of the new filter in its elliptic function filter form showing an extreme attenuation of 86 dB at 80 kHz just two octaves above the 20 kHz passband corner.

the asymptote becomes negative owing to the complex zero pair at 80 kHz. In this manner the passband characteristic is acceptably flat, while a sharp cutoff is provided. At 80 kHz the deviation from the asymptote is -40 dB ensuring extreme attenuation of any signal at that frequency. Even though the filter has a 20 kHz bandwidth the attenuation at 80 kHz is 86 dB, transmission of about one part in 20,000. If the filter were subjected to an 80 kHz pulse train, such as a switching waveform, the dominant fundamental sinusoidal component in the pulse train Fourier expansion will be removed almost entirely. The next harmonic present lies at 240 kHz, three times the fundamental frequency, and is present in much reduced magnitude. By 240 kHz the asymptote is again a good approximation indicating 56 dB of attenuation. Note that this final asymptote would be lower if more passband deviation were allowed or if the zeroes were placed at a higher frequency. Even though the zeroes are only two octaves above the edge of the passband the attenuation for an 80 kHz pulse train and its harmonics is very respectable. At 810 kHz another complex zero pair is experimentally found. The previous analysis with the simplifying assumptions made does not predict this behavior.

Note that in going to the elliptic filter configuration the impedance matching condition was violated and as a result the final declining asymptote predicted by (5.5) rolls off at 20 dB/decade and not 60. This is not of any great consequence in a practical filter since second-order effects always limit ultimate attenuation. In the balance one obtains almost total attenuation at the fundamental frequency, rapid transition between pass and stop band, and acceptable stop band attenuation.

The load and passband specifications on the filter under discussion were chosen so that it could serve as a switching audio amplifier filter for the buck type configuration shown in Fig. 5.7. This particular application emphasizes the merits of the elliptic filter because it requires extreme attenuation of switching ripple without low-frequency attenuation of audio signals. Figure 5.9 shows the hardware chosen to implement the amplifier. The transistors Q1 and Q2 with the commutating diodes D1 act in a push-pull arrangement to apply a square-wave excitation to the filter. The IN914's and the associated R // 1/sC are present to ensure that transient voltage overshoots on the square wave are suppressed.

Figure 5.10 is a photograph of the oscilloscope traces of the square-wave input to the filter and the resulting output voltage. The square-wave input is 80 V peak-to-peak. Since the transistors stand off the peak-to-peak voltage they are being stressed at their full rated voltage and no overshoot can be tolerated. Note that the switching action is fast but virtually no transient overshoot is present.

The output voltage is about 300 mV p-p, but for a considerable portion of the period the waveform has essentially no ac component. Approximating the trace as being either zero or roughly triangular allows one to estimate the rms output voltage to be about 40 mV. Attenuation of the "heartbeat" of this switcher is therefore about 60 dB, rather remarkable since the switching frequency is only 2 octaves above the filter passband corner.

Modulation of the square-wave input about its nominal symmetric operating condition applies excitation to the filter at the modulation

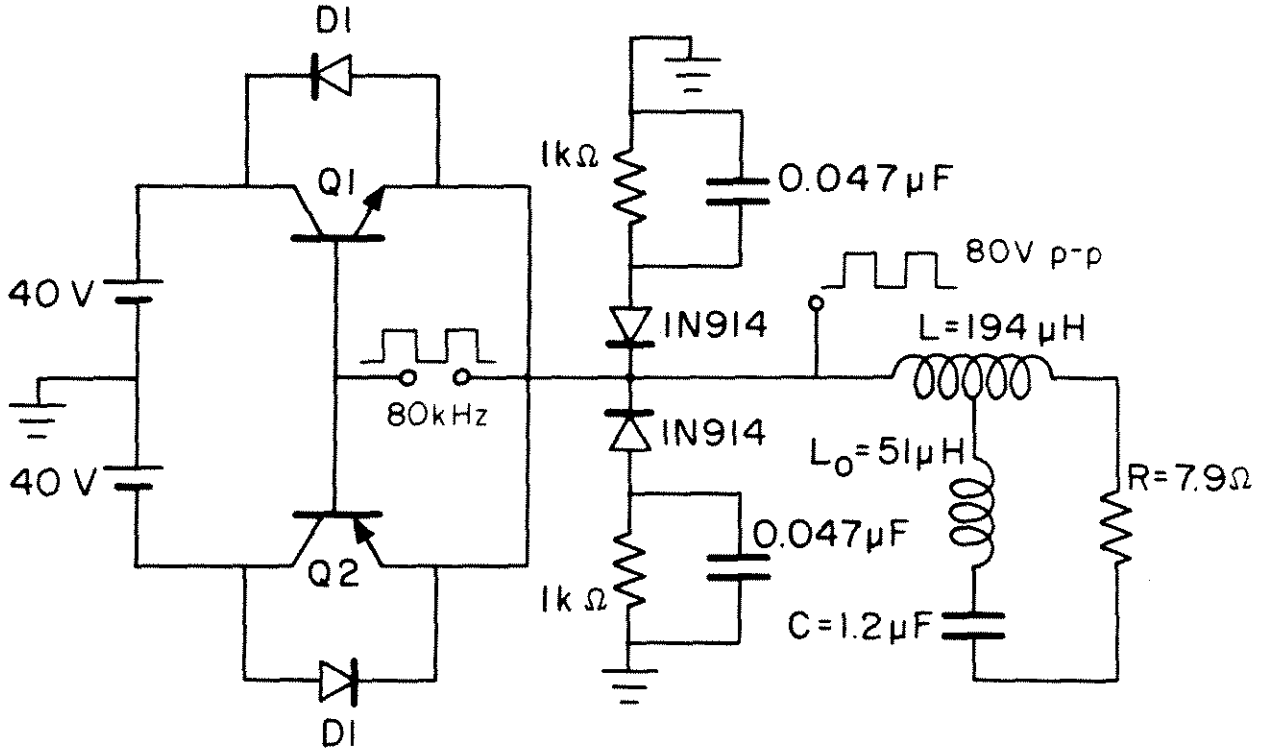

Fig. 5.9 Switching audio amplifier construction utilizes Q1, Q2, and D1, to implement a switch with bidirectional current capability.

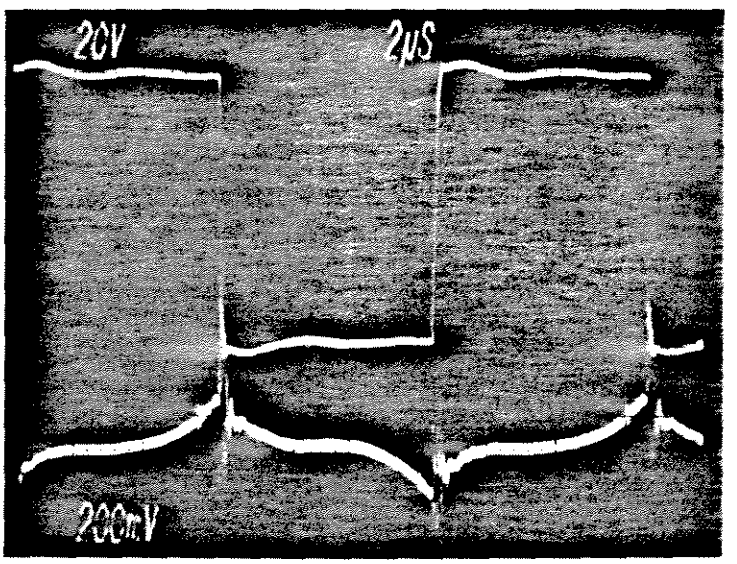

Fig. 5.10 Photographed oscilloscope traces show the 80 V square wave filter input voltage and the resultant 300 mV peak-to-peak output voltage ripple.

frequency as well as at the switching frequency. If the modulation is in the audio range the filter will pass the signal with no more than 2.5 dB attenuation while still suppressing the switching action by 60 dB.

Figure 5.11 shows pictures of the output of the amplifier to 1, 10, 15, and 20 kHz modulation. For the 1, 10, and 15 kHz signals a clean waveform is produced with the output power limited by the current ratings on the power supplies. The 12-18 watt outputs produced virtually no thermal stress on any of the circuit elements save for the 8 Ω resistance. At 20 kHz some difficulties interfered with the production of a clean waveform of appreciable amplitude. It is believed that careful attention to the modulation scheme and to the source impedance would allow the amplifier to realize the full bandwidth potential for unadulterated open-loop waveform reproduction at substantial output power.

It may seem that the new filter in its elliptic function configuration is very different from the configuration with the zeroes at infinity in that the possibility of the negative inductance effect is lost. This is not entirely true. The elliptic configuration shows a <u>frequency dependent negative-inductance effect</u>. If the switching frequency is just below the complex zero pair there is 180° less phase lead on the response than if the switching frequency is just above the zero location. The elliptic configuration shows ripple inversion by perturbing either the circuit element values (as before), or by varying the switching frequency, an effect not previously present when the zeroes were placed at infinity.

It is felt that the elliptic configuration deserves to be called truly a <u>zero</u> ripple configuration in that to an <u>excellent</u> approximation

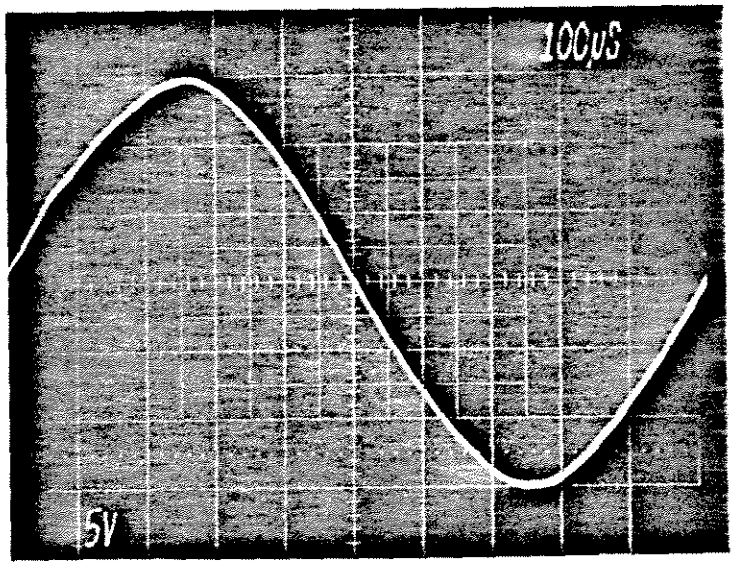

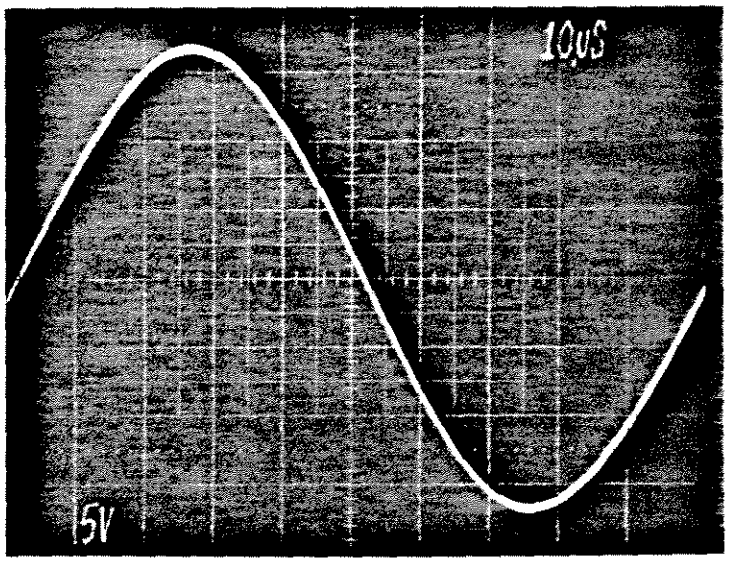

Fig. 5.11a 1 and 10 kHz sinusoids generated by the elliptic filter audio amplifier.

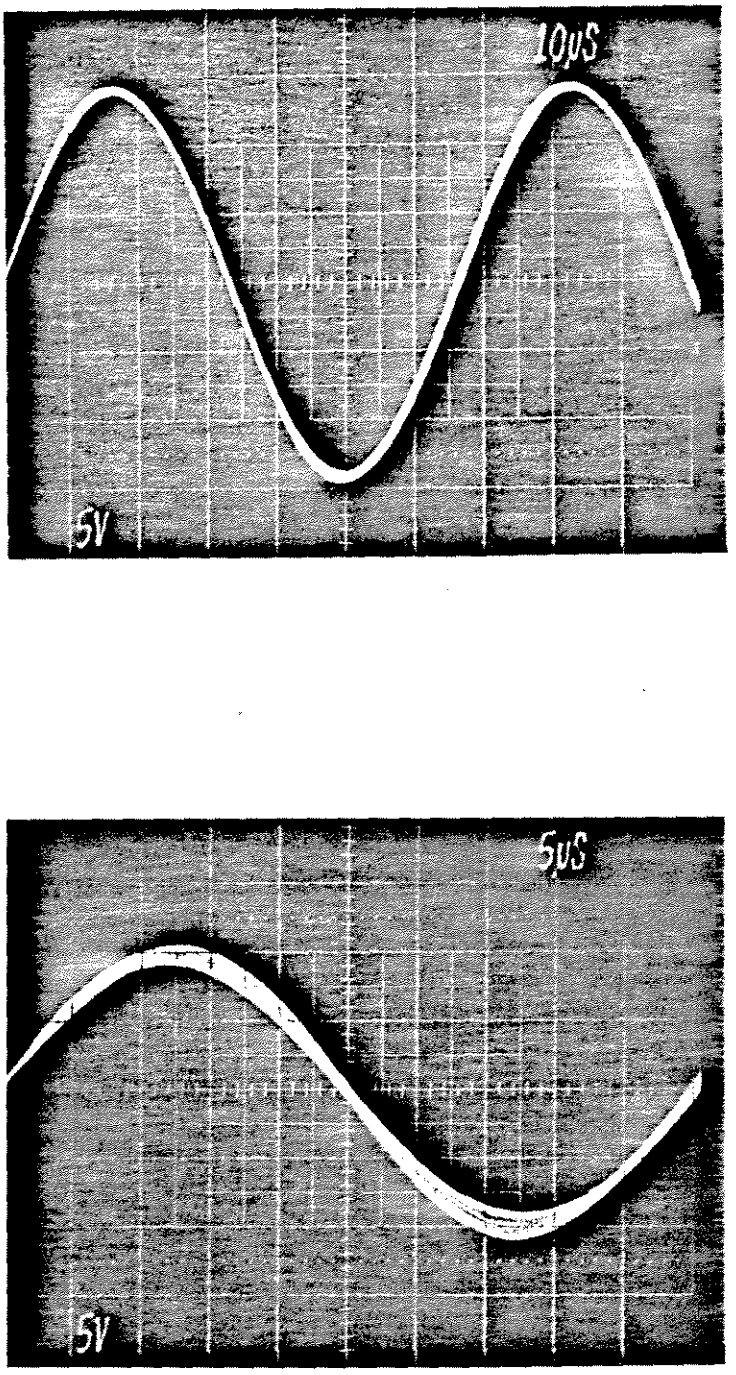

Fig. 5.11b 15 and 20 kHz sinusoids generated by the elliptic filter audio amplifier.

the fundamental component of the switching excitation is entirely rejected. Equation 5.5 shows that the position of the zeroes is not dependent on the load so that, even though the passband properties of the filter will be disturbed with changing load resistance, the location of the zeroes is unaffected and the filter remains zero ripple.

A zero output ripple buck type converter was used as an experimental example herein. It should be obvious, however, that a zero input ripple boost is also possible. Naturally this leads to the feasibility of zero input, zero output current ripple in boost-buck configurations. Previously discussed low-ripple modified Ćuk configurations could acquire extended bandwidth without sacrifice of ripple performance, or improved ripple attenuation for the same bandwidth, by adjustment of the components such that transmission zeroes exist at the switching frequency rather than at infinity.

The input filter section on the basic Ćuk converter, or that on a zero input ripple boost configuration, are examples of situations where the filter resistance R is comprised of parasitic resistances and as such it is not possible to obtain the desired passband properties of the elliptic filter. The model of Fig. 5.2 may be used to solve for the input current response to a switching waveform by taking R = 0 and solving for the current in the shorted path as a function of the source excitation. The method of the state-space solution is similar to that previously described and yields

$$\frac{i_{in}}{v_g}(s) = \frac{\left[L_0 - F(1-F)L\right]Cs^2 + 1}{s\,L(L_0Cs^2 + 1)} \qquad (5.14)$$

Equation (5.14) shows the typical sL impedance of the inductor as may be expected. The zero pair is still determined by the same circuit parameters as before and may be placed at the switching frequency. The glaring drawback to this transfer function is that it possesses a complex pole pair that is damped only by circuit parasitics and may have a very high resonant peak. Such behavior will complicate tailoring loop gain magnitude and phase for feedback regulation, as well as making the system susceptible to resonant response at $\omega = 1/\sqrt{L_0 C}$. These problems exist irrespective of the location of the zeroes, and are possibly the most severe shortcomings of the zero input ripple topologies. In practice however the limitation may not be as inhibiting as indicated by the idealized analysis. The sL impedance may be large enough at the filter resonant frequency so that the resonance limited by parasitics does not exceed 0 dB and the severity of the problem in somewhat lessened. The point of this discussion is that care should be exercised when applying high Q filters to switching converters, or else other performance aspects may suffer for the sake of improved switching ripple performance.

5.4 Review

In this chapter a particular filter configuration exhibiting the negative inductance effect was subjected to close scrutiny by means of state-variable analysis. Solution of the state equations with the Laplace transform produced a frequency domain explanation for the negative inductance effect which was shown to be related to the position of a zero pair in the s-plane. The filter transition from a positive ripple

current sense to a negative one was shown to correspond with the change from a minimum phase to a nonminimum phase system. Filter transmission zeroes move from the imaginary axis through the point at infinity to the real axis as the filter values are varied about the impedance matching condition of Chapter 3. With placement of the zeroes at infinity, the matching condition produces a third-order attenuation characteristic which rejects all high frequencies indiscriminately. Realization that the switching disturbance has a known discrete frequency spectrum prompted the idea of placement of the transmission zeroes in a manner that fully rejects the fundamental frequency component of the switching action. Application of some concepts of classical filter theory refined this idea, and a third-order elliptic-function power-processing filter developed. A prototype filter was built and found to perform very well in accordance with the analysis.

This chapter's extensions to the zero-ripple configurations deserve to be called zero ripple not only because positive or negative sense can be observed on the ripple waveforms, but also because the ripple attenuation is extreme. Excellent performance is obtained with minimal penalty in terms of component size and weight.

Development of the new filter concludes Part 1 of this work. The attained objective of this first part is the analysis of the ripple properties of the new converter and development of converter configurations with improved external current characteristics. Three general techniques for ripple attenuation were exposed, each gaining sophistication over the previous one. However, the price of the improved performance demonstrated

by the later developments is increased sensitivity to parameter variations. The impedance division technique for the coupled-inductor converter requires only that gross magnitude inequalities be satisfied for effective functioning. If one wishes to gain the component size advantages boasted by the impedance matching technique, the penalty is that the matching condition equality must be satisfied, or at least nearly so, which imposes tighter design tolerances on inductive components. The most sophisticated development, the elliptic filter, is also the most susceptible to variations in component values. For the classical filter frequency response to be obtained, each circuit parameter is uniquely determined. The technique chosen for a particular application will depend on the performance requirements and the amount of control the designer can exercise over the system component tolerances. In addition to the development of analysis technique, the principles realized were applied to generate a number of new or revised topologies each with its own merits with respect to ripple performance. Sufficient laboratory verification is included to illustrate the attributes of the new configurations and show the practical applicability of the techniques. Thus the analysis produced and the extensions envisioned fulfill the objectives of Part 1 with experimental substantiation.

PART II

MODERN CONTROL TECHNIQUES

for

SWITCHING REGULATORS

CHAPTER 6

OPTIMAL REGULATION FOR SWITCHING CONVERTERS

There are two well-established schools of thought on the subject of formulating feedback controllers. For want of more descriptive terms the two may be referred to as classical, and modern or optimal. Choosing such terminology does not imply any disdain for the classical control theory by hinting that it is conventional, archaic, or apriori a suboptimal or inferior approach. Indeed, the criteria of the classical techniques are used to judge the effectiveness of the modern in generating acceptable controllers, and hence there can be no legitimate condescension toward the older more established approach. Each method has its own particular strengths and weaknesses and so the designer who understands both is better equipped than one restricted to either. There are several typifying traits that serve to sharpen the distinction between classical and modern technique. Perhaps the most fundamental difference between the two is that the classical technique relies heavily on the steady-state system response to sinusoidal excitation, while the modern approach is primarily concerned with response to initial conditions.

Classical analysis and design generally begins by determining the system open-loop differential equations which are cast as algebraic polynomials in the frequency domain by means of the Laplace transform. The system transfer functions are factored to obtain the pole and zero locations, and the Bode diagram, root locus plot, and/or Nyquist diagram are used to interpret the system frequency response characteristics. Usually

the response is shaped by addition of series compensating elements obtaining an error signal proportional to the controlled variable with desirable phase properties that allow this single return path to close the feedback loop in a stable manner. Classical control formulation is guided by abundant established techniques in the frequency domain that use criteria such as gain and phase margin to generate a control scheme that will provide acceptable performance. Graphical techniques or equivalent circuit models with important quantities identified and related to circuit parameters are often used, allowing the designer to reformulate the open-loop plant, if necessary, to obtain more desirable characteristics. The analyst may relate to the classical approach in physically understandable terms such as loop gain, corner frequencies and phase response. The facilities provided by the graphical methods give the well-versed engineer a "feel" for the important properties of the plant to be controlled, and an understanding of the obstacles to be overcome in arriving at an effective control formula.

Modern analysis and design generally begins by determining the system open-loop differential equations expressed in the time domain by means of the matrix first-order differential equation provided by state-variable expansion. The matrix expressions describing system dynamics are used directly to constrain the minimization of a time domain penalty function on output error and control effort. In the cases of interest here, the minimization of the performance error penalty results in a control law that returns a linear combination of all the states and renders the closed loop response optimal by performance definition.

The modern approach tacitly assumes that the feedback signal will be derived from all of the system states, while the classical method usually returns an error signal derived only from the controlled variable. The ability to design multi-state feedback loops (and to use multiple controllers) is not gained without an attendant penalty. In all but the most simple cases the modern approach relies heavily on numerical methods and as such fails to provide the insight of a closed-form answer. An ill-conditioned plant may make the feedback gains very critical and the optimal solution worthless for practical application. In spite of its shortcomings the optimal control theory provides a powerful and quite general approach to regulation loop design. Even for complicated situations involving several states and controlled quantities the engineer's design task is reduced to defining a performance criterion and identifying the system's state-variable description. The rest of the solution may be handled by digital computer.

In this chapter the methods of optimal control are established for and applied to switching converters. The classical approach in this vein is already in wide use and well documented [1]. The material presented here is intended to provide an alternative point of view that complements and may be used in conjunction with frequency domain analysis. Only one of the many facets of modern control theory, the linear regulator problem, is treated. Under certain circumstances the solution for the modern controller becomes linear and time invariant, and thus useful from a practical standpoint. The major contribution of this chapter is the formulation of the regulator problem for switching

converters. Solution techniques are extensively documented elsewhere and references for these are provided. For illustrative purposes two solutions are obtained by separate methods for simple converter topologies. The examples not only show the utility of the method but also produce interesting and useful closed-form results for optimally controlling the widely-used buck converter.

The remaining two chapters of Part 2 deviate somewhat from the theme of optimal control in that the penalty function approach is abandoned in favor of directly prescribing the time response to initial conditions. In order to make this task meaningful and manageable a discrete time-domain system description of general applicability is developed. The accuracy of this model is substantiated by laboratory demonstration of a predicted time-domain sequence termed a finite settling time response. In keeping with the intent of this control analysis, relationships between the discrete and classical techniques are derived so that the designer may use either or both as need dictates.

6.1 System linearization

In order to apply the results of the linear regulator problem of optimal control theory, one must first arrive at a linear state-space description for the inherently nonlinear switcher that exposes the effect of duty-ratio modulation control. With this goal in mind, consider a switching converter operating with two switched topologies in like manner to the several converters mentioned in Chapter 1. The number of switched topologies each cyclic period is not a limitation on the linearization process, but since two switched intervals per period is very common it

will be used for concreteness in the development. The state equations during interval DT_s may be written as

$$\dot{x} = A_1 x + b_1 V_g \tag{6.1}$$

where the dot indicates the derivative with respect to time. The output of the converter, y, usually may be expressed as a linear combination of the states, compactly written as

$$y_1 = C_1^T x \tag{6.2}$$

In general x, V_g and y are vectors and A, b, and C are matrices. Typically, however, V_g is a scalar equal to the source voltage and y is a scalar output voltage or current. When this is the case b and C degenerate to vectors. The scalar input, scalar output case will be assumed in the following even though the derivations can be generalized to multi-input, multi-output configurations. During the second switched interval the equations of state and output can be expressed similarly with a suitable change of subscript.

$$\dot{x} = A_2 x + b_2 V_g \tag{6.3}$$

$$y_2 = C_2^T x \tag{6.4}$$

The state-space averaging method [1] met with considerable success and acceptance in generation of cannonical linear circuit models for switching converters. This same technique will be used here to coalesce (6.1) through (6.4) into a set of average equations that describe the low-frequency system dynamics. The result is

$$\dot{x} = Ax + bV_g \tag{6.5}$$

and

$$y = C^T x \tag{6.6}$$

where $A = DA_1 + D'A_2$, $b = Db_1 + D'b_2$ and $C^T = DC_1{}^T + D'C_2{}^T$. The averaged equations (6.5) and (6.6) can yield solutions for the steady-state conditions and the source voltage to state or output transfer functions. However, it is desired to obtain a set of equations that describe the effects of duty ratio modulation since feedback control is exercised by varying the duty ratio in response to some error on the controlled variable.

To determine the duty ratio modulation to state transfer functions, assume in (6.5) that the state vector x has some perturbation $\hat{x}$ superimposed, and likewise the duty ratio D some perturbation $\hat{d}$, where the modulation terms are small compared with the steady-state quantities. Then (6.5) is expanded to

$$[\dot{x} + \dot{\hat{x}}] = [A + \hat{A}] [x + \hat{x}] + [b + \hat{b}] V_g \tag{6.7}$$

where $\hat{A} = \hat{d} [A_1 - A_2]$ and $\hat{b} = \hat{d} [b_1 - b_2]$. Expansion of (6.7) yields

$$[\dot{x} + \dot{\hat{x}}] = Ax + A\hat{x} + \hat{A}x + \hat{A}\hat{x} + bV_g + \hat{b}V_g \tag{6.8}$$

Subtraction of equation (6.5) from (6.8) reveals the relationship between the duty ratio control induced $\hat{A}$ and $\hat{b}$ and state perturbation $\hat{x}$ as

$$\dot{\hat{x}} = A\hat{x} + \hat{A}x + \hat{A}\hat{x} + \hat{b}V_g \tag{6.9}$$

The term $\hat{A}\hat{x}$ may be expanded to $[A_1 - A_2]\hat{d}\hat{x}$. The factor $\hat{d}\hat{x}$ is the product of two quantities assumed small, and is hence very small compared to first order perturbation and control terms. Standard linearization practice

dictates neglect of such second order terms. The motivation for doing so is that the system small-signal model returns to the manageable linear time invariant form. With neglect of $\hat{A}\hat{x}$, (6.9) may be rewritten as

$$\dot{\hat{x}} = A\hat{x} + g\hat{d} \tag{6.10}$$

where g is the vector formed by the sum $[A_1-A_2]x_0 + [b_1-b_2]V_g$. The factor x_0 used in the calculation of g is the steady state solution to (6.5) obtained by setting $\dot{x} = 0$. Equation (6.10) is the desired linearized small-signal dynamic equation expressing the transient and duty ratio control induced behavior of $\hat{x}$.

6.2 Optimal feedback gains

If feedback control is utilized then $\hat{d}$ becomes a function of $\hat{x}$. The desire is to obtain an optimal functional relationship between $\hat{d}$ and $\hat{x}$. To any disturbance $\hat{x}$ there may be a corresponding undesired change in the controlled quantity y. To first order we have

$$\hat{y} = C^T\hat{x} + \hat{C}^T x_0 \tag{6.11}$$

where $\hat{C}^T = \hat{d}[C_1{}^T - C_2{}^T]$. Terms of order $\hat{C}^T\hat{x}$ are neglected with argument as before. A criterion for control optimality would be one that minimizes the magnitude of $\hat{y}$ stemming from $\hat{x}$ while still exercising acceptable levels of control effort. The output disturbance should be kept as small as possible for all time so a useful criterion is to minimize

$$J = \frac{1}{2}\int_0^\infty \left(r_0\hat{y}^2 + r_1\hat{d}^2\right)\, dt \tag{6.12}$$

where r_0 and r_1 are greater than zero to make the integrand positive definite. Thus $\hat{y}$ and $\hat{d}$ excursions of either sign will receive an appropriately weighted penalty. The values chosen for r_0 and r_1 determine the relative penalties for output deviation and for exercise of control. Substitution of (6.11) into (6.12) and expansion of the quadratic form yields

$$J = \frac{1}{2}\int_0^\infty \left(\hat{x}^T C r_0 C^T \hat{x} + 2x_0^T \hat{C} r_0 C^T \hat{x} + x_0^T \hat{C} r_0 \hat{C}^T x_0 + r_1 \hat{d}^2\right) dt \qquad (6.13)$$

To simplify notation and reveal the presence of $\hat{d}$ in the terms of the performance index J, define $R_1 = Cr_0C^T$, $R_2 = [C_1-C_2]r_0C^T$ and $R_3 = [C_1-C_2]r_0[C_1-C_2]^T$.

Now rewrite (6.13) as

$$J = \frac{1}{2}\int_0^\infty \left[\hat{x}^T R_1 \hat{x} + 2x_0^T R_2 \hat{x}\hat{d} + \left(x_0^T R_3 x_0 + r_1\right)\hat{d}^2\right] dt \qquad (6.14)$$

Equation (6.14) is of the form $J = \int_0^\infty L dt$.

In order to find a stationary point of J we may use results of the calculus of variations. We define

$$H = L + \lambda^T f = \frac{1}{2}\left[\hat{x}^T R_1 \hat{x} + 2x_0^T R_2 \hat{x}\hat{d} + (x_0^T R_3 x_0 + r_1)\hat{d}^2\right] + \lambda^T(A\hat{x} + g\hat{d}) \qquad (6.15)$$

where f is the right-hand side of (6.10), the linearized state perturbation equation. The vector of undetermined coefficients, λ, is the Lagrange multiplier vector and H is referred to as the Hamiltonian. For an extremum on J the Euler-Lagrange equations (6.16) and (6.17) must be satisfied [12]:

$$\dot{\lambda}^T = -\frac{\partial H}{\partial \hat{x}} \tag{6.16}$$

$$\frac{\partial H}{\partial \hat{d}} = 0 \tag{6.17}$$

The symbol ∂ indicates the partial derivative. Expanding these equations in terms of the particular problem at hand produces

$$\dot{\lambda}^T = -\left(\hat{x}^T R_1 + x_0{}^T R_2 \hat{d} + \lambda^T A\right) \tag{6.18}$$

and

$$\frac{\partial H}{\partial \hat{d}} = x_0{}^T R_2 \hat{x} + \left(x_0{}^T R_3 x_0 + r_1\right)\hat{d} + g^T\lambda = 0. \tag{6.19}$$

From (6.19) the optimal control law may be written as

$$\hat{d}^o = -\frac{g^T\lambda + x_0{}^T R_2 \hat{x}}{x_0{}^T R_3 x_0 + r_1} \tag{6.20}$$

Equation (6.20) would give the answer for $\hat{d}^o$ in the terms of $\hat{x}$ if λ were known. Since an optimal feedback law is sought we may suspect that λ depends on $\hat{x}$. Assign $\lambda = S\hat{x}$ assuming linear feedback and see if a matrix S can be determined without contradiction of optimality conditions. Transposing (6.18) and substituting $S\hat{x}$ for λ yields

$$\dot{S}\hat{x} + S\dot{\hat{x}} = -R_1\hat{x} - R_2^T x_0 \hat{d} - A^T S\hat{x} \tag{6.21}$$

Substitution from (6.10) for $\dot{\hat{x}}$ and (6.20) for $\hat{d}$ yields, after a little manipulation,

$$\dot{S} = \frac{Sgg^TS}{x_0{}^T R_3 x_0 + r_1} + \frac{Sgx_0{}^T R_2 + R_2{}^T x_0 g^T S}{x_0{}^T R_3 x_0 + r_1} - \left(SA + A^T S\right) + \frac{R_2{}^T x_0 x_0{}^T R_2}{x_0{}^T R_3 x_0 + r_1} - R_1 \tag{6.22}$$

Note that $\hat{x}$, assumed nonzero, has been divided out of both sides of (6.22). Equation (6.22) is a matrix differential equation in S referred to as the matrix Riccati equation characterized by the S^2 dependence of the derivative. Note that the terms of (6.22) are all symmetric. For steady-state regulator gains, $\dot{S}$ is set equal to zero and a solution for S determined. Equation (6.20) with $\lambda = S\hat{x}$ is then the optimal feedback law. Since $S(\infty)$ may be chosen to be symmetric, S also can be symmetric and (6.22) contains $n(n + 1)/2$ nonlinear equations for as many unique elements of S. This fact is exploited in the literature to obtain solutions for S and hence $\hat{d}^0$.

There are many numerical techniques in optimal control literature for the solution of (6.22), varying in sophistication from direct numerical integration until $\dot{S} \simeq 0$ to eigenanalysis based solutions [12-15]. Suffice it to point out that the solution for optimal regulator feedback gains can be implemented numerically on a digital computer from the starting point of the switched state descriptions, the penalty coefficients r_0 and r_1, and the nominal operating duty ratio, needed to determine the steady-state state vector.

An important and common special case of (6.22) occurs when the controlled variable y has a constant relationship to the state vector x during both switched subintervals. Then $R_2=R_3=0$ and (6.22) reduces to

$$\dot{S} = \frac{Sgg^TS}{r_1} - \left(SA + A^TS\right) - R_1 \qquad (6.23)$$

The optimal control law is given by

$$\hat{d}^o = - \frac{g^T S \hat{x}}{r_1} = - K^T \hat{x} \tag{6.24}$$

where K is the feedback gain vector. Equations (6.23) and (6.24) will be used for illustration of the modern control approach to converter feedback regulation in the following sections.

6.3 Riccati equation approach example

At this point a simple illustrative example is in order. To avoid involvement in numerical techniques, a first-order system will be examined. Consider a buck converter with no output capacitance as shown in Fig. 6.1. The state equations for the two switch positions may be written as

$$\begin{aligned} \frac{di}{dt} &= - \frac{R}{L} i + \frac{1}{L} V_g \; ; \; DT_s \\ \frac{di}{dt} &= - \frac{R}{L} i + 0 \; V_g \; ; \; D'T_s \end{aligned} \tag{6.25}$$

Equation (6.10) then takes the form of (6.26)

$$\frac{di}{dt} = \underbrace{- \frac{R}{L}}_{A} \hat{i} + \underbrace{\frac{V_g}{L}}_{g} \hat{d} \tag{6.26}$$

If we choose as the regulated quantity the output voltage, then $R_1 = r_0 R^2$ and with the terms identified in (6.26) we may write the Riccati equation (6.23) in the scalar form as

$$\dot{S} = \frac{S^2 V_g^{\,2}}{r_1 L^2} + \frac{2SR}{L} - r_0 R^2 \tag{6.27}$$

The solution to (6.27) with $\dot{S}$ set to zero may be evaluated by means

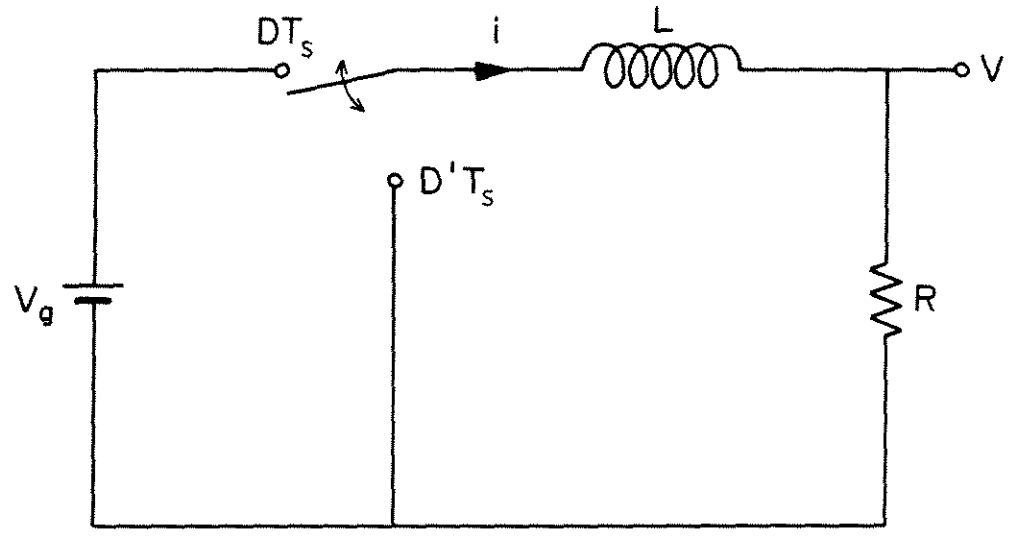

Fig. 6.1 Simple buck converter without output capacitor is a first-order system shown with inductor current identified as choice of state.

of the quadratic formula giving

$$S = - \frac{RLr_1}{V_g^2} \left[1 \pm \sqrt{1 + \frac{V_g^2 r_0}{r_1}} \right] \tag{6.28}$$

Note in (6.28) that there are two possible solutions for S since (6.27) is quadratic. The positive root is the desired answer since that root will result in negative feedback and a stable system. From (6.24) the optimal control law for this simple buck converter is

$$\hat{d}^o = \frac{R}{V_g} \left[1 - \sqrt{1 + \frac{V_g^2 r_0}{r_1}} \right] \hat{i} \tag{6.29}$$

Let's now write the equivalent of (6.26) with $\hat{d}$ prescribed by (6.29) to see how the optimal control places the system closed-loop pole.

$$\frac{d\hat{i}}{dt} = - \frac{R}{L} \hat{i} + \frac{R}{L} \left[1 - \sqrt{1 + \frac{V_g^2 r_0}{r_1}} \right] \hat{i} \tag{6.30}$$

Note that the optimal control has exactly removed the system open-loop pole at -R/L so (6.30) may be condensed as

$$\frac{d\hat{i}}{dt} = - \frac{R}{L} \sqrt{1 + \frac{V_g^2 r_0}{r_1}} \hat{i} \tag{6.31}$$

exposing the closed-loop dynamic equation. The closed-loop pole is seen to lie on the negative axis in the s-plane regardless of its original position and irrespective of choice of r_0 and r_1 as long as they are positive. The time response of the system to a disturbance is exponentially decaying with the decay time constant a function of the penalty parameters:

$$\hat{i}(t) = \hat{i}(0)\ e^{-R/L\sqrt{1 + V_g^2 r_0/r_1}\ t} \tag{6.32}$$

Equation (6.32) shows that the decay is increasingly more rapid as the relative penalty on output deviation, r_0/r_1, is increased. This result shows how any desired decay time constant may be generated by choice of r_0 and r_1 and points out a practical difficulty in the modern approach. How does one choose r_0 and r_1 in the performance criterion? Here this choice amounts to choosing a feedback gain, or decay time constant for the closed-loop system, and the latter two alternatives are much more easily understood physically. It appears that a poor trade-off in point of view has been made in order to support the claim that the control is optimal with respect to a chosen criterion. One could as easily choose a practically implementable feedback gain from circuit design considerations and then solve for the sense in which this control is optimal, i.e. the values of r_0 and r_1 in (6.12). These criticisms of the penalty function approach are valid and especially caustic when a first-order single-input single-output system is being examined. The method is illustrated by this simple example but the utility of the approach is not shown when a single gain constant needs to be determined. The next section will develop a second-order example which shows how the modern approach can be most useful when used in conjunction with practical design considerations.

6.4 The Kalman equation approach

Before considering an example of higher order it behooves us to develop an alternative solution to the optimal gain vector that does not involve solution for the Riccati matrix. The problem stated by the

Riccati equation in n(n + 1)/2 unknown elements can be reduced to a problem in n unknown feedback gains when a single control is used. The reformulation of the steady-state Riccati matrix problem in terms of the feedback gain vector K is attributed to R. E. Kalman [13, 16]. A similar exposition with appropriate modifications for our purposes is used here.

The solution for the optimal linear regulator gains is obtained when the coefficients of the S matrix are determined from

$$- SA - A^T S + \frac{Sgg^T S}{r_1} = R_1 \tag{6.33}$$

and the result used in (6.24) where the feedback gain vector K is defined by

$$K = \frac{Sg}{r_1} \tag{6.34}$$

The immediate goal is to reformulate (6.33) using the information of (6.34) resulting in a problem statement in terms of the feedback gain vector directly. This may be accomplished in three steps although the motivation for the manipulations at first may seem obscure. First, add and subtract pS from the left-hand side of (6.33) resulting in (6.35) where p is an arbitrary possibly complex variable.

$$S(pI-A) + (-pI-A^T)S + \frac{Sgg^T S}{r_1} = R_1 \tag{6.35}$$

For convenience let $E(p) = (pI-A)^{-1}g$; then $E^T(-p) = g^T(-pI-A^T)^{-1}$. Second, multiply (6.35) from the left by $E^T(-p)$ and from the right by E(p), reducing it to a scalar equation.

$$E^T(-p)Sg + g^T SE(p) + E^T(-p)\frac{Sgg^T S}{r_1}E(p) = E^T(-p)R_1 E(p) \tag{6.36}$$

Third, use (6.34) to eliminate S in (6.36) producing (6.37) in terms of the gain vector K.

$$E^T(-p)K + K^TE(p) + E^T(-p)KK^TE(p) = E^T(-p)\frac{R_1}{r_1}E(p) \qquad (6.37)$$

Addition of 1 to each side of (6.37) and factorization of the left-hand side simplifies the expression somewhat and yields the equivalent statement of (6.37) in (6.38)

$$[1 + E^T(-p)K][1 + K^TE(p)] = E^T(-p)\frac{R_1}{r_1}E(p) \qquad (6.38)$$

$$E(p) = (pI-A)^{-1}g \qquad (6.39)$$

which is referred to as the Kalman equation [13] when E(p) is given by (6.39). The use of (6.38) in solution for the optimal regulator gains relies on establishment of n equations in the unknown gains K_i by equating coefficients in like powers of p. Since p is arbitrary the coefficients must be identical. Perhaps the method is best explained by another example.

The circuit chosen to illustrate the Kalman equation approach is the common buck converter of Fig. 6.2. The buck converter with the output capacitance included is a second-order system and will serve not only to show the utility of (6.38) but also will be instrumental in pointing out the advantages one may gain by viewing the control problem with modern analysis as well as with the usual techniques.

The state equations for the two switch positions are easily written if one chooses the inductor current and the capacitor voltage as components of the state vector.

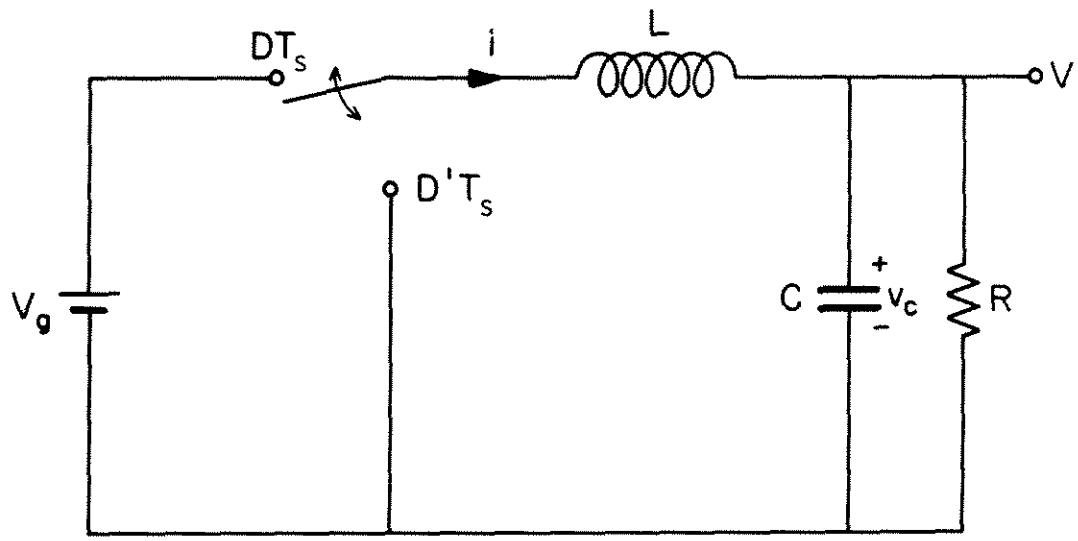

Fig. 6.2 The common buck converter shown with inductor current and capacitor voltage identified as state variables.

$$\begin{bmatrix} \dot{i} \\ \dot{v}_c \end{bmatrix} = \underbrace{\begin{bmatrix} 0 & -\frac{1}{L} \\ \frac{1}{C} & -\frac{1}{RC} \end{bmatrix}}_{A_1} \begin{bmatrix} i \\ v_c \end{bmatrix} + \underbrace{\begin{bmatrix} \frac{1}{L} \\ 0 \end{bmatrix}}_{b_1} V_g \quad ; \quad \underline{DT_s} \qquad (6.40)$$

$$\begin{bmatrix} \dot{i} \\ \dot{v}_c \end{bmatrix} = \underbrace{\begin{bmatrix} 0 & -\frac{1}{L} \\ \frac{1}{C} & -\frac{1}{RC} \end{bmatrix}}_{A_2} \begin{bmatrix} i \\ v_c \end{bmatrix} + \underbrace{\begin{bmatrix} 0 \\ 0 \end{bmatrix}}_{b_2} V_g \quad ; \quad \underline{D'T_s} \qquad (6.41)$$

For the buck converter A_1 equals A_2 since the switch does not rearrange the relationship of any of the energy storage elements. This simplifies calculation of the perturbation equation (6.10) since g will not depend on the operating point as it does for the general case. With use of (6.40) and (6.41), the equivalent of (6.10) is written for this problem as

$$\begin{bmatrix} \dot{\hat{i}} \\ \dot{\hat{v}}_c \end{bmatrix} = \underbrace{\begin{bmatrix} 0 & -\frac{1}{L} \\ \frac{1}{C} & -\frac{1}{RC} \end{bmatrix}}_{A} \begin{bmatrix} \hat{i} \\ \hat{v}_c \end{bmatrix} + \underbrace{\begin{bmatrix} \frac{V_g}{L} \\ 0 \end{bmatrix}}_{g} \hat{d} \qquad (6.42)$$

If this buck converter is to be used as a voltage source then it seems reasonable that the deviations in the output voltage should be penalized in the performance criterion. Since the output voltage equals the

capacitor voltage state a suitable criterion may be generated by choosing R_1 and r_1 as shown in (6.43) where r_0 and r_1 are chosen to determine

$$J = \frac{1}{2}\int_0^\infty \left(\hat{x}^T \underbrace{\begin{bmatrix} 0 & 0 \\ 0 & r_0 \end{bmatrix}}_{R_1} \hat{x} + r_1 \hat{d}^2\right) dt \tag{6.43}$$

the relative penalties for voltage error and control exercise. To use (6.38) one must first evaluate E(p) by (6.39).

$$E(p) = (pI-A)^{-1}g = \frac{\begin{bmatrix} \frac{V_g}{L}\left(p + \frac{1}{RC}\right) \\ \frac{V_g}{LC} \end{bmatrix}}{p^2 + \frac{p}{RC} + \frac{1}{LC}} \tag{6.44}$$

When (6.44) is used in (6.38) a fourth order expression in p results:

$$p^4 + \left[2\left(\frac{K_2V_g + 1}{LC} + \frac{K_1V_g}{LRC}\right) - \left(\frac{1}{RC} + \frac{K_1V_g}{L}\right)^2\right]p^2 + \left(\frac{K_2V_g + 1}{LC} + \frac{K_1V_g}{LRC}\right)^2$$

$$= p^4 + \left[\frac{2}{LC} - \left(\frac{1}{RC}\right)^2\right] p^2 + \frac{r_0}{r_1}\left(\frac{V_g}{LC}\right)^2 + \left(\frac{1}{LC}\right)^2 \tag{6.45}$$

From (6.45) two equations for the components of the gain vector may be obtained by equating the coefficients of like powers of p. From the constant term

$$\frac{r_o}{r_1} V_g^2 + 1 = (K_2V_g + K_1V_g/R + 1)^2 \tag{6.46}$$

and from the p^2 coefficients

$$K_1 = \sqrt{2K_2L/(V_gC)} \tag{6.47}$$

One may immediately see a difficulty in this approach since the simultaneous equations (6.46) and (6.47) are nonlinear and do not possess a unique solution. The appropriate solution is the positive definite one resulting in negative feedback as in the previous example. Choosing r_0/r_1, the relative weight on voltage error, determines a unique solution for K_1 and K_2. Notice that again the engineering tradeoffs are involved in choosing some abstract weighting coefficients rather than something physically meaningful like a feedback gain or the closed-loop system bandwidth. However, one may see in (6.46) that since K_1 and K_2 are positive and have a relationship fixed by (6.47) both feedback gains will monotonically increase with r_0/r_1. So, instead of choosing the penalty parameters, either K_1 or K_2 may be selected with larger values reflecting less constraint on control and more concern for voltage error. A good selection might be to choose the voltage return gain K_2 guided by performance specifications and practical design considerations just as the feedback gain may have been chosen in the previous first-order example. Then (6.47) prescribes the corresponding current feedback gain that will result in the best transient response possible in the integral square sense. If one were interested one could then calculate r_0 and r_1 from (6.46) to see what specific performance index is minimized by one's selection of K_1 and K_2, but the exercise is purely academic. The important result is that the relative amounts of voltage and current feedback prescribed by (6.47) will give the best output voltage transient

response for a given level of control exercise determined by selection of a physically meaningful feedback gain. The same situation will arise with higher-order single-input single-output systems. If the designer wishes to employ multiple-state feedback he may select a single gain from practical design considerations, and the remainder of the gain constants are uniquely determined from the Kalman equation (6.38) and the requirement for negative feedback.

The example of this section has produced an important result for the common buck converter regulated by state-vector feedback that would in itself justify the development in this chapter. If such a buck converter is used as a voltage source and it is desired that the output voltage recover from a disturbance with minimal squared error, then the ratio of feedback gains is fixed by (6.47). One may observe that the relationship between the gains given by (6.47) does not depend on the load or operating condition making the result particularly useful.

It should be noted at this point that the Kalman equation approach is useful for hand calculations and can yield closed form results for simple situations. However, the analysis effort grows rapidly with increasing system order and numerical solutions gain favor. This method results in the nonlinear equations (6.38) which may have several solutions, only one of which is correct. As a result the implementation of the solution on digital computer is unduly complicated, as is the direct solution to the algebraic Riccati equation (6.33). For this reason the numerical solutions typically rely on alternative methods

that do not involve solving simultaneous nonlinear algebraic equations, such as direct numerical integration of (6.23) until $\dot{S} = 0$ to solve for K.

6.5 Optimal s-plane pole location

To aid in relating the method of this chapter to the classical approach some results from [15] and [16] concerning the closed-loop pole locations will be stated here without proof. It is possible to determine the asymptotic properties of the closed-loop pole locus as r_0/r_1 becomes very large or very small. As r_0/r_1 approaches zero the relative penalty on control exercise dominates the performance criterion and the system closed-loop poles approach the open-loop locations, unless open-loop poles are located in the right-half plane. In that circumstance the closed-loop poles tend toward the open-loop locations or their mirror-image positions in the left-half plane. State vector feedback stabilization of an unstable plant with minimal control effort is achieved by effectively changing the sign of the real part of the unstable poles. As r_0/r_1 becomes very large the emphasis is placed on system transient behavior and the closed-loop time constants become ever smaller with increased control exercise. The pole locus tends to form a semicircle of increasing radius in the left-half plane assuming the Butterworth filter pole locations. When zeroes are present in the transfer function the appropriate number of poles move to cancel the zeroes or tend toward the mirror-image location if the zero is right-half plane. Thus the optimal controller can in principle produce a response that is arbitrarily fast approximating the Butterworth filter response with the filter bandwidth determined by r_0/r_1. The important exception to this behavior occurs

when low-frequency right-half plane zeroes are present as is often the case in switching converters (e.g. boost and buck-boost converters have right-half plane zeroes in their duty ratio to output voltage transfer function). In this case the closed-loop response will be dominated by the pole assuming the mirror image location of the zero, severely limiting theoretical performance possibilities.

Figure 6.3 illustrates the optimal s-plane pole loci for two conditions, one where the poles and zeroes reside exclusively in the left-half plane, and one where they are in the right-half plane. Since the optimal control with minimal effort simply reverses the sign of the real part of unstable poles and the roots tend toward the mirror image of right-half plane zeroes, the two loci are identical.

6.6 Review

This chapter merely laid some groundwork for the application of optimal control theory to the design of switching regulators. An entire volume could easily be compiled on this and other related topics from the theory such as existence and uniqueness of solutions, state reconstruction, and optimal estimation. These subjects are left as possible areas for further study based on the foundations provided herein.

Linearized small-signal dynamic equations for a general constant-frequency duty-ratio-controlled switching converter with two switched topologies per period were derived using the state-space-averaging approach. The linear model of the dynamics was then used in conjunction with established methods of modern control to form procedures for generating linear optimal state-feedback control for switching converters.

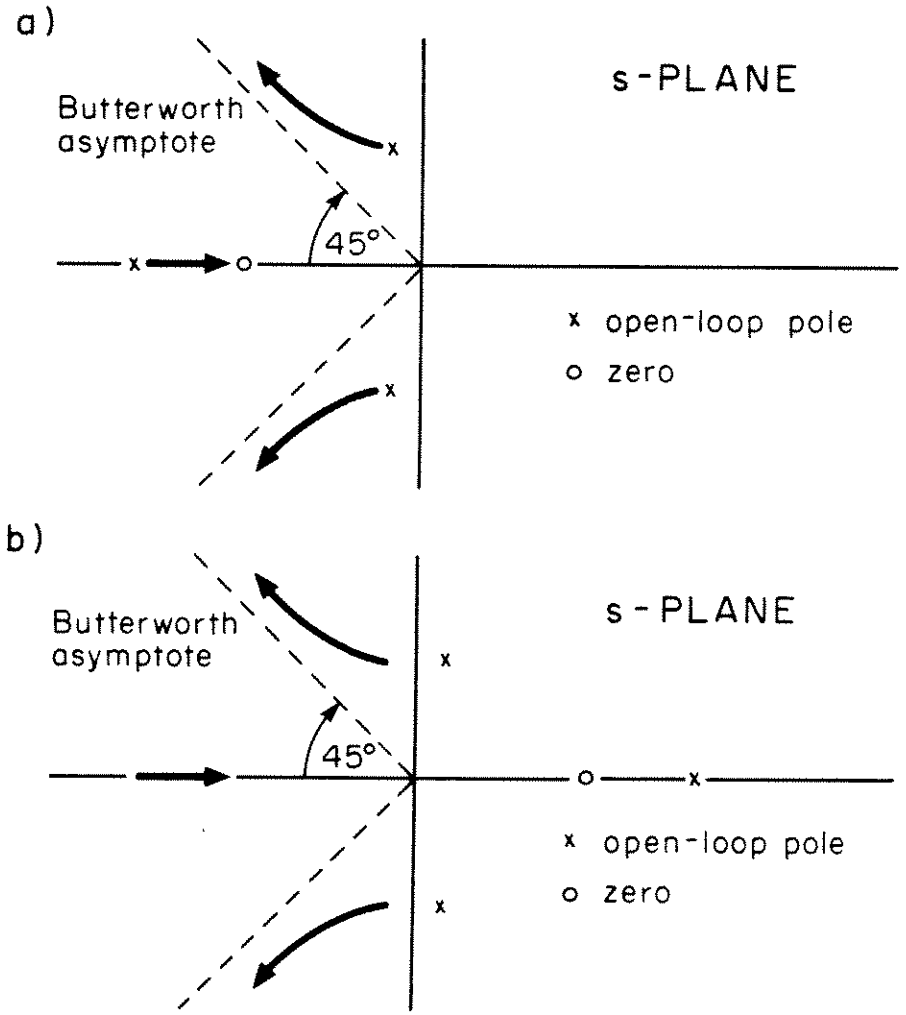

Fig. 6.3 Example behavior of s-plane root loci shown in bold lines for optimally regulated converters; a) left half-plane open-loop poles and zeroes, b) right half-plane poles and zeroes. Stable configurations result irrespective of open-loop dynamics with loci moving in the direction of the arrows with decreasing penalty on control effort.

Two examples illustrated methods for obtaining the solution for the feedback gains and gave specific closed form results for buck converters.

Even though the examples relied on hand calculations, the great utility of this method lies in the fact that the approach is general for switched state converters and may be automated on a digital computer. The most difficult step in the process may be in arriving at a suitable choice of penalty function. This approach admittedly lacks some of the foresight provided by applying classical control techniques to obtain the desired closed-loop regulation. However, a great deal of the burden of analysis may be laid on the digital computer and the result can be said to be the best with respect to a given criterion. The effectiveness of the method can be evaluated with classical control techniques by analysis of the optimal closed-loop system which results from a particular choice of performance index. In cases where the system is of high order (many independent states) and/or multi-input, multi-output, optimal state vector feedback may be distinctly the most desirable method of obtaining stable regulation and good transient characteristics.

CHAPTER 7

DISCRETE FORMULATION OF REGULATOR DYNAMICS

with

APPLICATIONS TO CURRENT PROGRAMMING

The previous chapter established modern control theory design techniques for switching converters predicated on a system dynamic model consisting of state variable differential equations generated with the state-space-averaging method. The techniques developed in the present chapter rely on identical linearizing assumptions to produce a model expressed in terms of state variable difference equations describing the sampled-data system dynamic behavior. The difference equations comprising the discrete formulation of the regulator dynamics predict the evolution of the state vector by a time sequence of instantaneous values related to initial conditions and control exercise.

Although cursory examination of the relative merits of the continuous and discrete models suggests that the sampled-data approach contains less information, the converse is actually true. Switching converters contain an inherent sampling process that limits the accuracy of linearized models to predicting effects that have frequency components less than half the switching frequency. This limitation is implicit in the discrete model and is a well-known constraint on the application of continuous representations. The difference equations, however, contain the switching period T_s, an additional item of information. Advantages obtained by inclusion of the sampling rate in the model are increased capability in

predicting effects present near half the switching frequency, such as sampling induced instability, and more accurate representation of rapid transient behavior, such as the finite-settling-time response discussed in this and the following chapter. Even though the discrete model possesses certain unique advantages, it has drawbacks that prevent it from supplanting the continuous approach and is currently best employed harmoniously with classical technique. The examples of this chapter and the next are chosen to spotlight the strong points of the discrete method which is shown capable of generating important results. Limitations of the sampled-data description stem from its emphasis on time-domain transient behavior and resultant difficulty in relating the analysis to the familiar frequency domain techniques of classical control design. The reader is forewarned to remain cognizant of such limitations while the exposition emphasizes the method's advantages.

After establishing a time-domain system description in terms of state transition equations, the z-transform is introduced and applied to facilitate analysis of the model. Then, in keeping with the theme of using these techniques in conjunction with classical design results, the interrelation between the z and s domain descriptions is discussed and relationships are introduced that allow the designer to move bidirectionally between the z-domain model and the s-domain state-space-averaged model, such that either analysis method may be conveniently applied where it is most appropriate. Thus, for instance, the z-domain may establish the presence or absence of sampling induced oscillations when the s-domain analysis predicts system bandwidths that are a substantial fraction of the switching frequency. In this manner a design may be generated using classical frequency response

technique, or the optimal control method of Chapter 6, and then checked for the destabilizing effects of sampling if the engineer deems it necessary.

The general time-domain development of the model and the implications interpreted in the z and s domain may seem too recondite for practical application in engineering design by all but the most industrious engineer. To dispel this notion one example chosen to illustrate the methods of this chapter is very simple, and is of considerable practical importance. The control of a single inductive-current state variable is analyzed by several techniques to give the reader a multifaceted understanding of current feedback control that will enable him to predict performance in a variety of ways, some of which are so simple that they are useful for approximate laboratory-bench design manipulation with a minimum of calculation.

A more ambitious application of this discrete approach is reserved for the next chapter where the solution for finite-settling-time state-feedback gains is developed for a switching regulator of arbitrary system order and substantiated by a second-order circuit realization.

7.1 The linearized difference equation model

Since the development of the linearized discrete system representation closely parallels the system linearization described in Chapter 6 for the continuous model, it will not be necessary for clarity to limit to two the number of switched topologies each cyclic period. The initiation into the similar methods used in the previous chapter will serve to help the reader negotiate a development generalized to multiple switched topologies. Thus, the derivation here at first will be more general, to show how these methods can easily be adapted to include many switched subintervals, but

ultimately will focus on the common fixed-frequency two-topology duty-ratio-modulated configurations.

Consider a switching converter that may be accurately described by linear differential equations during each of its switched topologies. In any of the periodically switched configurations the state equations may be written as

$$\dot{x} = A_i x + B_i u \tag{7.1}$$

and the converter output usually may be expressed by

$$y_i = C_i^T x \tag{7.2}$$

where the subscript i indexes each subinterval. Generally x, u, and y are vectors representing the system state, control, and output respectively. Information about the system dynamics and output relationships during the i^{th} switched state topology is contained in the matrices A_i, B_i and C_i^T. These state-space descriptions are generally applicable to linear systems and are well established as a compact expression of an n^{th} order differential equations in terms of a first-order matrix differential equation, governing the behavior of an n-element vector dependent variable. The exact behavior of x and y may be obtained by solving each of the sequence of differential equations with the initial condition on x determined by the final value of the solution for the previous switched interval. If A_i, B_i and u are invariant during an interval for which the solution to (7.1) is desired, then the expression for x(t) assumes a simple exponential form analogous to the solution of a scalar first-order differential equation. If x(0) denotes the initial condition on x, the solution may be written as

$$x(t) = e^{A_i t}x(0) + A_i^{-1}(e^{A_i t} - I)B_i u(0) \tag{7.3}$$

In (7.3) I is the identity matrix and $e^{A_i t}$ is the exponential matrix, which is the solution to the matrix differential equation (7.4) [17].

$$\frac{d}{dt}\underline{\overline{X}} = A_i\underline{\overline{X}} \; ; \; \underline{\overline{X}}(0) = I \tag{7.4}$$

An equivalent definition of $e^{A_i t}$ is given in the form of an infinite series;

$$e^{A_i t} = I + A_i t + \frac{(A_i t)^2}{2!} + \frac{(A_i t)^3}{3!} + \ldots \tag{7.5}$$

The reader may verify that (7.3) is a solution to (7.1) under the given assumptions by differentiating (7.3) and applying definition (7.5). The result is equation (7.1). If the time interval t is sufficiently small then $e^{A_i t}$ is well approximated by the first two terms of its series representation (7.5).

$$e^{A_i t} \simeq I + A_i t \tag{7.6}$$

Under approximation (7.6) the solution (7.3) becomes (7.7).

$$x(t) \simeq (I + A_i t)x(0) + B_i u(0)t \tag{7.7}$$

It can be seen by differentiation and substitution that (7.7) is also a solution to (7.1), but it is not the complete solution. It is complete only to the extent that the neglected higher order terms in (7.5) are sufficiently small. This is tantamount to describing the scalar exponential by a straight line [18]. Such an approximation is generally very good in switching converters [1] since by design $|A_i t|$ is made small

to minimize switching ripple. In addition, A_i often contains eigenvalues with negative real parts and so (7.5) may be viewed as an alternating series which is very rapidly convergent. Hence the straight line approximation (7.6) is usually quite accurate and (7.7) is a simplified but still useful solution to (7.1).

A common practice in switching converter design is to make the switching sequence cyclic with period T_s and effect control over the system by varying the fractions of T_s each subinterval occupies. Since we seek to reveal the influence of such control action on the state and output vectors it is desirable to determine how the state vector changes during a period T_s as a function of the subinterval durations. This desired solution may be obtained exactly by repeated application of (7.3) with $t = t_i$, the length of the i^{th} subinterval. Unfortunately the solution is unwieldy and nonlinear with respect to t_i, which greatly diminishes its usefulness. If one accepts the accuracy of (7.7), the solution then assumes a much simpler form:

$$x(T_s) = \prod_{i=1,k} (I + A_i t_i)\, x(0) + \sum_{i=1,k} B_i u(0) t_i \prod_{j=i+1,k} (I + A_j t_j) \qquad (7.8)$$

In (7.8) k is the number of subintervals, Π indicates product and Σ indicates summation. Notice that (7.8) is still fairly complicated and nonlinear since it contains products of the t_i. The t_i are not all independent because they are related by

$$\sum_{i=1,k} t_i = T_s \qquad (7.9)$$

and so the products in (7.8) contain dependence on t_i^2. To be consistent with previous assumptions and to reveal the linearized dependence of $x(T_s)$ on the t_i, the higher order terms in (7.8) may be neglected and only the first order terms retained.

$$x(T_s) = \left[I + \sum_{i=1,k} A_i t_i\right] x(0) + \sum_{i=1,k} B_i u(0) t_i \tag{7.10}$$

Equation (7.10) is the linearized solution for $x(T_s)$ and reveals the average linearized derivative of x with respect to time as

$$\frac{d}{dt}x = \frac{1}{T_s} \sum_{i=1,k} \left(A_i x + B_i u(0)\right) t_i \tag{7.11}$$

The statement of (7.11) is the pith of the state-space-averaged method of S. Ćuk [1], which may be obtained directly from (7.10) by averaging the derivative over one period. Thus it is manifest that the assumptions made in arriving at (7.10) are equivalent to the state-space-averaging postulates.

With equation (7.9) in mind it is clear that modulation of one t_i must be at the expense of some or all of the other intervals. If the case of two switched topologies in each period T_s is examined, then the control effect will be exposed in the simple circumstance where increasing the first interval directly diminishes the second. This case is of considerable practical significance since many converters operate with two switched state topologies and are controlled by duty-ratio modulation. Once the simple case is understood, more complicated schemes for choosing

multiple t_i can be evaluated by superposition, since the model is linear. In pursuit of such an option, let $t_1 = DT_s$ and and $t_2 = D'T_s = (1-D)T_s$ then (7.10) becomes

$$x(T_s) = (I + A_1DT_s + A_2D'T_s)\, x(0) + (B_1D + B_2D')T_s u(0) \qquad (7.12)$$

Now, to find the system small signal response, add modulation terms, indicated by a caret, to the duty ratio and the state and control vectors so that D is replaced with $D + \hat{d}$, x with $x + \hat{x}$ and u with $u + \hat{u}$ in (7.12) which generates

$$\begin{aligned}(x + \hat{x})(T_s) = (I + A_1DT_s + A_2D'T_s + [A_1-A_2]\hat{d}(0)T_s)(x + \hat{x})(0) \\ + (B_1D + B_2D' + \left[B_1-B_2\right]\hat{d}(0)T_s)(u + \hat{u})(0)\end{aligned} \qquad (7.13)$$

Equation (7.13) contains terms including products of the perturbations, which are assumed small. In keeping with the desire for a linear description, these perturbation products are neglected in expanding (7.13). Then subtraction of (7.12) from the expansion of (7.13) yields the ac small-signal system characteristics stated in (7.14):

$$\begin{aligned}\hat{x}(T_s) = (I + A_1DT_s + A_2D'T_s)\hat{x}(0) + (B_1D + B_2D')T_s\hat{u}(0) \\ + [(A_1 - A_2)x(0) + (B_1 - B_2)u(0)]T_s\hat{d}(0)\end{aligned} \qquad (7.14)$$

For convenience in notation define

$$\begin{aligned}F &= (I + A_1DT_s + A_2D'T_s) \\ B &= (B_1D + B_2D')T_s \\ h &= [(A_1 - A_2)x(0) + (B_1 - B_2)u(0)]T_s\end{aligned} \qquad (7.15)$$

where

$$x(0) = -(A_1 D + A_2 D')^{-1}(B_1 D + B_2 D')u(0) \tag{7.16}$$

from the steady state solution of (7.12), and u(0) is taken as its nominal value. Then (7.14) may be written concisely as

$$\hat{x}(T_s) = F\hat{x}(0) + B\hat{u}(0) + h\hat{d}(0) \tag{7.17}$$

which tells us how the ac state vector propagates in the linear sense during any switching period T_s, subject to initial conditions $\hat{x}(0)$ and control influences $\hat{d}(0)$ and $\hat{u}(0)$. Equation (7.17) is a state-variable difference equation describing the converter open-loop dynamics. If, as developed in Chapter 6, the duty ratio modulation is determined via constant gain state feedback, then the control law for the converter may be written as

$$\hat{d}(0) = -K^T\hat{x}(0) \tag{7.18}$$

Substitution of (7.18) into (7.17) then produces the closed-loop state-variable difference equation (7.19)

$$\begin{aligned} \hat{x}(T_s) &= M\hat{x}(0) + B\hat{u}(0) \\ M &= (F - hK^T) \end{aligned} \tag{7.19}$$

Equations (7.17) and (7.19) are linear difference equation models for converter and regulator ac dynamics, and as such embody the attainment of this section's objectives.

7.2 Z-transform analysis

Just as the Laplace transform reduces time-domain differential equations to algebraic equations in the complex transform variable s,

the z-transform recasts difference equations in terms of z. Since the first-order difference equations (7.17) and (7.19) are of particularly simple form generation of their z-domain representations and their subsequent analysis requires only rudimentary knowledge of the z-transform. In the following discussion an elementary understanding of both transform methods is assumed and only those points of particular significance to the subject at hand are developed. There are many good texts available to provide background material among which [19] and [20] are recommended.

The z-domain analysis of system transfer characteristics, impedances and loop gain is quite similar to its s-domain counterpart. For illustrative purposes the closed-loop dynamics will be analyzed. Application of the techniques to the open-loop plant should be obvious, since a mere change of matrix nomenclature is all that is required. If (7.19) is transformed to reveal the z-domain counterpart of the difference equation, the result is

$$z\hat{x}(z) - z\hat{x}(0) = M\hat{x}(z) + B\hat{u}(z) \tag{7.20}$$

In (7.20) $\hat{x}(z)$ indicates that $\hat{x}(t)$ has been appropriately transformed, not a mere substitution of z for t in the expression for $\hat{x}(t)$. A little manipulation of (7.20) results in

$$\hat{x}(z) = (zI-M)^{-1}(z\hat{x}(0) + B\hat{u}(z)) \tag{7.21}$$

a familiar form for those acquainted with transform analysis. Response to initial conditions or transfer functions from the control $\hat{u}(z)$ to any state or linear combinations of states are readily available in terms of the complex variable z from the expansion and manipulation of the vector equation (7.21). Note that the inverse of zI-M plays a crucial role

in determining the form of $\hat{x}(z)$, and that the eigenvalues of M are the z-domain singularities of $\hat{x}(z)$. Closed-loop system stability is contingent on all characteristic values of M residing within the unit circle in the complex z-plane.

As a first illustrative example of the usefulness of z-domain analysis, let us revisit the buck converter of Chapter 6 whose regulation is effected in an optimal fashion by total-state feedback. The buck regulator under consideration is shown in Fig. 7.1. Both the inductor current and the capacitor voltage are sensed and duty ratio control results from a linear combination of detected errors. Current and voltage error gains, K_1 and K_2, determine the relative weight given to their respective states. Recall that, in Section 6.4, use of the Kalman equation approach, coupled with a continuous linearized model of the converter, produced an expression for the relationship of K_1 and K_2 that yields the best voltage transient response. There it appeared that one may choose K_1 and K_2 as large as one pleases, procuring an ever more rapid transient, without invoking the penalty of instability, as long as the gains are related by eqn. (6.47), repeated here for convenience:

$$K_1 = \sqrt{2K_2L/(V_gC)} \tag{6.47}$$

Certainly we know that the system bandwidth cannot exceed one-half the switching frequency, but we are not intuitively aware of how close to this limit we may come, or what the implication is for K_1 or K_2. For a definitive answer we may resort to z-domain analysis.

The method is straightforward. The eigenvalues of the closed-loop

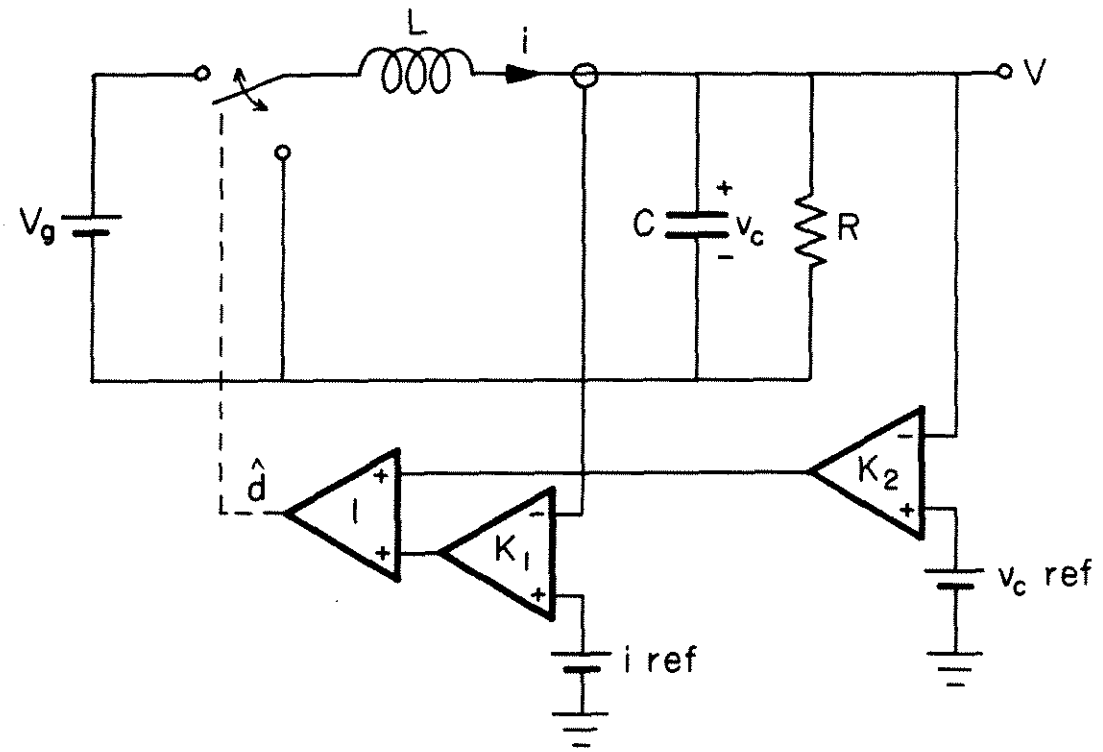

Fig. 7.1 State-vector-feedback buck regulator returns both current and voltage error signals to determine duty-ratio modulation control.

system are examined in root locus fashion with K_2, the voltage gain, as the parameter. In accordance with the modelling methods of this chapter we seek to form the matrix M. Equation (7.11) demonstrated that there is a close correspondence between this discrete formulation and the state-space-averaged method [1] used in Chapter 6. Advantage may be taken of this fact to facilitate development of M from the work of Chapter 6. Alternative definitions to (7.15) for F and h are

$$\begin{aligned} F &= I + AT_s \\ h &= gT_s \end{aligned} \tag{7.22}$$

where A and g are the state-space-averaged response matrix and forcing vector used in (6.10), shown here for clarification:

$$\dot{\hat{x}} = A\hat{x} + g\hat{d} \tag{6.10}$$

Thus we may directly write

$$F = \begin{bmatrix} 1 & -\frac{T_s}{L} \\ \frac{T_s}{C} & 1-\frac{T_s}{RC} \end{bmatrix} \tag{7.23}$$

and

$$h = \begin{bmatrix} \frac{V_g T_s}{L} \\ 0 \end{bmatrix} \tag{7.24}$$

from the work of the previous chapter. Use of (7.19) gives

$$M = \begin{bmatrix} 1 & -\frac{T_s}{L} \\ \frac{T_s}{C} & 1-\frac{T_s}{RC} \end{bmatrix} - \begin{bmatrix} \frac{V_g T_s}{L} \\ 0 \end{bmatrix} \begin{bmatrix} K_1 & K_2 \end{bmatrix} \tag{7.25}$$

or more compactly,

$$M = \begin{bmatrix} 1 - \frac{K_1 V_g T_s}{L} & -\frac{K_2 V_g + 1}{L} T_s \\ \frac{T_s}{C} & 1 - \frac{T_s}{RC} \end{bmatrix} \tag{7.26}$$

which is the desired result. Now, we need to form zI-M thus:

$$zI-M = \begin{bmatrix} z + \frac{K_1 V_g T_s}{L} - 1 & \frac{K_2 V_g + 1}{L} T_s \\ -\frac{T_s}{C} & z + \frac{T_s}{RC} - 1 \end{bmatrix} \tag{7.27}$$

To complete the example, specific converter values are needed. Consider $T_s = 100(10^{-6})$sec, L = 1 mH, C = 1000 μF, R = 10 Ω, and V_g = 10 V. Then (7.27) reduces to

$$zI-M = \begin{bmatrix} z-1 + K_1 & K_2 + .1 \\ -.1 & z-.99 \end{bmatrix} \tag{7.28}$$

and (6.47) assumes the form

$$K_1 = \sqrt{.2K_2} \tag{7.29}$$

The only work that remains is to evaluate the determinant of zI-M in (7.28) for its zeroes while varying K_2, with K_1 constrained by (7.29). When this is done, the answers form the root locus plot of Fig. 7.2.

Since the roots occur in complex conjugate pairs, only half of the entire locus need be shown, the other half being a mirror image. With $K_2 = 0$, the locus lies near the +1 point in the plane, corresponding to the natural open-loop LC resonant pair. As K_2 in increased, and K_1

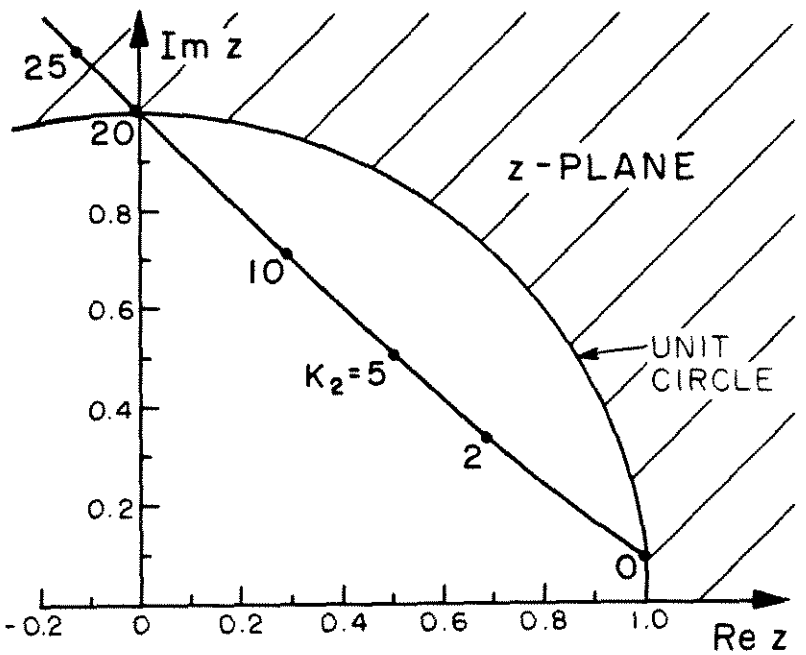

Fig. 7.2 Z-domain root locus for a state-vector-feedback buck regulator using the optimal control gains derived in Chapter 6 for the continuous time model.

accordingly, the locus moves across the unit circle until, at K_2 about 20, the roots occupy ± j1.0. This is indicative of impending oscillation at one-quarter the switching frequency and prescribes the confines on upper choice of K_2, with K_1 given by (6.47). This evinces the ability of the discrete formulation to warn of possible instability when large system bandwidths are predicted by the continuous model. With the gains related optimally, the continuous representation shows no possibility of instability. However, the discrete model, based on the same approximations, accounts for the effects of sampling and is able to determine the upper limit on bandwidth. Use of both methods in design allows an optimal s-domain pole placement, approximating the Butterworth configuration, while still ensuring that the gains are not chosen so large that the discrete model predicts instability. It should be obvious that in this case the

discrete modelling complements the continuous.

As a second example, it is instructive to entertain the concept of loop gain, as applicable to the general case of state-vector feedback. Since the duty-ratio modulation comprises a single control input port, it is always possible in this circumstance to define a loop gain for the regulator which is the quantity that could, in principle, be measured by breaking the signal path at the modulator, injecting a test signal, and measuring the resultant signal returned by the feedback system to the signal injection point, as illustrated in Fig. 7.3 for a buck regulator. In practice, difficulty is often encountered when the loop is broken for measurement purposes, but the technique illustrated serves to identify by example the existence of a single measurable quantity that is the loop

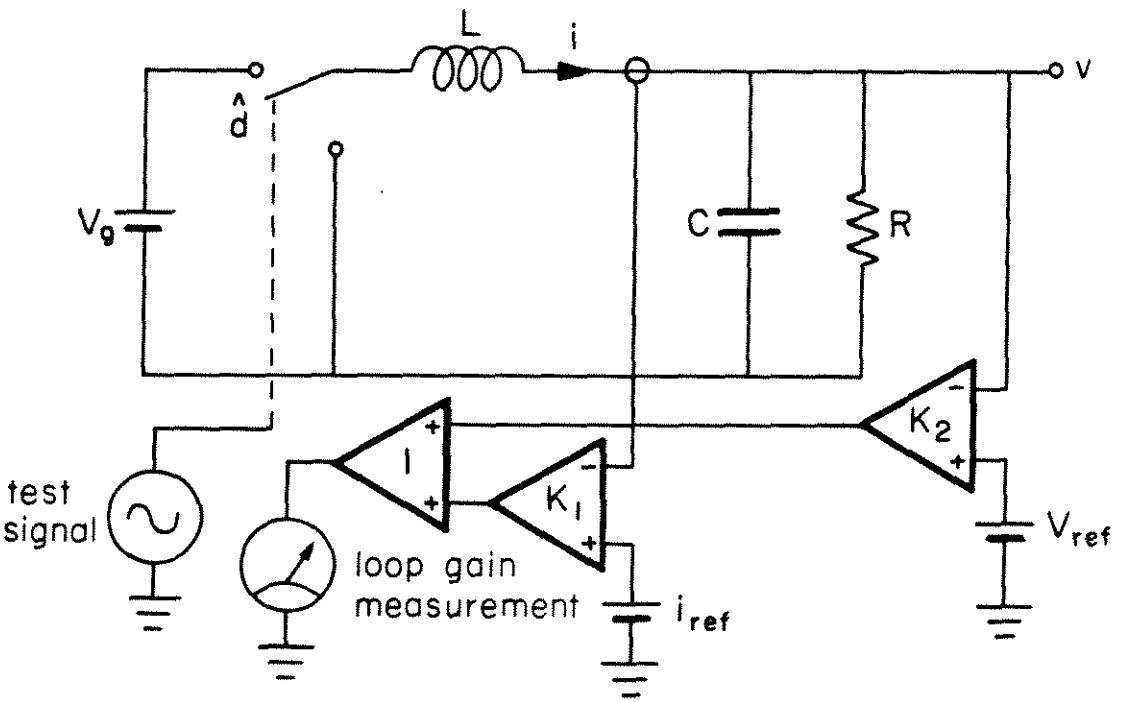

Fig. 7.3 Loop gain measurement for a state-feedback buck regulator.

gain for a state-feedback control system. Measurements on the example circuit of the next chapter are made by means of a more sophisticated method which circumvents practical problems with opening the loop. The z-transform prediction for the loop gain measurement may be obtained by massaging an abbreviated (7.17) and the control law (7.18), whose z-transforms are given in (7.30) and (7.31) respectively:

$$\hat{x}(z) = (zI-F)^{-1}(z\hat{x}(0) + h\hat{d}(z)) \tag{7.30}$$

$$\hat{d}(z) = -K^T\hat{x}(z) \tag{7.31}$$

From the discussion above and the specific example of Fig. 7.3 one may realize that the expression for the loop gain will appear in a recursive equation for $\hat{d}(z)$ which may be generated by use of (7.30) in (7.31). The result is

$$\hat{d}(z) = -K^T(zI-F)^{-1}(z\hat{x}(0) + h\hat{d}(z)) \tag{7.32}$$

where the loop gain, $T(z)$, is readily identified as

$$T(z) = K^T(zI-F)^{-1}h \tag{7.33}$$

when the sign inversion for negative feedback is taken into account. Such a loop gain has been derived and used in conjunction with z-plane root locus methods for state-feedback design for systems of low order [18]. The equation is easily obtained, but as is the case for most z-domain expressions, interpretation and laboratory verification by the usual frequency response procedure proves difficult. The complication stems from the fact that a frequency response on (7.33) involves allowing z to equal $e^{J\omega T_s}$, and so the expression takes the form of a ratio of polynomials of complex exponentials of ω. The assistance in understanding

provided for the s-domain counterpart by the Bode diagram is absent. As such, there is much to be gained by developing the relationship directly between the linearized z-domain and the state-space-averaged s-domain converter descriptions, since one then accrues numerous alternate avenues of attack on the control problem and finds adequate support from standard laboratory measurements. In particular, one seeks to avail oneself of the state-space-averaged describing function result without resorting to the fundamental descriptions. Motivation for the endeavor of the next section is thus provided.

7.3 Transformation to state-space averaging

Consider the state-space-averaged open-loop dynamic equation (6.10) as a representative specimen.

$$\dot{\hat{x}} = A\hat{x} + g\hat{d} \tag{6.10}$$

The Laplace transform solution to this time-domain equation, with initial conditions disregarded, is used for purposes of predicting describing function results measured in the laboratory. The solution is

$$\hat{x}(s) = (sI-A)^{-1}g\hat{d}(s) \tag{7.34}$$

This representation with $s = j\omega$ is solidly established as a means for predicting frequency characteristics of switching converters. The parallel equation to (6.10) in the present descrete-time development is (7.17) which when written in abbreviated form is

$$\hat{x}(T_s) = F\hat{x}(0) + h\hat{d}(0) \tag{7.35}$$

The z-transform solution to this equation, again with initial conditions ignored, may be used for z-domain frequency response, with the complications

cited in the previous section. The solution is

$$\hat{x}(z) = (zI-F)^{-1}h\hat{d}(z) \tag{7.36}$$

It is well known that the z-domain and s-domain are related by $z = e^{sT_s}$, and in fact this statement is sometimes used to define the z-transform [20]. The development of both (6.10) and (7.35) was predicated on the accuracy of a two-term approximation to the exponential matrix. So, instead of dealing with the definitive relationship between the two transform domains, one may try an approximate substitution in (7.36) to see what results. Let us try

$$z = 1 + sT_s \tag{7.37}$$

in keeping with the postulates supporting both models. Again we approximated the exponential by its first two terms. Substitution of (7.37) into (7.36) and the assumption that the transformation from the linearized z-domain to the state-space-averaged s-domain is effected results in

$$\hat{x}(s) = [(1 + sT_s)I-F]^{-1}h\hat{d}(s) \tag{7.38}$$

If (7.38) is further expanded by use of relations (7.22) the outcome is

$$\hat{x}(s) = [(1 + sT_s)I-I-AT_s]^{-1}gT_s\hat{d}(s) \tag{7.39}$$

which reduces to

$$\hat{x}(s) = (sI-A)^{-1}g\hat{d}(s) \tag{7.40}$$

and justifies the supposition that the transformation occurred. It may be seen that (7.40) agrees exactly with (7.20), so the substitution (7.37) transforms the z-domain straight-line model to the s-domain state-space-averaged model, provided initial conditions may be ignored and a steady-

state solution exists. Thus, if a transfer function, impedance, admittance, etc. is obtained with the z-domain model, the state-space-averaged prediction may be recovered without resorting to fundamentals by use of (7.37). It is worth stressing the fact that the transformation (7.37) exactly relates the predictions of the two models, even though it is only an approximation to the mathematical relationship between the transform domains.

To illustrate the utility of the transformation, (7.37) may be inverted and used to map the z-domain root locus and the unit circle of Fig. 7.2 onto the s-plane, as shown in Fig. 7.4. One may then see that the state-space-averaged locus, indicated by dots, moves toward the dashed asymptote, drawn at a 45° angle, as the gain is increased. This behavior is precisely what is anticipated for the optimal design. From the discussion of Section 6.5 on optimal pole location, we know that the poles should approach a Butterworth configuration as the gain becomes large. For a second-order plant, the locus should thus eventually lie along 45° asymptotes in the left half-plane. In light of this interpretation, it is not at all surprising that the root locus crosses the unit circle at quite precisely one-quarter of its circumference since that is where the asymptote intersects.

Another interesting observation may be made from Fig. 7.4. The area slashed out in the s-plane corresponds to pole locations which are said to be stable by state-space-averaging, but are judged unstable by the linearized-discrete z-domain criterion. One should note that the discrepancy is not always found at high frequencies, as is the case with the

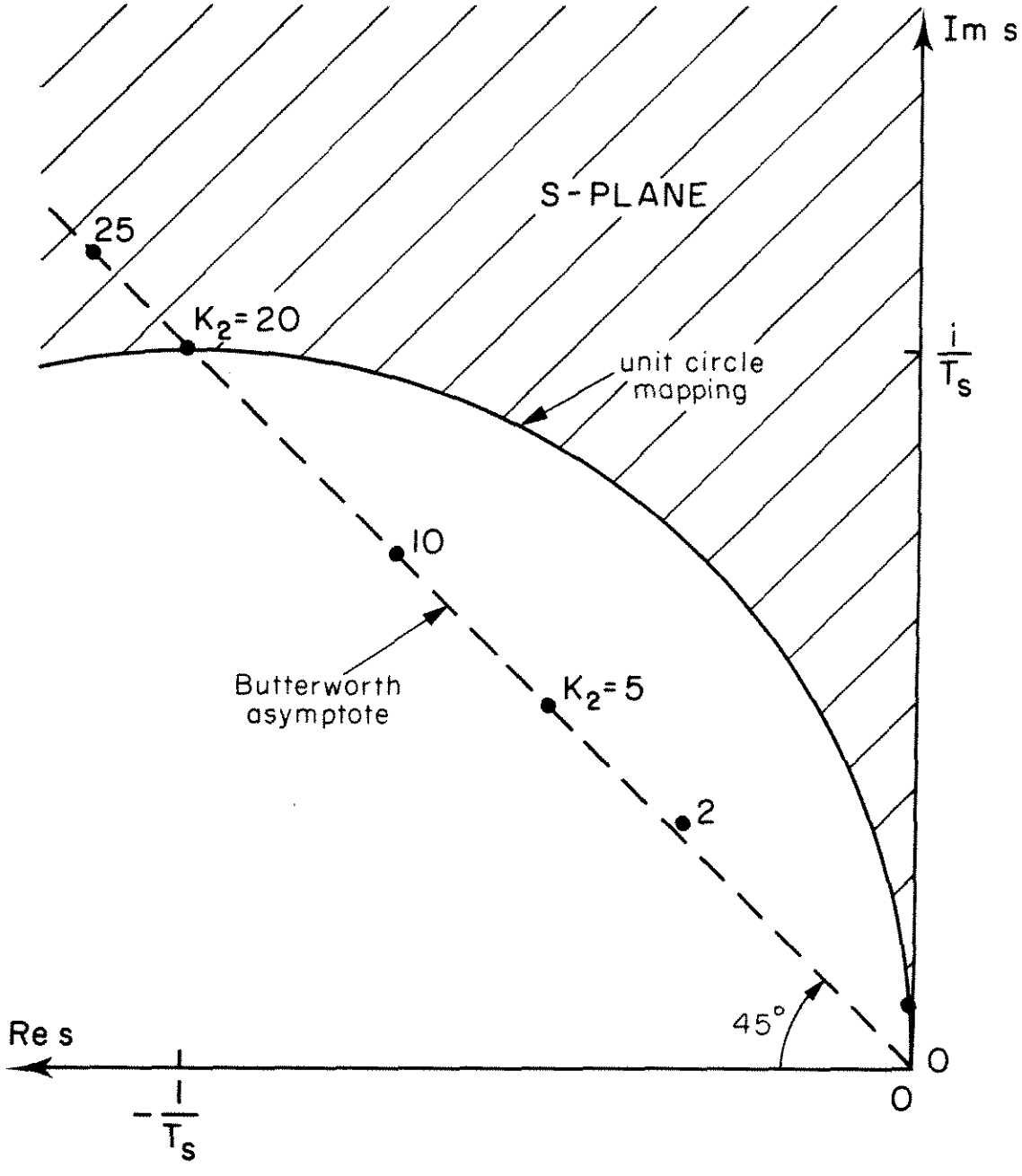

Fig. 7.4 State-space-averaged s-plane pole locus prediction obtained from the z-domain locus of Fig. 7.2 by use of the transformation $s = (z-1)/T_s$.

locus plotted. It is easily possible to conjure up a situation where the state-space-averaged poles lie near the imaginary axis but at a low frequency. In such a circumstance there will still be a conflict between the stability predictions, even though the effects of sampling should be minimal. An example used in the next chapter has just such an occurrence with open-loop poles. In that event, clearly the state-space-averaged answer for stability is correct and the discrete model is wrong. Until further analysis can clarify such discrepancies, the conclusion is that one must always exercise engineering judgement when employing approximate models. Once again we see that since each approach has its own strengths and weaknesses the well-versed engineer will know both and remain cognizant of the limitations of each.

7.4 Inductive current control

As a concluding topic for this chapter, an instance is chosen for which there often is particularly vivid evidence of straight lines. In switching converters, the currents flowing in inductors typically display linear waveforms on a monitoring oscilloscope. Not only does this behavior make the current state an ideal candidate for analysis by the methods of the preceding sections, but also it provides a vehicle for further discussion, which leads to important concepts and the subject matter of the next chapter.

The topic of controlling inductive current states is, of course, not new and in fact has received considerable attention. For constant frequency converters, advantage has been taken of the cyclic ramping

behavior to effect control over the current level by means of a comparator, which regulates inductor current magnitude by turning the switch off when the current meets a reference level [21]. Such a scheme can very rigidly determine the current, so that in fact it may appear to have eliminated this state, and reduced the system order. When this point of view is taken the comparator control scheme is aptly called "current programming". Converters operating in the current-programmed mode have certain advantages which have prompted development of modelling techniques for them [10]. The intent of this section is not to examine current programming per se, although the methods of this chapter are applicable. Instead, consideration will be given to normal duty-ratio modulation feedback control of an inductive current state. Small-signal differences are subtle, if any, but that will not be a matter of concern here.

For sake of concreteness, one may consider the following discussion to apply to the inductor current in the buck converter of Fig. 7.5, although one will soon realize that the exposition is not limited to a specific topology. The salient feature of the converter depicted is that the voltages which excite current in L are essentially constant, or at least well approximated as such. This is not a necessary condition for the straight line approximation to be valid, as will be shown in the next chapter, but it simplifies the development by making the line slope easy to see. In continuous conduction mode of operation the inductor current i will appear as shown in Fig. 7.6. Each cycle the current in the inductor ramps linearly upward during the switch on time, and back down when the switch is off. Since the stated objective of this section

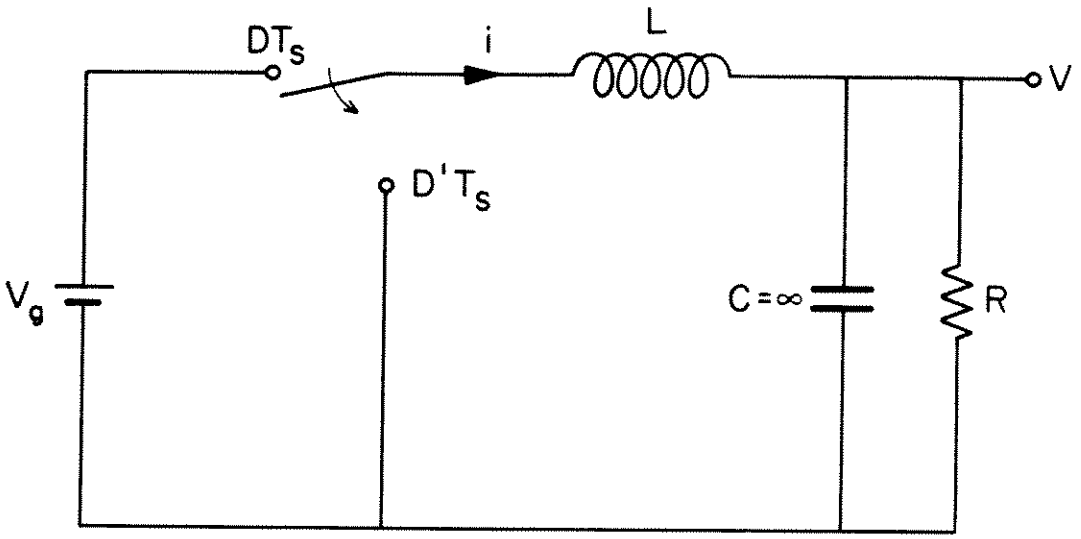

Fig. 7.5 Buck converter with large output capacitor has constant voltage across inductor for either position of the switch.

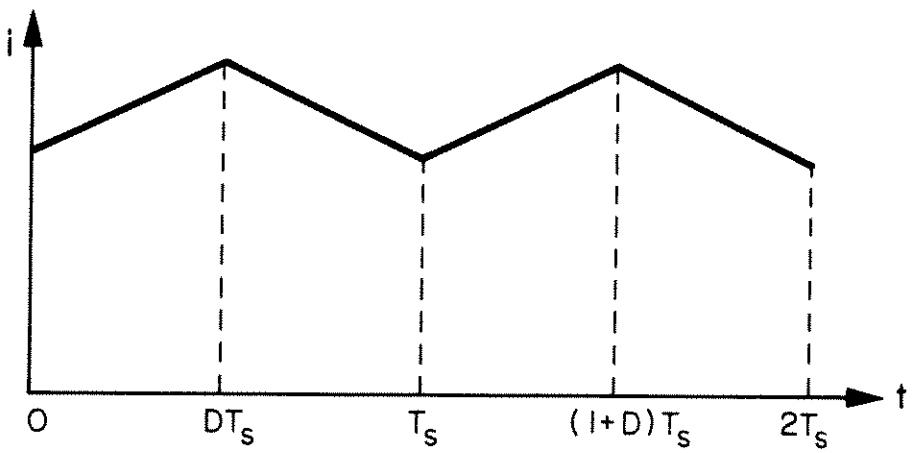

Fig. 7.6 Typical inductive current waveform.

is to examine duty-ratio control, let us perturb the sequence of events shown in Fig. 7.6 by addition of $\hat{d}$ to D in the first cycle. Then the sketch of Fig. 7.7 results. The current level changes by some increment Δi, which remains essentially constant. The level shift does not decay because in this example the output voltage is constant. In an actual converter this situation will be well approximated for our purposes if the natural LC resonance is well below the switching frequency, a common occurrence. Since the relationship between the duty ratio modulation and the resultant current modulation is sought, attention should be focused on the action at the instant the change happens. If the circled area in Fig. 7.8 is magnified for inspection, Fig. 7.9 emerges. The slopes identified in Fig. 7.9 are functions of the inductance value, the voltages involved and the converter operating condition. For steady-state operation it is necessary that $Ds_1 = -D's_2$. The slopes are easily calculated. For the buck converter of Fig. 7.5 $s_1 = (V_g - V)/L$ and $s_2 = -V/L$, where V is given by $V = DV_g$, illustrating dependence on operating condition. One may obtain by inspection of Fig. 7.9 the desired relationship between Δi and $\hat{d}$ given in (7.41).

$$\Delta i = \hat{d} T_s (s_1 - s_2) \tag{7.41}$$

Thus there exists an easily calculable gain constant relating the current and duty ratio modulations.

It appears that by use of (7.41) the current in the buck converter, for example, could be adjusted arbitrarily quickly to some desired reference level. Engineering experience makes one aware, however, that if feedback control is used to adjust the current to a reference, then caution need be exercised lest practical problems make the control

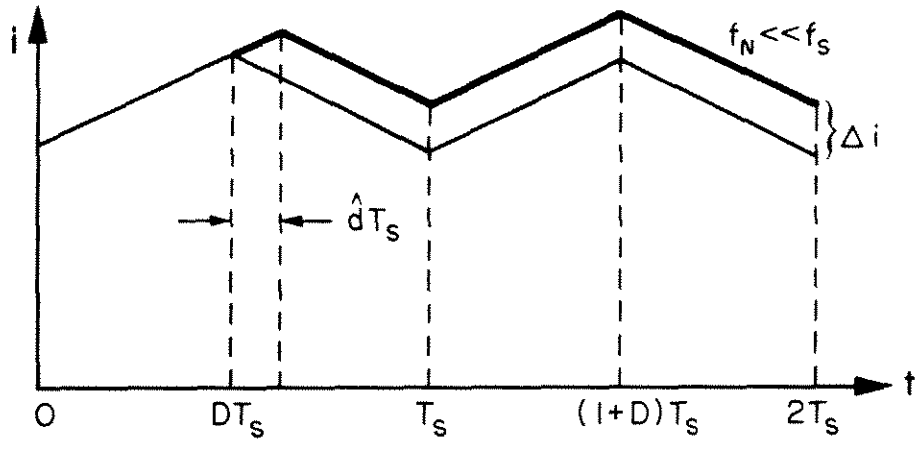

Fig. 7.7 Effect of a single duty-ratio perturbation on the inductive current is indicated by the bold line.

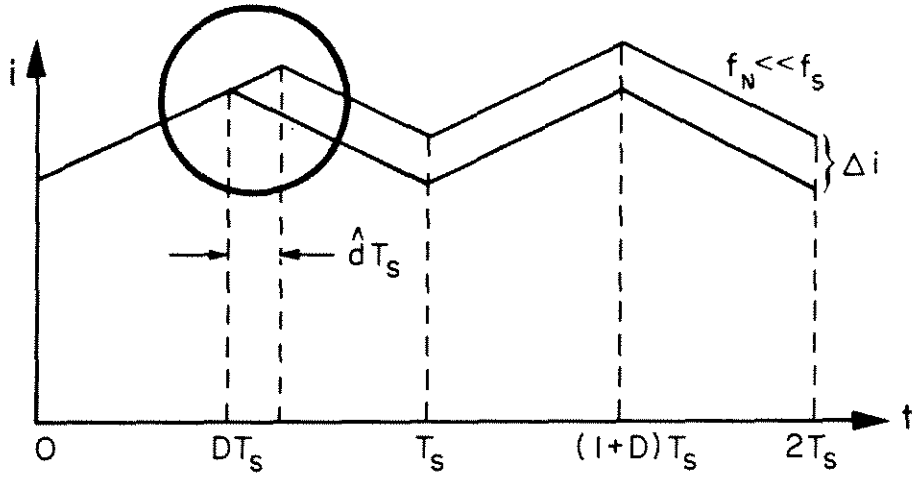

Fig. 7.8 Circle focuses attention on the waveform geometry at the instant of the duty-ratio modulation.

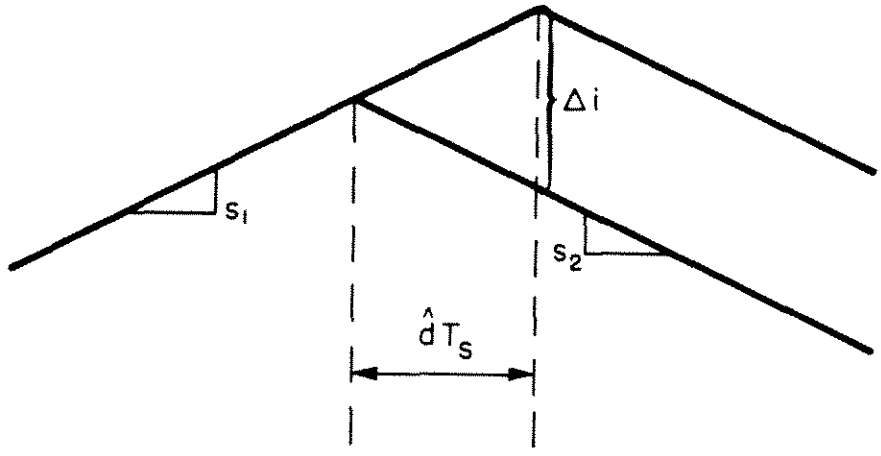

Fig. 7.9 Magnified view of the change in current Δi induced by $\hat{d}$. Current waveform slopes, assumed constant, are identified as s_1 and s_2.

ineffective. One needs to consider factors such as noise susceptibility and neglected control loop lags which may be destabilizing. A particularly familiar way of evaluating regulation effort is by examining the closed-loop bandwidth of the design. The engineer knows that designing for excessive bandwidth invites trouble, even when the system is ostensibly first order. It is therefore desirable to be able to predict what break frequency would result from a given amount of current control effort in response to a sensed error. This may be done, in this case, in a simple and elegant manner with all the work performed in the time domain. There is no need to resort to any transform method whatever in obtaining a basic understanding of current feedback control. Let us then proceed with such an analysis.

Consider the situation where the current deviates by some perturbation from a desired level, shown on an exaggerated scale in Fig. 7.10. When the error $\hat{i}(0)$ is sensed by a regulation loop some duty-ratio control will be exercised to reduce that error in the manner shown in Fig. 7.11. The modulation of the duty ratio required to produce the desired Δi is given by (7.41). Since the current change is in response to the detected error and feedback regulation is assumed here, Δi will be related to $\hat{i}(0)$ by some chosen reduction gain constant r. In this circumstance $\hat{i}(0)$ will be reduced to some lesser value at the end of the period, $\hat{i}(T_s)$, given by

$$\hat{i}(T_s) = (1-r)\hat{i}(0) \tag{7.42}$$

as illustrated in Fig. 7.12. The picture given in Fig. 7.12 has all the information needed to deduce the current break frequency. Notice that every T_s seconds the error decays to 1-r times its initial value. For

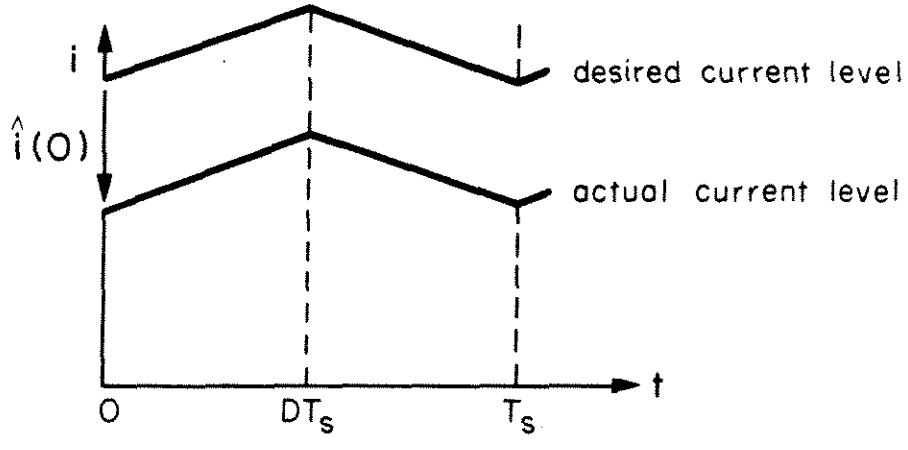

Fig. 7.10 Undesired perturbation on current level shown with actual current less than desired value.

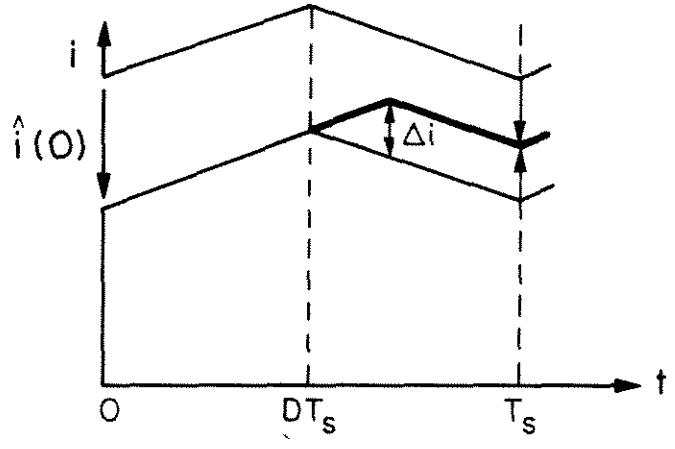

Fig. 7.11 Duty-ratio control acts to reduce the current error magnitude.

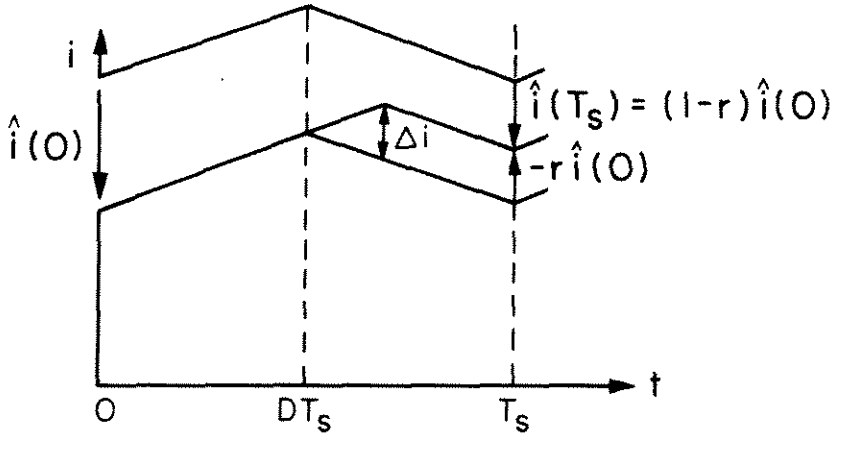

Fig. 7.12 Negative feedback duty-ratio control reduces the current error to a predictable fraction of its initial value every switching cycle. The low frequency response may be modelled as an exponential decay and a closed-loop time constant determined.

a low frequency approximation to this behavior, the ripple at the switching frequency may be ignored and the error reduction likened to an exponential decay, with a decay time constant to be determined in accordance with the behavior shown on the figure. With τ_i denoting the current error decay time constant, the approximation may be written as

$$e^{-T_s/\tau_i} = 1-r \tag{7.43}$$

from which the current break frequency may be derived. Solution for τ_i from (7.43) and conversion of this time constant to a frequency f_i yields, in terms of the switching frequency f_s, the prediction (7.44).

$$f_i = -\frac{\ell n\ (1-r)}{2\pi} f_s \tag{7.44}$$

Thus we see that by the use of straight line approximations and the simple artifice of the exponential decay model, an expression for the current-state response bandwidth results. From (7.41) the control law producing the frequency response of (7.44) is

$$\hat{d} = \frac{-r\hat{i}}{(s_1-s_2)T_s} \tag{7.45}$$

It may seem that the derivation of (7.44) is too simple to give accurate or useful answers. This is definitely not the case. One of the important conjectures in the derivation of (7.44) was that the change Δi persisted without natural decay. This is equivalent to ignoring the natural response matrix F in (7.17). Often one is allowed to do this by the very nature of the current behavior sought. If control is effected to push the response speed well beyond the natural mode, then the supposition in the derivation

is correct to the very extent that it need be. Control induced error decay will dominate, and natural time constants are rightly neglected. When such an estimate is not sufficient, then methods of the previous sections still apply, otherwise, one will find (7.44) and (7.45) simple and very useful relationships.

Rarely, however, in voltage conversion, will a current control loop stand alone. It is often used as a "minor loop" in a voltage regulation scheme involving multiple-state feedback [9]. In this circumstance the current pole location will be influenced by other feedback gains as well as its own. Only if the current response corner frequency is well separated from other system break frequencies can (7.44) be relied on for accuracy. Nonetheless, (7.44) has been used with good results in designing the control loop for the one-kilowatt regulator in [9].

If again attention is turned to Fig. 7.12, one may ascertain from the sketch what choices of r are permissible in terms of stability. If r is less than zero, the error will monotonically increase. If r is greater than 2, the error will increase in an alternating sign sequence, so r is constrained by

$$0 \leq r \leq 2 \tag{7.46}$$

An interesting possibility may occur to one looking at Fig. 7.12. If r is set equal to unity the error will be eliminated entirely in a single cycle. This is called a finite-settling-time decay. Notice that for r equal to unity (7.43) makes no sense. The exponential no longer approximates the decay behavior. For r greater than one, τ_i becomes a complex number. For illumination on these cases one may resort to the z-plane.

Equation (7.42), which represents the time-domain discretized response of the current error, may be transformed into the z-domain in the usual manner which yields

$$\hat{i}(z) = \frac{z\hat{i}(0)}{z-(1-r)} \tag{7.47}$$

It is manifest in (7.47) that the z-domain pole resides at 1-r. If a plot of the z-plane root locus is made, Fig. 7.13 results. Notice that as r varies from 0 to 2 the pole traverses the unit circule along its diameter of the real axis. When r = 0 there is no control exercised and the +1 point in the z-plane corresponds to a persistent error. For r = .5 the decay is one-half each cycle, displayed in the z-plane by a pole at 0.5. When r = 1 the pole is at the origin which indicates the

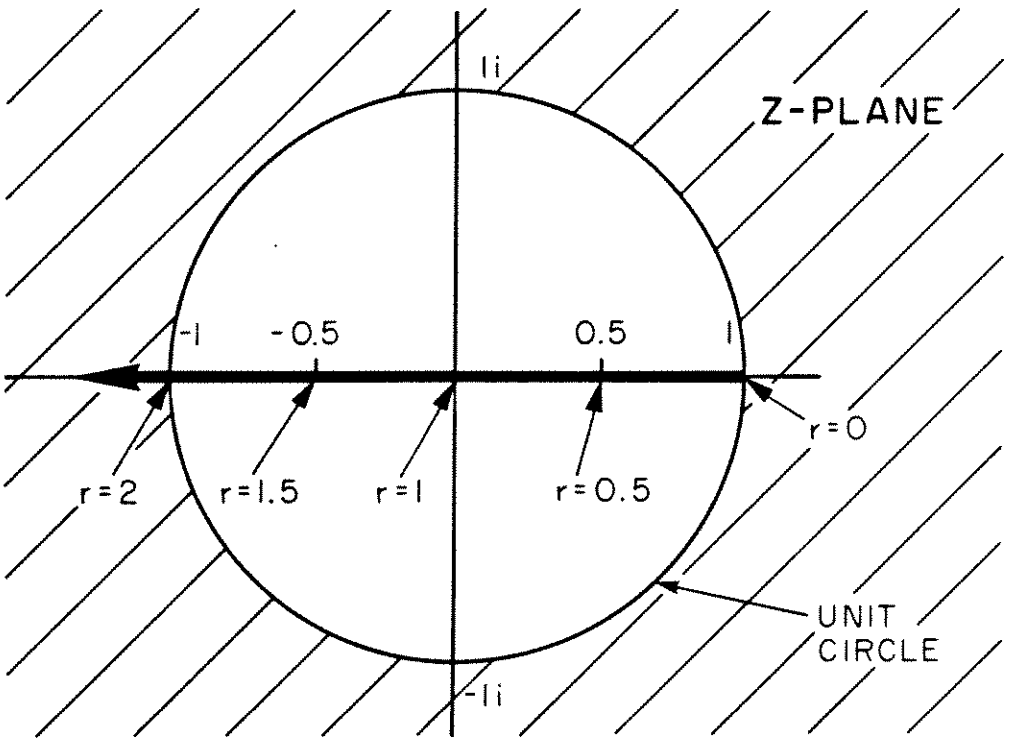

Fig. 7.13 A z-domain root locus shows how the controlled current pole moves as a function of the fractional error reduction per cycle r.

finite-settling-time response. As r is increased beyond 1 the pole moves along the negative real axis, meaning that the response will be oscillatory at half the switching frequency. As r approaches 2, the pole nears the unit circle at -1, and the oscillations become less damped, until, when the pole emerges from the circle, instability results. In this simple example one is easily able to see how the z-plane prediction and the time domain behavior correspond. This gives reinforcement to the previous z-transform analysis and adds an alternative way of viewing the stability bounds (7.46). Additionally, it is easily seen why τ_i becomes a complex number for $r > 1$. The response is sinusoidal in nature, requiring a complex exponential representation.

Now that we have analyzed the current feedback control, postulating $\hat{d}(0)$ a function of $\hat{i}(0)$, one may wonder how such a system could be built. It seems that the large ripple on i would thwart any attempt at feeding back this variable in the usual manner for comparison with a pulse-width-modulation ramp waveform. This is true. The solution can be realized by the use of a sample-and-hold circuit in conjunction with a normal pwm scheme. More detail on this may be found in [9] and the practical example of the next chapter where two high ripple waveforms are returned to the modulator. In the following chapter the interesting case of the finite-settling-time response will be taken up in general and a second-order example constructed as a demonstrator.

7.5 Review

This chapter developed a discrete model for switching converters and regulators of general applicability, from the basis of a concatenation

of exponential solutions for each switched interval, which was rendered manageable through use of a straight line approximation to the exponential matrix. Subsequent perturbation and linearization produced a dynamic model in the discrete domain that is the dual to the state-space-averaged model in the continuous time domain. With the aid of the z-transform, the discrete model was used to ascertain stability bounds on the gain coefficients for a state-vector-feedback buck regulator whose error return vector is determined optimally in the continuous domain.

Kinship of the linearized-discrete and state-space-averaged models was established on three levels. First, it was demonstrated that the time-domain differential and difference equations are related by the switching period. Second, correspondingly simple differences between the matrices of the models were shown to exist. Third, a simple transformation was given relating the two models' predictions in its respective z or s frequency domain.

Finally, important observations were made on the subject of inductive current feedback control, by very simple time-domain methods. Results include: establishment of an expression for controlled inductive current bandwidth of wide applicability in switched-mode converter topologies, determination of stability bounds for current control gain, and an introduction to the concept of finite-settling-time error response. The utility of these findings is enhanced by their elementary form and derivation.

Further growth and substantiation of these ideas are supplied in the next chapter.

CHAPTER 8

FINITE SETTLING TIME

The discussion on current feedback control in the preceding chapter introduced the notion of an error decay which completely transpires in a fixed number of switching intervals, independent of the initial error. This finite-settling-time response was shown to exist in the simplest circumstance where one state was considered and its natural dynamics were ignored relative to the control induced changes. The single-cycle elimination of current error was envisioned using a straight-line geometric construction of typical inductive current waveforms, which resulted in a constant-gain feedback control law producing the fastest possible transient response. Stimulated by the success obtained in the simple case, one is naturally led to consider prospects for obtaining the time-optimal response for more widely applicable switching system models, which include natural dynamics and an arbitrary number of states. To obtain a less restricted result, the straight-line geometric interpretation is discarded and the dynamic model of the previous chapter is used in its place. Success may well be anticipated in such an undertaking, particularly if one recalls that the dynamic model is based on a more general straight line, that approximates the exponential matrix solution to the system differential equations.

To develop a full understanding of the finite-settling-time control process, three different points of view will be used for exposition in this chapter. First, the problem will be inspected from a control-coordinate frame of reference that is particularly useful in revealing

the mechanics of the error reduction and establishing the existence of a constant feedback gain vector which effects the desired response. Second, the system's eigenvector coordinates will be used along with the specific case of a second-order plant to show the solution in a lucid circumstance where the mathematics are relatively simple. Third, the general answer for the feedback gain vector is generated in an arbitrary coordinate system for any specified length of the state vector. This problem attack may be used in the coordinates of the designer's choice, typically the result of a physically meaningful and measureable state definition, which ultimately will be used for feedback implementation. The general approach not only derives the feedback gains, but also considers optimal use of feedforward to further increase immunity to sensed external disturbances. To emphasize the utility of the universal solution, the regulator gains producing the fastest possible transient decay for a buck converter are derived in closed form.

To substantiate the derivations for the control gains, a specific converter with second-order dynamics is analyzed in both eigenvector and generalized coordinates, and the coincident result is realized in hardware for laboratory verification. The regulator performance is subjected to time and frequency domain measurements which support the analysis and lend credence to the discrete dynamic model.

8.1 Control coordinate analysis

The existence of the finite-settling-time response for switching converters, with appropriate constant state-vector feedback control, is most easily established through use of the artifice of a control-coordinate

reference frame. In such a reference one may view the error reduction as a methodical elimination of independent dimensions of the perturbation, mapping it into the origin with a sequence of control exercise whose length equals the system order. The analysis of this section is an adaptation of that presented in [22] to the particular instance of switching converters. Although most of the development will concern itself with a second-order example for clarity, the important results will be expanded to embrace higher order systems.

In the previous chapter eqn. (7.35) provided an abbreviated statement of the linearized discrete ac dynamic model that will be used as the basis for the endeavor of these first two sections, and so is duplicated here for expediency:

$$\hat{x}(T_s) = F\hat{x}(0) + h\hat{d}(0) \tag{7.35}$$

Recall that F is the linearized state transition matrix, and h is the control influence vector, respectively relating the effects of initial conditions and duty-ratio modulation on the characteristics of the state disturbance at the end of one cycle. Specific definitions of F and h are given by eqns. (7.15) and (7.16) where they are shown to depend on the matrices of the state-space subinterval descriptions, the steady-state operating condition, and the switching period T_s.

As a step toward understanding the general case, it behooves one to solve for the states, if any, from which the origin may always be reached with a single exercise of control. With $\hat{x}^1(0)$ indicating such a state (7.35) is rewritten:

$$\hat{x}(T_s) = 0 = F\hat{x}^1(0) + h\hat{d}(0) \tag{8.1}$$

whence the solution for $\hat{x}^1(0)$ is

$$\hat{x}^1(0) = -F^{-1}h\hat{d}(0) \tag{8.2}$$

If an appropriate vector in the direction of $\hat{x}^1(0)$ is defined as a basis vector for a new choice of coordinates, to be called control coordinates for reasons which will become evident, then (8.2) may be rewritten as

$$\hat{x}^1(0) = q_1 v_1 \tag{8.3}$$

where q_1 is some real constant related to the magnitude of $\hat{x}^1(0)$. The basis vector v_1 is not necessarily a unit vector as it is defined by

$$v_1 = F^{-1}h \tag{8.4}$$

As a logical sequel to (8.3) let us now seek out a solution for all states $\hat{x}^2(0)$ from which the origin may be reached with at most two sequential alterations of duty ratio. It is plain that the states $\hat{x}^2(0)$ must be those removed from $\hat{x}^1(0)$ by a single period of duty-ratio control. Thus use of (7.35) and (8.3) permits writing a relationship containing $\hat{x}^2(0)$ as

$$\hat{x}(T_s) = q_1 v_1 = F\hat{x}^2(0) + h\hat{d}(0) \tag{8.5}$$

Resolution of an expression for $\hat{x}^2(0)$ from (8.5) yields

$$\hat{x}^2(0) = F^{-1}[q_1 v_1 - h\hat{d}(0)] \tag{8.6}$$

or equivalently by use of (8.4), which defines v_1,

$$\hat{x}^2(0) = q_1 F^{-2}h - F^{-1}h\hat{d}(0) \tag{8.7}$$

Parallel to the procedure for expressing $\hat{x}^1(0)$, define a second basis vector as

$$v_2 = F^{-2}h \tag{8.8}$$

then (8.7) may take the form

$$\hat{x}^2(0) = q_1 v_1 + q_2 v_2 \tag{8.9}$$

where q_1 and q_2 are some newly defined real constants. In (8.9) it is manifest that if v_1 and v_2 are linearly independent vectors and the state vector $\hat{x}$ is of length two, then $\hat{x}^2(0)$ may assume any value in the two-dimensional space by proper assignment of q_1 and q_2. As such, it is apparent from (8.9) that as long as v_1 and v_2 span the state space, the state may occupy the origin in at most two cycles, irrespective of the starting point. It remains to be demonstrated that this feat may be accomplished by means of constant gain feedback.

Proceeding with examination of the second-order case, one may utilize (8.9) and (7.35) to write

$$\hat{x}(T_s) = F[q_1(0)v_1 + q_2(0)v_2] + h\hat{d}(0) \tag{8.10}$$

Use of (8.4) and (8.8), which define v_1 and v_2, allows reformatting of (8.10) as

$$\hat{x}(T_s) = F[q_1(0)F^{-1}h + q_2(0)F^{-2}h] + h\hat{d}(0) \tag{8.11}$$

which in turn reduces to

$$\hat{x}(T_s) = q_2(0)v_1 + [q_1(0) + \hat{d}(0)]h \tag{8.12}$$

Since the time-optimal control is sought, it is desired that (8.12) be of the form of (8.5), or equivalently that $\hat{x}(T_s)$ lies in the direction of v_1, which occurs if and only if

$$\hat{d}(0) = - q_1(0) \tag{8.13}$$

in which case $q_1(T_s)$ is specified by

$$q_1(T_s) = q_2(0) \tag{8.14}$$

and so,

$$\hat{x}(T_s) = q_1(T_s)v_1 \tag{8.15}$$

which is in the required form. In like fashion to the solution for (8.13) it may be stipulated that

$$\hat{x}(2T_s) = 0 = q_1(T_s)Fv_1 + h\hat{d}(T_s) \tag{8.16}$$

When (8.16) is reduced through use of (8.4), which defines v_1, it becomes

$$0 = (q_1(T_s) + \hat{d}(T_s))h \tag{8.17}$$

In (8.17) it is obvious that $\hat{d}(T_s)$ must be constrained by

$$\hat{d}(T_s) = - q_1(T_s) \tag{8.18}$$

Inspection of (8.13) and (8.18) reveals that the control for second-cycle settling of the two-state system is always determined by the magnitude of the first element of the error vector expressed in control coordinates. It follows that the solution for q_1, and hence the control $\hat{d}$, is given by an invariant linear combination of the vector-element scalar magnitudes expressed in any specified spanning coordinate system, as may be realized by the following argument. Since the control coordinates and the other bases of choice both span the state space, any $\hat{x}$ may be equivalently described in either reference. Thus we have

$$\hat{x} = p_1x_1 + p_2x_2 = q_1v_1 + q_2v_2 \tag{8.19}$$

which, when cast as vector dot products, becomes

$$\hat{x} = \begin{bmatrix} p_1 & p_2 \end{bmatrix} \begin{bmatrix} x_1 \\ x_2 \end{bmatrix} = \begin{bmatrix} q_1 & q_2 \end{bmatrix} \begin{bmatrix} v_1 \\ v_2 \end{bmatrix} \tag{8.20}$$

The v_i and the x_i have unchanging magnitude and direction in state space, so they are related by an invariant transform matrix which may be illustrated as

$$\begin{bmatrix} x_1 \\ x_2 \end{bmatrix} = \begin{bmatrix} t_{11} & t_{12} \\ t_{21} & t_{22} \end{bmatrix} \quad \begin{bmatrix} v_1 \\ v_2 \end{bmatrix} \tag{8.21}$$

Substitution of (8.21) in (8.20) generates

$$\hat{x} = [p_1 \; p_2] \begin{bmatrix} t_{11} & t_{12} \\ t_{21} & t_{22} \end{bmatrix} \begin{bmatrix} v_1 \\ v_2 \end{bmatrix} = [q_1 \; q_2] \begin{bmatrix} v_1 \\ v_2 \end{bmatrix} \tag{8.22}$$

where it is easy to see that

$$q_1 = t_{11}p_1 + t_{21}p_2 \tag{8.23}$$

and so, the solution for the control exercise is a uniform combination of the error components measured in any chosen complete basis frame.

Now established, for a second-order system, are the important results that, subject to certain constraints on the control coordinates, any state may be mapped into the origin in at most two periods, and that the transformation may be done with constant coefficient feedback from any suitable state definition. Accompanying these significant findings is the descriptive interpretation of the regular reduction of control coordinate dimensions of error, until the error is confined to a space of zero dimension at the origin.

The treatment of the second-order dynamics can be directly extrapolated to include more complicated converters with higher-order state descriptions. It is then found that the n^{th} order system can settle in at most n cycles when governed by the control law

$$\hat{d}(iT_s) = - q_1(iT_s) \tag{8.24}$$

and that q_1 may always be determined from a specific constant linear combination of error components measured in spanning coordinates. As a matter of additional interest, it is also true generally that

$$q_1(iT_s) = q_{1+i}(0) \tag{8.25}$$

and so the entire control sequence is predetermined by the initial values of the error, even though in practice it will be generated by linear feedback and the propagation of the dwindling perturbation.

The condition that the control coordinates span the state space is a criterion for the controllability of the converter. In practice this test is almost invariably satisfied, although it may prove difficult to demonstrate. The solution in Section 8.3, developed in generalized coordinates, gives an equivalent means of determining controllability that is easily applied.

Even though the solution for the optimal feedback gains can be developed along the lines of this section, a less complicated answer in terms of the familiar concepts of eigenvectors and eigenvalues may be obtained. The next section makes use of coordinates which decouple the states of a second-order system for a simplified exposition.

8.2 Eigenvector coordinate analysis

The finite-settling-time control gains will be generated for the second-order switching converter by use of the converter canonic coordinates and adoption of a method recommended in [23]. Resort to eigenvector coordinates permits one to view the action of each state as

independent of the others which results in considerable simplification of the notation in the solution. The procedure established here, with explicit expanded expressions for the second-order system, is similar to and will lay the foundations for the more general treatment of the next section where the notation of necessity is more complex.

If the matrix F in (7.35) has distinct eigenvalues, which will be assumed for this development, then there exists a matrix L which satisfies the generalized eigenproblem

$$FL = L\Lambda \tag{8.26}$$

In (8.26), Λ is a diagonal matrix of the eigenvalues of F, and L is a matrix whose columns are the eigenvectors of F. Since the eigenvalues are distinct, the eigenvectors are linearly independent and L is non-singular. Therefore (8.26) may be solved for Λ which yields

$$\Lambda = L^{-1}FL \tag{8.27}$$

It is desired to make use of (8.27) to render dynamic eqn. (7.35) diagonal. To this end, premultiply (7.35) by L^{-1} as in

$$L^{-1}\hat{x}(T_s) = L^{-1}F\hat{x}(0) + L^{-1}h\hat{d}(0) \tag{8.28}$$

If $\hat{x}(0)$ is replaced by $LL^{-1}\hat{x}(0)$ in (8.28), then (8.29) results, which has the diagonal form:

$$L^{-1}\hat{x}(T_s) = L^{-1}FLL^{-1}\hat{x}(0) + L^{-1}h\hat{d}(0) \tag{8.29}$$

To see this define w by

$$w = L^{-1}\hat{x} \tag{8.30}$$

and f by

$$f = L^{-1}h \tag{8.31}$$

then, with use of (8.27), (8.29) becomes

$$w(T_s) = \Lambda w(0) + f\hat{d}(0) \tag{8.32}$$

If (8.32) is used twice, an expression for $w(2T_s)$ may be written in terms of $w(0)$:

$$w(2T_s) = \Lambda^2 w(0) + \Lambda f\hat{d}(0) + f\hat{d}(T_s) \tag{8.33}$$

In the preceding section it was shown that we may expect to be able to reduce $w(0)$ to zero in two cycles and so, with this in mind, we may set $w(2T_s) = 0$ in (8.33). Then it consists of two simultaneous equations, in terms of the initial conditions on w, for the two unknowns $\hat{d}(0)$ and $\hat{d}(T_s)$. Expanding the notation in (8.33) with $w(2T_s) = 0$ yields

$$0 = \begin{bmatrix} \lambda_1^2 & 0 \\ 0 & \lambda_2^2 \end{bmatrix} \begin{bmatrix} w_1(0) \\ w_2(0) \end{bmatrix} + \begin{bmatrix} \lambda_1 & 0 \\ 0 & \lambda_2 \end{bmatrix} \begin{bmatrix} f_1 \\ f_2 \end{bmatrix} \hat{d}(0) + \begin{bmatrix} f_1 \\ f_2 \end{bmatrix} \hat{d}(T_s) \tag{8.34}$$

which when written in scalar equation form becomes

$$\begin{aligned} 0 &= \lambda_1^2 w_1(0) + \lambda_1 f_1 \hat{d}(0) + f_1 \hat{d}(T_s) \\ 0 &= \lambda_2^2 w_2(0) + \lambda_2 f_2 \hat{d}(0) + f_2 \hat{d}(T_s) \end{aligned} \tag{8.35}$$

Equations (8.35) make it very plain to see that the matrix-vector eqn. (8.33) was indeed simultaneous equations for the $\hat{d}$ in terms of $w(0)$. Any of the several techniques for solving simultaneous linear equations may produce answers for the $\hat{d}$. However, from the results of the previous section, we know that $\hat{d}$ will be an invariant linear combination of w, and so we need only solve for $\hat{d}(0)$ to find the feedback gain coefficients.

As such, in this instance, Cramer's rule provides an attractive solution. Slight manipulation of (8.35) reformats the equations as

$$\begin{aligned} -w_1(0) &= f_1/\lambda_1\ \hat{d}(0) + f_1/\lambda_1^{\,2}\ \hat{d}(T_s) \\ -w_2(0) &= f_2/\lambda_2\ \hat{d}(0) + f_2/\lambda_2^{\,2}\ \hat{d}(T_s) \end{aligned} \tag{8.36}$$

and so, the answer in determinant form for $\hat{d}(0)$ is

$$\hat{d}(0) = \frac{\begin{vmatrix} -w_1(0) & f_1/\lambda_1^{\,2} \\ -w_2(0) & f_2/\lambda_2^{\,2} \end{vmatrix}}{\begin{vmatrix} f_1/\lambda_1 & f_1/\lambda_1^{\,2} \\ f_2/\lambda_2 & f_2/\lambda_2^{\,2} \end{vmatrix}} \tag{8.37}$$

Performing the operations indicated in (8.37) and simplifying the result yields eqn. (8.38) which is the time-optimal control law for a second-order plant expressed in canonical coordinates:

$$\hat{d}(0) = w_1(0)\ \frac{-\lambda_1^{\,2}}{f_1(\lambda_1-\lambda_2)} + w_2(0)\ \frac{\lambda_2^{\,2}}{f_2(\lambda_1-\lambda_2)} \tag{8.38}$$

Note how the solution assumes a simple form in terms of the familiar eigenvalues, and also that similar eigenvalues will result in large feedback gains. Thus, <u>good design practice is to configure the open-loop plant such that it has distinct eigenvalues</u>, in accordance with the assumptions of this development. Rarely, however, will (8.38) be of any use by itself. The canonical state may be a complex number combination of the initial choice of state $\hat{x}$, and so to use the information in (8.38) we need to

transform it back to a meaningful choice of state vector elements. Let k_1' and k_2' be the canonical state feedback gains defined by

$$k_1' = \frac{\lambda_1^2}{f_1(\lambda_1-\lambda_2)} \quad , \quad k_2' = \frac{-\lambda_2^2}{f_2(\lambda_1-\lambda_2)} \tag{8.39}$$

then (8.38) may be cast in vector notation as

$$\hat{d}(0) = -k'^T w(0) \tag{8.40}$$

If definition (8.30), for w in terms of x, is used in (8.40), (8.41) results:

$$\hat{d}(0) = -k'^T L^{-1}\hat{x}(0) \tag{8.41}$$

In (8.41) it may be seen that the desired feedback gain vector K is given by

$$K^T = k'^T L^{-1} \tag{8.42}$$

which is a useful answer, once the mechanics of obtaining the eigenvalues defining k' and the eigenvectors comprising L are sorted out.

The eigenvalues of any second order matrix are handily evaluated as

$$\lambda_{1,2} = \frac{Tr}{2} \pm \sqrt{\left(\frac{Tr}{2}\right)^2 - Det} \tag{8.43}$$

where Tr implies the trace, or sum of the matrix diagonals, and Det implies the matrix determinant. Thus in our particular case, with regard to the matrix F, we have

$$Tr = f_{11} + f_{22} \tag{8.44}$$

and

$$Det = f_{11}f_{22} - f_{12}f_{21} \tag{8.45}$$

With suitable normalization, the eigenvector matrix L takes the form

$$L = \begin{bmatrix} 1 & 1 \\ \ell_{21} & \ell_{22} \end{bmatrix} \tag{8.46}$$

where the elements ℓ_{21} and ℓ_{22} may be calculated from the eigenvalues and the components of F by use of (8.47):

$$\begin{aligned} \ell_{21} &= -\left(\frac{f_{11} - \lambda_1}{f_{12}}\right) \\ \ell_{22} &= -\left(\frac{f_{11} - \lambda_2}{f_{12}}\right) \end{aligned} \tag{8.47}$$

Notice that F must be written such that $f_{12} \neq 0$ for eqns. (8.47) to be used. To write the expression for the feedback gains, L^{-1} is needed, and so (8.48) provides the required information from inversion of (8.46):

$$L^{-1} = \frac{\begin{bmatrix} \ell_{22} & -1 \\ -\ell_{21} & 1 \end{bmatrix}}{\ell_{22} - \ell_{21}} \tag{8.48}$$

Now a complete algorithm for solution of the time-optimal feedback gain vector is established. One need only write the dynamic eqn. (7.35) by any of the methods of Chapter 7, calculate the eigenvalues of F from (8.43), find f from (8.31), obtain k' from (8.39), derive L^{-1} using (8.47) and (8.48), then write the answer from (8.42). This procedure would not be too arduous an undertaking with a hand calculator if all of the arithmetic were real. Unfortunately, by the very nature of the high efficiency conversion sought, the eigenvalues of F will often be complex,

and so will the arithmetic involved in this approach. Aside from this complication, however, the method is straightforward and rather generally applicable to second order systems. Since a modern digital computer manipulates complex numbers with great facility, there is little difficulty in automating the aforementioned algorithm to solve for the gains directly from the statement of (7.35). This has been done and a copy of the Fortran coding is provided in the Appendix.

In Section 4 of this chapter results obtained for a particular second-order system by means of this algorithm, and an algorithm to be developed in the next section, are given. The gains obtained by the method of this section are scaled by a loop-gain factor, and a root locus plot is generated which confirms the eigenvector coordinate analysis. When the loop-gain scale factor is unity the z-domain poles are shown to reside at the origin as anticipated.

It may be seen that the solution for the return coefficients relies on a time-domain analysis. The prediction of the diagonalized dynamic eqn. (8.32) was used twice in succession to obtain a relationship for $w(2T_s)$ in terms of initial conditions and two exercises of control. Two equations, from the state vector of length two, and two unknowns $\hat{d}$, from considering two transition periods, resulted in a unique determination for the control gains, when $w(2T_s)$ is set equal to zero. It will be shown in the next section that this type of time-domain problem formulation and solution may be used on higher-order systems, with correspondingly longer control sequences, and that it may be done in any spanning coordinate system.

8.3 Generalized coordinate analysis

This final assault on the finite-settling-time control problem will be the most general, and at the same time in some ways the simplest. Since a solution with as few restrictions on it as possible is desired, no longer will the abbreviated form of the dynamic equation be used. The starting point will be eqn. (7.17) which includes modelling of control disturbances other than the duty-ratio modulation. Since it is essential to the present development, eqn. (7.17) is given again here:

$$\hat{x}(T_s) = F\hat{x}(0) + B\hat{u}(0) + h\hat{d}(0) \tag{7.17}$$

The control vector disturbance $\hat{u}(0)$ may include such influences on the switching system as input voltage and load variation. Under the present modelling technique, these perturbations are assumed to be constant during any given switching period, so $\hat{u}(0)$ describes $\hat{u}$ from the beginning of the period until just prior to the next sampling instant.

In the eigenvector coordinate development, the solution was obtained by writing an expression for $w(2T_s)$ and setting that quantity to zero. For the present purpose a relation for $\hat{x}(iT_s)$ will be required. Repeated application of (7.17) generates the requisite equation:

$$\hat{x}(iT_s) = F^i\hat{x}(0) + \sum_{j=0}^{i-1} F^{i-1-j}[B\hat{u}(jT_s) + h\hat{d}(jT_s)] \tag{8.49}$$

Equation (8.49) gives us foresight into the position of the ac state vector as a function of its initial position in state space and the control sequences $\hat{d}(jT_s)$ and $\hat{u}(jT_s)$. The duty-ratio modulation $\hat{d}(jT_s)$ is effected

at the discretion of the design engineer, usually by linear feedback. The other control perturbations $\hat{u}(jT_s)$ typically are not known in advance, and only $\hat{u}(0)$ can be measured. An unbiased assumption about $\hat{u}$ would be that

$$\hat{u}(jT_s) = 0 \quad , \quad j \neq 0 \tag{8.50}$$

Application of (8.50) to (8.49) yields

$$\hat{x}(iT_s) = F^i\hat{x}(0) + F^{i-1}B\hat{u}(0) + \sum_{j=0}^{i-1} F^{i-1-j}h\hat{d}(jT_s) \tag{8.51}$$

The intent is to use eqn. (8.51) to solve for the $\hat{d}(jT_s)$ that will reduce $\hat{x}(0)$ to zero while negating the impact of the control disturbance $\hat{u}(0)$. To do this we may set $\hat{x}(iT_s)$ equal to zero; then, (8.51) will consist of n (the system order) simultaneous linear algebraic equations in the i unknowns $d(jT_s)$. For these equations to possess a unique solution for the $\hat{d}(jT_s)$, with $\hat{x}(0)$ and $\hat{u}(0)$ arbitrarily determined, one must choose i = n. This observation is in keeping with the results of Section 8.1 where it was shown that the n^{th} order plant required n cycles to settle. With i = n and $\hat{x}(nT_s) = 0$ (8.51) becomes (8.52):

$$0 = F^n\hat{x}(0) + F^{n-1}B\hat{u}(0) + \sum_{j=0}^{n-1} F^{n-1-j}h\hat{d}(jT_s) \tag{8.52}$$

The sequence $\hat{d}(jT_s)$ may be viewed as a vector $\underline{\hat{d}}$ of length n whose elements are $\hat{d}_j = \hat{d}(jT_s)$. Then, to simplify notation, some matrices may be defined as

$$P = F^n \tag{8.53}$$

$$Q = F^{n-1}B$$

and

$$C = \underset{j=0}{\overset{n-1}{\text{Col}}} F^{n-1-j}h \tag{8.54}$$

where in (8.54) Col denotes the left-to-right column expansion of the arguments following it to generate a matrix. With these definitions and the vector concept of $\hat{d}$, (8.52) may be expressed compactly as

$$0 = P\hat{x}(0) + Q\hat{u}(0) + C\underline{\hat{d}} \tag{8.55}$$

Since (8.55) is a set of simultaneous equations and only one of the unknowns need be solved for, we may again write the solution for $\hat{d}(0)$, in determinant form, through use of Cramer's rule as

$$\hat{d}(0) = \frac{\left|[-P\hat{x}(0) - Q\hat{u}(0)] + \underset{j=1}{\overset{n-1}{\text{Col}}} F^{n-1-j}h\right|}{|C|} \tag{8.56}$$

However, the arithmetic of the more general solution is often best handled by a digital computer, and (8.56) proves to be a computationally expensive way to solve (8.55). An alternative method is provided by inversion of C and use of

$$\underline{\hat{d}} = -C^{-1}P\hat{x}(0) - C^{-1}Q\hat{u}(0) \tag{8.57}$$

In (8.57) it may be seen that the complete solution for the entire control sequence is determined by the initial condition, again agreeing with the analysis of Section 8.1. For solutions (8.56) and (8.57) to exist, it is required that $|C| \neq 0$. This is an alternative statement of the need for control coordinates to span the state space. The matrix C, often referred to as the controllability matrix, must be nonsingular, or else there are

one or more dimensions in state space that are not independently affected by any control sequence. Such a circumstance is rare for switching converters, which by design are controllable systems.

The solutions (8.56) and (8.57) may in some situations be even easier to evaluate than the eigenvector coordinate answer. If $\hat{x}$ is chosen to be a real vector variable, then the tedium of complex arthmetic may be avoided. Further, (8.57) need not be evaluated in its entirety, since the feedback gain vector is prescribed by the first row of $C^{-1}P$. In simple cases closed form results are readily obtained, as will now be shown by returning to the buck converter example.

To keep the example as simple as possible, $\hat{u}(0)$ will be taken to be zero and so all the system description needed is provided by eqns. (7.23) for F and (7.24) for h. From those equations the controllability matrix may be formed as shown in (8.58):

$$C = \begin{bmatrix} Fh & h \end{bmatrix} = \begin{bmatrix} \frac{V_g T_s}{L} & \frac{V_g T_s}{L} \\ \frac{V_g T_s^2}{LC} & 0 \end{bmatrix} \tag{8.58}$$

The inverse of C may be evaluated in the usual manner as

$$C^{-1} = \begin{bmatrix} 0 & \frac{LC}{V_g T_s^2} \\ \frac{L}{V_g T_s} & -\frac{LC}{V_g T_s^2} \end{bmatrix} \tag{8.59}$$

If F, as given in (7.23), is squared then P results:

$$P = \begin{bmatrix} \left(1 - \frac{T_s^2}{LC}\right) & \left(-\frac{T_s}{L}\left[2 - \frac{T_s}{RC}\right]\right) \\ \left(\frac{T_s}{C}\left[2 - \frac{T_s}{RC}\right]\right) & \left(-\frac{T_s^2}{LC} + \left[1 - \frac{T_s}{RC}\right]^2\right) \end{bmatrix} \tag{8.60}$$

The feedback gain vector K^T is now obtained, as given in (8.61), by pre-multiplying P in (8.60) with the first row of C^{-1} in (8.59).

$$K^T = \left[\left(\frac{L}{V_g T_s}\left[2 - \frac{T_s}{RC}\right]\right), \left(-\frac{1}{V_g} + \frac{LC}{V_g T_s^2}\left[1 - \frac{T_s}{RC}\right]^2\right)\right] \tag{8.61}$$

The result may be directly verified by solving for the closed-loop z-domain poles, which may be obtained, as in the example of Section 7.2, by solving for the singularities of zI-M appearing in eqn. (7.27). After appropriate substitutions in (7.27) for the elements of K from (8.61), and a little manipulation, we have zI-M given in (8.62):

$$zI\text{-}M = \begin{bmatrix} \left(z + \left[1 - \frac{T_s}{RC}\right]\right)\left(\frac{C}{T_s}\left[1 - \frac{T_s}{RC}\right]^2\right) \\ \left(-\frac{T_s}{C}\right) \qquad \left(z - \left[1 - \frac{T_s}{RC}\right]\right) \end{bmatrix} \tag{8.62}$$

To find the singularities, set the determinant of zI-M to zero, which results in

$$z^2 - \left(1 - \frac{T_s}{RC}\right)^2 + \left(1 - \frac{T_s}{RC}\right)^2 = 0 \tag{8.63}$$

or

$$z^2 = 0 \tag{8.64}$$

and so, both z-domain poles are assigned to the origin when K^T is

determined by (8.61). The z-domain pole placement is indicative of a finite-settling-time response, which confirms the anticipations. Thus we see, in this simple example, that it is possible to obtain a closed-form result, which is always desirable from a design point of view. One may observe from (8.61) that the gains are independent of operating point, vary inversely with the source voltage, and have specific dependence on the switching period and circuit elements. Therefore, for instance, if inordinately large gains resulted from a particular proposed converter configuration, the designer can see what must be done to correct the situation. If he cannot change circuit parameters, he may opt for a slower transient response by reducing each gain to a fraction of the finite-settling-time value. Then the modified response could be predicted from a z-domain root locus, obtained by use of (8.61), to determine the ratio of the two gains, and (7.27), from which the poles may be repeatedly obtained to form a locus.

Although closed-form results are nice from a design standpoint, they are seldom procured this easily. With sacrifice of the insight of analytic expressions, the large portion of the tedious arithmetic may be assigned to a digital computer. Software for the solution outlined in this section is included in the Appendix. The Fortran program presented there will solve for the finite-settling-time feedback and feedforward gains, from the starting point of the state matrices, for systems up to tenth order. Intermediate results are printed out to give the designer as much insight into the idiosyncrasies of each solution as possible. The design example of the next section contains some output from this computer program analysis.

8.4 Second-order finite-settling-time control example

The applications of the discrete approach thus far have been rather simple ones, so that the mathematics remained manageable and the method was prominent. This section will substantiate earlier results by presenting an actual design instance and hardware realization of finite-settling-time control. The candidate chosen to illustrate the effectiveness of discretized state vector feedback is a coupled-inductor Ćuk converter. Owing to the converter's nonlinear gain characteristic, the feedback and feedforward gains are operating condition dependent, and so the closed-form solution is considerably more complicated than in the buck converter example. To circumvent algebraic toil, the computer programs based on the methods of Sections 8.2 and 8.3 are utilized.

Consider the coupled-inductor Ćuk converter shown in Fig. 8.1. The converter contains two energy storage elements, L and C, and thus is a system governed by second-order dynamics. The switch shown alternately grounds one end or the other of C with fixed period T_s and duty ratio D. A physically meaningful and easily measurable state variable selection is the inductor magnetizing current and the capacitor voltage. To distinctly identify this choice of states, Fig. 8.1 may be redrawn with the coupled inductor replaced by the equivalent circuit model of an ideal transformer. Fig. 8.2 shows the converter model with the state variables identified and their sense indicated. By inspection of Fig. 8.2, it is possible to write the vector differential equation describing the system dynamics for each position of the switch. Using the principle of linear superposition, one may evaluate the effect of each state or control with all others assumed

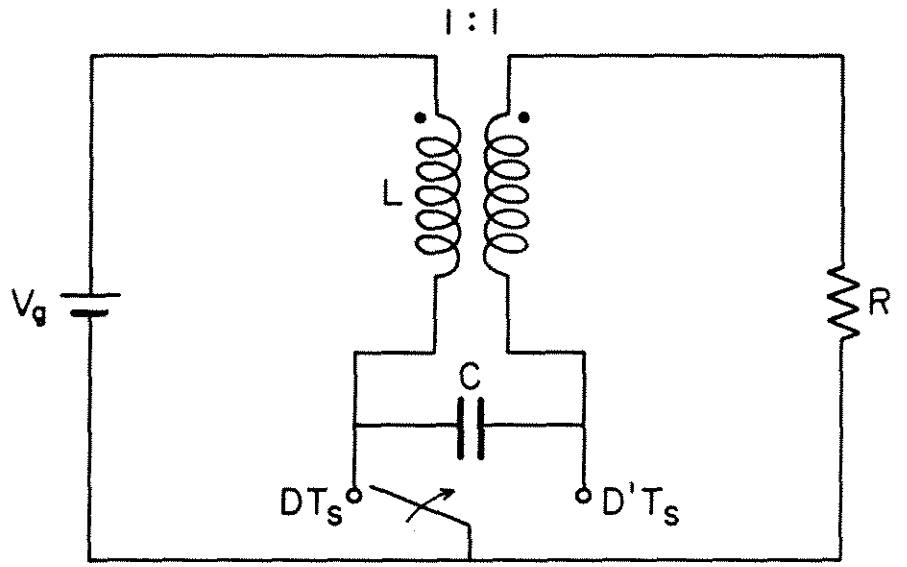

Fig. 8.1 The coupled-inductor Ćuk converter without output capacitor used to demonstrate a two-cycle total transient time recovery from error.

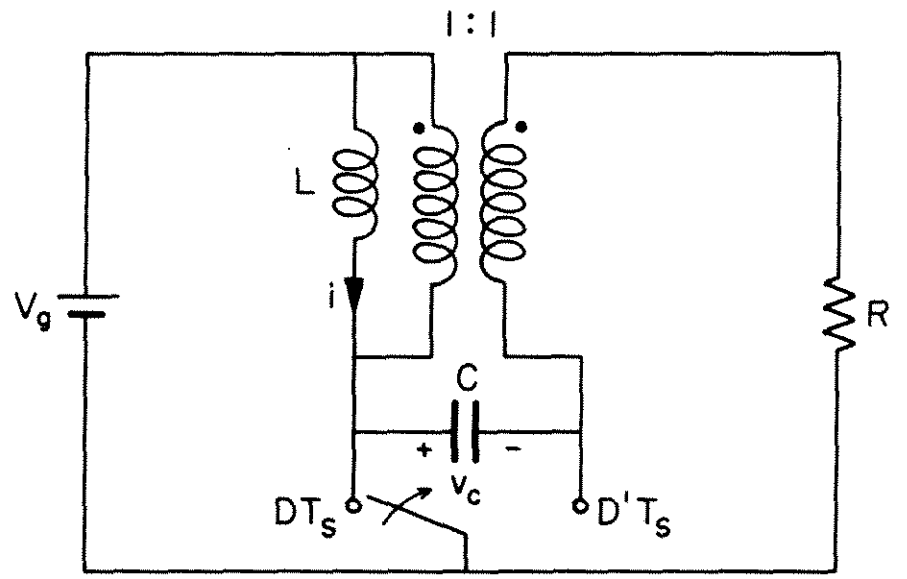

Fig. 8.2 State-variable model for the finite-settling-time demonstrator.

zero. When all states and controls have been independently considered, and their contributions to the state derivative superimposed, the complete description of the state dynamics is obtained. One need only write the anticipated form of the vector differential equation and then enter the matrix elements one at a time by examination of the circuit model in Fig. 8.2. Equations (8.65) and (8.66) give the outcome for the two switched intervals DT_s and $D'T_s$:

$$\frac{d}{dt}\begin{bmatrix} i \\ v_c \end{bmatrix} = \begin{bmatrix} 0 & 0 \\ 0 & -\frac{1}{RC} \end{bmatrix}\begin{bmatrix} i \\ v_c \end{bmatrix} + \begin{bmatrix} \frac{1}{L} \\ \frac{1}{RC} \end{bmatrix} V_g \quad ; \quad \underline{DT_s} \tag{8.65}$$

$$\frac{d}{dt}\begin{bmatrix} i \\ v_c \end{bmatrix} = \begin{bmatrix} 0 & -\frac{1}{L} \\ \frac{1}{C} & -\frac{1}{RC} \end{bmatrix}\begin{bmatrix} i \\ v_c \end{bmatrix} + \begin{bmatrix} \frac{1}{L} \\ \frac{1}{RC} \end{bmatrix} V_g \quad ; \quad D'T_s \tag{8.66}$$

Note that in the present formulation the control vector is the scalar input voltage V_g. More generally, one could consider more influences on the system as control. For example, load current and input voltage could comprise a control vector, then B_1 and B_2 would become 2 x 2 matrices. The solution procedure is not altered, however, and so for this illustrative example it is sufficient to consider scalar control. Load disturbances will later serve to perturb the regulator operation for examination of transient behavior.

Determination of the state equations (8.65) and (8.66) is in some

sense the answer to this control problem. Once numerical values are calculated for the matrix entries, the rest of the solution reduces to arithmetic, handled with dispatch by a computer.

The circuit of Fig. 8.1 was constructed with L = 1 mH, C = 5.36 μF, R = 150 Ω, V_g = 15 V, D = .5 and T_s = 50 μs. The converter output is - 15 V at 100 mA producing 1.5 watts of dissipation in R. With the circuit element values inserted in (8.65) and (8.66), the state equations assume the numerical form required by the computer programs as given in eqns. (8.67) and (8.68):

$$\frac{d}{dt}\begin{bmatrix} i \\ v_c \end{bmatrix} = \begin{bmatrix} 0 & 0 \\ 0 & -1244 \end{bmatrix}\begin{bmatrix} i \\ v_c \end{bmatrix} + \begin{bmatrix} 1000 \\ 1244 \end{bmatrix} 15 \quad ; \quad DT_s \qquad (8.67)$$

$$\frac{d}{dt}\begin{bmatrix} i \\ v_c \end{bmatrix} = \begin{bmatrix} 0 & -1000 \\ 1.87(10^5) & -1244 \end{bmatrix}\begin{bmatrix} i \\ v_c \end{bmatrix} + \begin{bmatrix} 1000 \\ 1244 \end{bmatrix} 15 \quad ; \quad D'T_s \qquad (8.68)$$

If the information contained in (8.67) and (8.68) is appropriately formatted and input to the computer program employing the eigenvector coordinate solution, the state transition matrix is automatically calculated by means of (7.22) as

$$F = I + AT_s = \begin{bmatrix} 1.00 & -0.0250 \\ 4.66 & 0.938 \end{bmatrix} \qquad (8.69)$$

Pursuing the solution outlined in Section 8.2, one may solve for the plant eigenvalues from F as

$$\lambda_{1,2} = 0.969 \pm 0.340i \qquad (8.70)$$

which, if transformed to polar notation, become

$$\lambda_{1,2} = 1.03 \angle \pm 19.3° \tag{8.71}$$

Conspicuous in (8.71) is the fact that discrete analysis is predicting open-loop eigenvalues that lie outside the unit circle and corresponding system instability. The circuit is known to be open-loop stable, and so we have a circumstance where the discrete formulation gives qualitatively the wrong result, even though quantitatively the error is on the order of a few percent. The discussion in Section 7.3 alluded to the possibility of such an erroneous result and sheds some light on the circumstances under which it is likely to occur. In any event, the accuracy and usefulness of the discrete model will be borne out in this example, and so one should not be too upset that neglect of small effects in obtaining linear approximations destabilized the model.

The eigenvector coordinate solution proceeds as outlined to obtain the feedback gain vector K^T given in (8.72):

$$K^T = [1.41 \quad 0.0980] \tag{8.72}$$

Since it is useful to have some idea of how critical the feedback gains are, the gain vector is multiplied by a loop gain factor k, such that K^T is replaced by kK^T, and k is varied from zero upward. The eigenvalues of the closed-loop state transition matrix M are repeatedly evaluated during this process to form a z-domain root locus as shown in Fig. 8.3. The poles follow a trajectory that takes them both to the origin when k = 1.0 as expected, and then, as k is further increased, one pole moves toward the loop-gain zero at z = 0.733 and the other proceeds to minus infinity. When k is between 1.2 and 1.4 a pole exits the unit circle along the negative real axis indicating that the circuit will go unstable with oscillations at half the switching frequency.

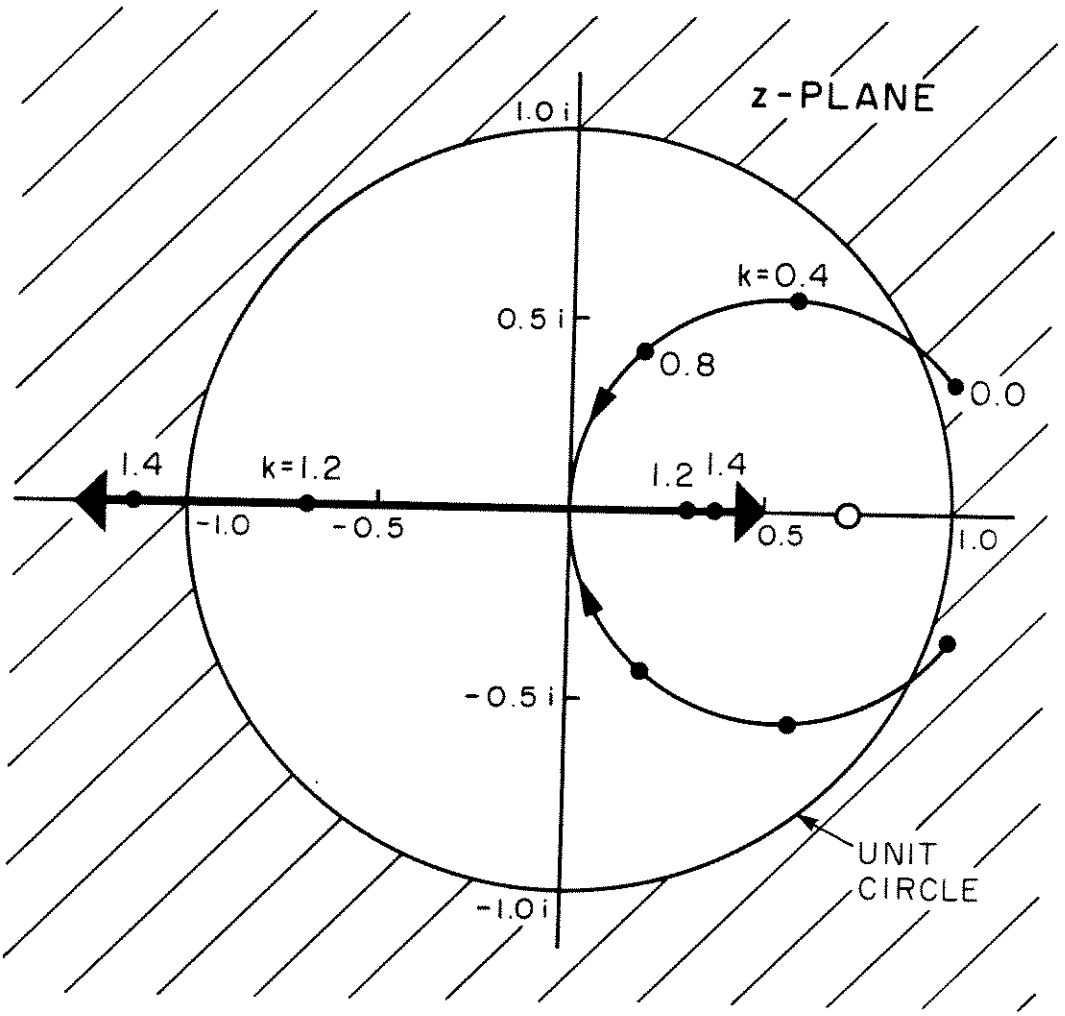

Fig. 8.3 *Z-domain root locus for the finite-settling-time configuration as a function of loop-gain normalization parameter k. Stability gain margin is between 20% and 40% determined by gains indicated on the locus exiting the unit circle at -1.*

The position of the loop gain zero was not determined by the computer program since no use is made of the loop-gain concept in the algorithm. However, the loop gain is defined in (7.33), and the location of the loop gain zero is easily calculated by hand from this definition. Once the ratio of the feedback gains is determined, so is the position of the zero. Then one may generate Fig. 8.3 by use of graphical root-locus technique just as is done in the s-plane. This is promoted as a design technique in [18] and so the zero is included in the locus to facilitate comparing solution methods. The time-domain solution solves directly for the correct ratio of the feedback gains, and in fact the precise gains, that assign the z-plane poles to the origin. In contrast, with root-locus technique, one must determine where to place the loop gain zero so that the locus passes through the origin, and then determine the required loop gain. For second-order plants this approach is workable, but clearly for higher order systems, where multiple zeroes need to be placed prior to generating a complicated locus, the method becomes cumbersome if not useless. It is still to one's advantage to be able to interpret the pole placement in terms of loop-gain and root-locus concepts. Each additional vantage point gained on the control problem increases the probability that the designer has a meaningful interpretation.

To capitalize on the attributes of the time-domain solution, another computer program was written to solve, in generalized coordinates, for feedback and feedforward finite-settling-time control gains, and to do so for systems whose state and control vectors may contain up to ten elements.

This program accepts the information of (8.67) and (8.68) directly, and automates the solution by the method of Section 8.3 thereafter. The program sets up the complete dynamic equation (7.17) through use of the defining equations (7.15) and (7.16). The process involves solving for the steady-state operating point and so this information is also printed out. The nominal state values agree precisely with the prediction of state-space averaging and are

$$x(0) = \begin{bmatrix} i(0) \\ v_c(0) \end{bmatrix} = \begin{bmatrix} 0.20 \\ 30 \end{bmatrix} \tag{8.73}$$

indicating 200 mA magnetizing current and 30 V capacitor voltage. Use of the result (8.73) in eqns. (7.15) permits calculation of the complete ac dynamic representation as

$$\hat{x}(T_s) = F\hat{x}(0) + B\hat{u}(0) + h\hat{d}(0)$$

$$= \begin{bmatrix} 1.00 & -0.025 \\ 4.66 & 0.938 \end{bmatrix} \hat{x}(0) + \begin{bmatrix} 0.050 \\ 0.062 \end{bmatrix} \hat{u}(0) + \begin{bmatrix} 1.50 \\ -1.87 \end{bmatrix} \hat{d}(0) \tag{8.74}$$

Notice that there is a negative entry in h. Upon first increasing the duty ratio the capacitor voltage will diminish, but will eventually increase due to the interaction of the states determined by F. This "wrong way" high frequency behavior manifests itself in a $1-\tau s$ term in the numerator of the Laplace transform transfer function, where it is interpreted as a right half-plane zero. The presence of this phenomenon often complicates the control loop problem by contributing to phase lag while increasing the loop gain at high frequency. The interpretation in the time domain is not nearly so elegant but one should be aware that such a minus sign in the

duty-ratio control influence vector can indicate an ill-conditioned plant and make the feedback gains unreasonably large or critical.

The solution proceeds with the calculation of P, Q, and C from (8.53) and (8.54). Then the controllability matrix is inverted and the desired gains are obtained from the first row of (8.57). The resultant control law including feedforward may be written

$$\hat{d}(0) = -[1.41 \quad 0.0980] \begin{bmatrix} \hat{i}(0) \\ \hat{v}_c(0) \end{bmatrix} - 0.0491 \quad \hat{v}_g(0) \qquad (8.75)$$

The control law (8.75) will, to the extent of the accuracy of the linearizing approximations, remove any effect of an initial state or input voltage perturbation in two switching periods.

In order to implement the control law, one must somehow obtain the values of $\hat{i}(0)$, $\hat{v}_c(0)$ and $\hat{v}_g(0)$ without heeding normal state-variable ripple or any intracycle variation in v_g. One expedient way of making the control loop conform to the postulates of the analysis is to use a sample-and-hold circuit to keep the values of the initial errors, appropriately modified by the control gains. Figure 8.4 is an equivalent circuit representation of the control loop and power stage developed for this example. The differential amplifiers and buffer amplifier are constructed from LM318 operational amplifiers. The sampling switch is a MC14066B bidirectional mosfet switch. The ramp generation and comparator functions are provided by a SG3524 switching regulator control chip. The power switch is realized by a n-channel FET and a diode. Timing signals to the sample and hold are processed with a MC14584B hex Schmitt trigger to provide

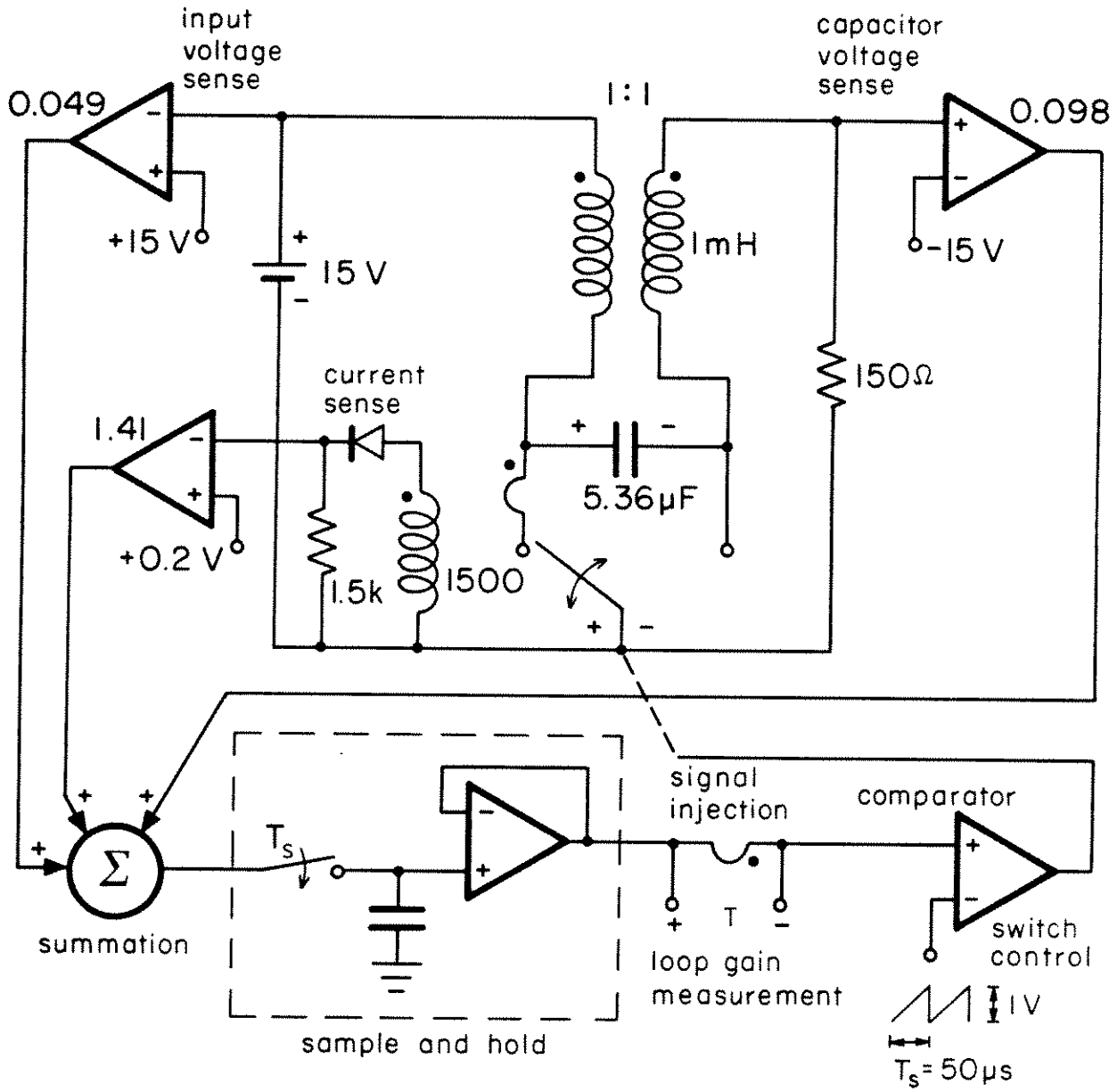

Fig. 8.4 Equivalent circuit of the finite-settling-time demonstration regulator with feedforward and feedback implementation shown as well as an appropriate point for loop-gain measurement.

sampling just after the switch grounds the positive end of the transfer capacitor.

The signal injection and loop-gain measurement points are chosen such that the injected signal is sensed by the high impedance input of the comparator, while the amplified return is measured at the low impedance output of the buffer amplifier. This technique of loop gain measurement is described in detail in [24] and [25].

We may make use of the transformation $s = (z-1)/T_s$ developed in Section 7.3 and the knowledge of the z-plane loop-gain poles and zeroes from eqn. (8.70) and Fig. 8.3 to determine the state-space-averaged frequency response prediction. The low frequency magnitude of the loop gain may be obtained from T(z) with z approaching 1, or from T(s) with s approaching zero, whichever is more convenient. The results are that the low frequency loop gain is 13 dB, the loop gain zero is at 850 Hz, and the complex pole pair is at 1080 Hz. With this information the Bode asymptotes are easily sketched. Figure 8.5 shows these asymptotes along with measurement data on loop gain and phase. One can see that the state-space-averaging prediction agrees well with the experimental data, especially considering the complexity of the loop gain path. There is a notable discrepancy in phase as 10 kHz is approached. The phase lag is heading toward 180° instead of the 90° expected from the magnitude asymptote sketch. Such deviations are commonly found as half the switching frequency is approached, and thus its occurrence here is not surprising.

The converter has no open-loop line rejection and passes any

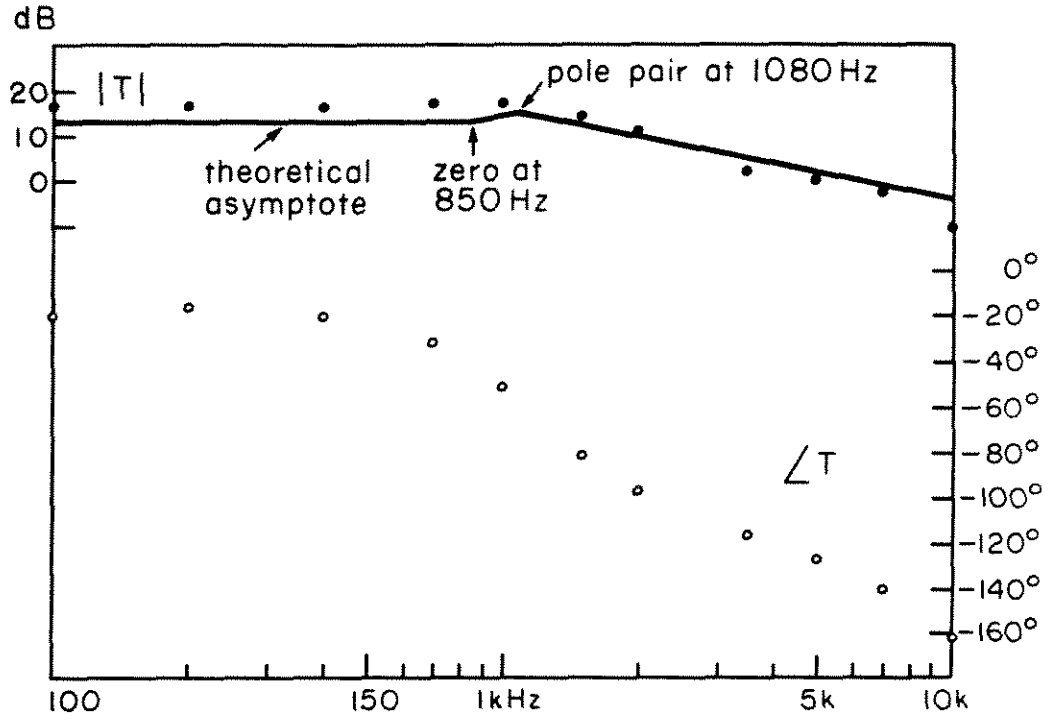

Fig. 8.5 Finite-settling-time regulator loop gain and phase.

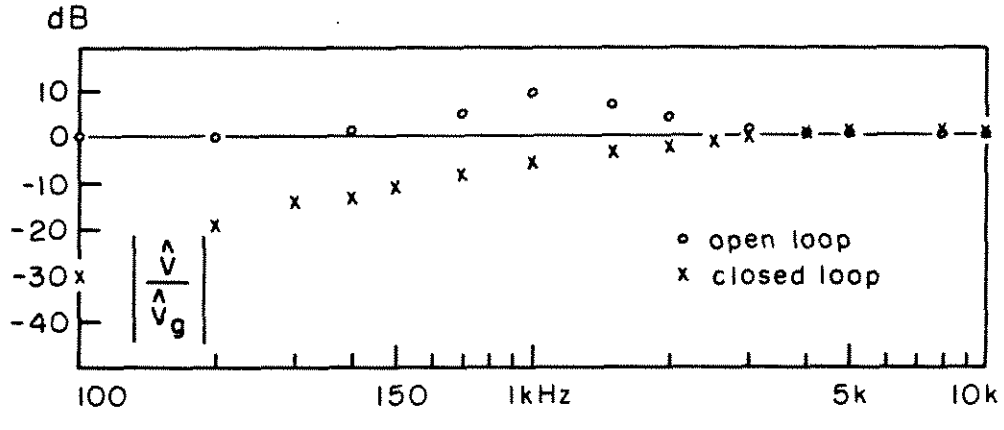

Fig. 8.6 Line rejection characteristic for the example regulator showing open and closed-loop performance.

voltage disturbance at the input directly to the output, possibly even magnified by plant resonance. Closing the loop and connecting the feedforward gain both produced improvements in the line rejection characteristic over the open-loop case, with virtually no degradation at any frequency. Figure 8.6 plots the open and closed loop data obtained experimentally. The open-loop characteristic is essentially 0 dB except in the vicinity of the system's natural resonance at 1080 Hz. Once the control is implemented, one notices appreciable line rejection below the state-space-averaged system bandwidth of $f_s/2\pi$, which may be ascertained from the transformation $s = (z-1)/T_s$ and the z-domain closed-loop pole placement. Thereafter the line rejection returns essentially to its open-loop value. Nowhere does the line rejection characteristic degrade when the feedforward is connected, and there is considerable benefit obtained at the lower frequencies. Since the line rejection feedforward gain is chosen in this case with no assumption about the frequency spectrum of the line distrubance, one may anticipate a reduction in line pass for all frequencies within the converter closed-loop bandwidth, as is experimentally observed.

The loop control was estiablished in order to effect an elimination of any state vector error in n cycles. Since this system is of order 2 and T_s = 50 μs, state errors should be eliminated in 100 μs, at least in the small signal sense. This is of course subject to the accuracy of the approximations made when linearizing the analysis. To test the regulator's transient response, a large signal disturbance of a 100% overload condition is used. The load is switched to 75 Ω which disturbs both the capacitor

voltage state and the inductor current state. When the load is returned to the nominal 150 Ω, the system recovers to its normal operating point. Figure 8.7 is a picture of the oscilloscope trace of the recovery transient. The upper trace is the converter's output voltage. Since the converter is operating without an output capacitor the peak-to-peak voltage ripple is seen to be about 1.5 V or 10% of the dc output level. The lower trace indicates the removal of the overload condition when the signal goes low. While in the overload condition the output voltage drops about 0.5 V from - 15 V to - 14.5 V. When the overload is released, the system is seen to recover without any overshoot in 2 cycles to a very close approximation. This performance is obtained in the face of a rather large disturbance, while the analysis was predicated on small signal approximations. It is clear that in the small signal sense the regulator does indeed exhibit a finite-settling-time response.

For sake of comparison the open-loop response is shown in Fig. 8.8. The transient there is determined by the open-loop poles. The trace shows that 800 μs after the disturbance the output voltage is still oscillating, markedly different behavior than the 100 μs total transient time of the closed-loop regulator. The frequency of oscillation without regulation is approximately 1 kHz as anticipated.

Formulation of this switching regulator relied on time-domain transient analysis. Therefore, the most stringent criterion for the precision of this synthesis technique is comparison of the experimentally obtained transient with the predictions of the modelling. Figure 8.7 provides most convincing testimony, asserting that the linearized

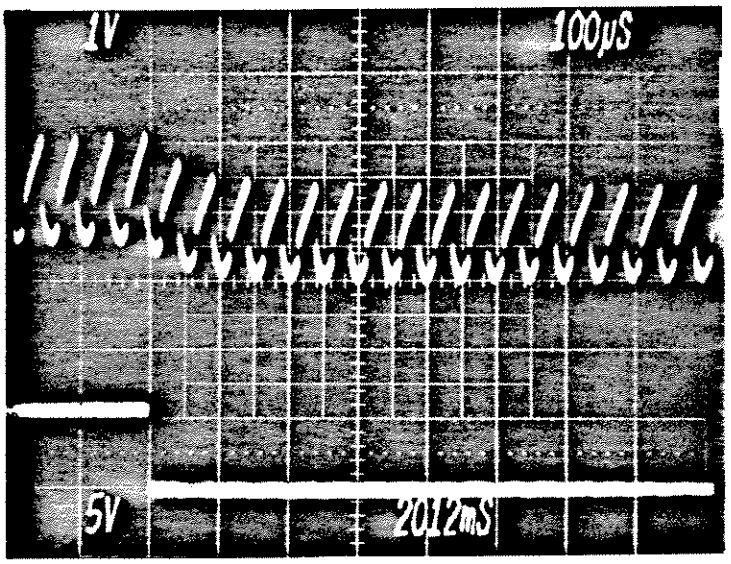

Fig. 8.7 Upper oscilloscope trace with switching frequency ripple evident shows a two-cycle complete recovery from an overload condition. Lower trace step change indicates removal of overload.

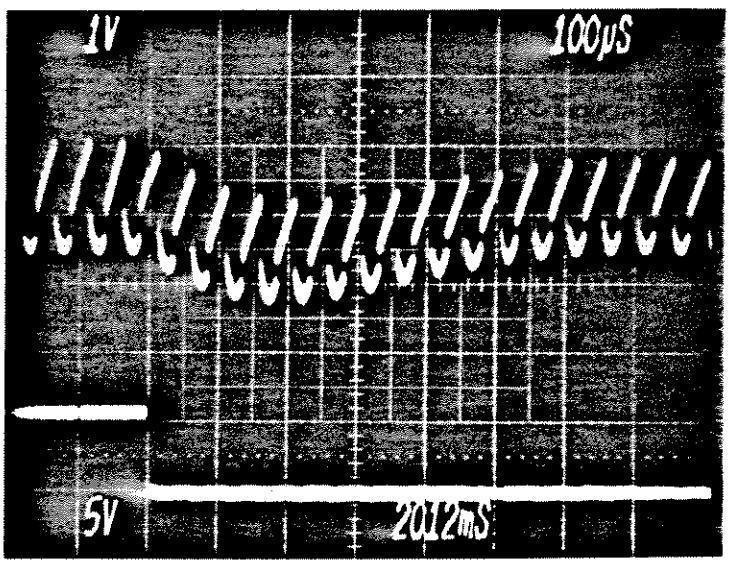

Fig. 8.8 Open-loop recovery from overload condition shows an oscillatory response at the converter's natural plant resonance of about 1 kHz.

discrete model is a potent implement for analysis and design of high-frequency transient behavior. Although the material presented in this chapter is predominantly concerned with obtaining the finite-settling-time response, it should be evident that the discrete approach is not limited to this application. Since such a response is not predicted by continuous models, realization of such performance serves as a persuasive demonstration that there are unique merits associated with the discrete method, and that, even though it certainly is not always the technique of choice, it is a useful approach and adds another dimension to the switching-regulator design engineer's capability.

8.5 Review

Three different viewpoints were adopted in this chapter's analysis of the finite-settling-time state-vector feedback controller. Each frame of reference used had its own particular attributes which allow one to understand certain aspects of the time-optimal control problem.

First, a coordinate frame was defined whose axes lie antiparallel to directions that duty-ratio control sequentially moves the state vector while eliminating the error in a countable number of cycles. The primary utility of this control coordinate reference results from exposure of the error reduction process so that several important fundamental facts may be established. Of essential significance is the result that, subject to the condition that control coordinates span the state space, any small-signal error may be eliminated with a number of discrete control exercises equal to the element count in the state vector. Further, the entire

duty-ratio modulation sequence was shown to be predetermined by the vector coefficients of the initial error expressed in control coordinates. These results would remain academic curiosities were it not for the indispensable conclusion, from a practical standpoint, that the entire control sequence may be implemented with any suitable choice of states by constant-gain vector feedback, thus utilizing the system dynamic response to perform an analog computation for the duty-ratio modulations. Tersely stated, the desired result may be achieved by constant gain linear feedback.

Second, a technique for obtaining the return gains was developed in eigenvector coordinates which decouple the states and thereby minimize mathematical complexity so that emphasis may be placed on the algorithm for solution. Consideration of second-order systems not only resulted in explicit expressions for the gains in terms of eigenvalues and eigenvectors, but also introduced a time-domain method of solution in an unclouded circumstance. Clear indication was obtained from the closed-form results that, for ease of controllability, the open-loop plant should be designed to have well-separated eigenvalues. The simplified notation encountered in this choice of coordinates made the solution easy to implement on a digital computer. Predictions of this automated solution were correlated with experimental findings.

Third, the solution was viewed from an arbitrary spanning coordinate frame in state space, where an alternative controllability criterion was developed, and the existence of an n-cycle sequence of control, predetermined by initial conditions, was re-established. Not only was the choice

of states left arbitrary, but also the system order, and additionally, the use of feedforward to reject external disturbances was included. Despite the formidable appearance of the expanded problem, its time-domain solution, once understood, was shown to be in fact simple, as exemplified by generation of closed-form answers for a buck converter in terms of circuit parameters. The wide applicability of the approach and the possibility of using this method on high-order plants provided sufficient motivation for computer automation. Feedback and feedforward regulation for the second-order example of this chapter was designed digitally by means of a Fortran program written in very general terms for systems up to tenth order.

Experimental verification for the analysis of this chapter was derived from a second-order Ćuk converter regulated to obtain the fastest possible recovery from error. The computer programs aided the circuit design by providing a z-domain root locus for loop-gain stability analysis, as well as by calculation of the optimal regulation gain vector. Describing function results for the loop gain, forecast from the discrete model through use of the transformation to state-space averaging, were obtained by laboratory measurement, which confirmed the theoretical frequency response prediction. The regulator was shown to have good line rejection characteristics within the closed-loop bandwidth, entirely attributable, in this case, to the control which incorporated feedforward from the input voltage as well as state feedback. Direct evaluation of the time-domain analysis was obtained from scrutiny of photographed oscilloscope traces of the system recovery transient. The settling response obtained agrees

extremely well with anticipations, giving solid support to the techniques employed and developed in this chapter.

A seemingly minor contribution to the fabrication of control circuitry for switching regulators is the inclusion of a sample and hold in the feedback loop to prevent switching ripple from interfering with the normal pulse-width-modulation process. Use of the sample and hold rendered the loop control in a form that corresponds well with the piecewise constant assumptions of the derivation, and so, the motivation for inclusion of the sampling circuit was to make the regulator conform to the analysis. However, the sample and hold provides a useful alternative to comparator-based ripple regulation of state variables, such as the current programming discussed in [10]. With a sample and hold preceding the pulse-width-modulation ramp and comparator, it is possible to set a constant feedback gain that will not be affected by the different ripple slopes that occur with changing operating point. Gain compensation then may be done in the usual manner by adjusting error amplification, thus avoiding the complexity and operating condition sensitivity of cyclic ramp compensation as used in [10].

Part 2 of this work is primarily concerned with the regulation of switching converters. The development uses two different modelling techniques, one continuous and one discrete, both relying on identical linearizing assumptions. With either model the controller design has followed the modern control approach, with state vector feedback tacitly assumed and response to initial conditions related to the performance criterion. Whenever possible the results of the modern theory are related

to the concepts of the classical single-return-path formulation, in keeping with the belief that the fullest understanding of the control problem is only obtained by viewing it from as many aspects as available.

In Chapter 6 methods of optimal control theory were applied to the continuous model, establishing a general procedure for regulator design that may be automated from the starting point of the switched state matrices and the selection of a penalty function. Closed-form results were obtained for a buck converter by the Kalman equation method, which was shown to be workable by hand for low-order systems. The buck regulator envisioned promised to have an optimal pole placement and a corresponding minimal transient excursion on output voltage for a given level of control exercise. Such configurations, which can be said to be the best or optimal with respect to a chosen criterion, may in principle be designed for systems of arbitrary order. Once the converter dynamics are cast in a suitable form as developed, methods for solving the optimal linear regulator problem for switching converters with computer automation are suggested and referenced.

In Chapter 7 a linearized discrete model of general applicability for switching regulators was developed and used to determine the stability boundaries for the previously mentioned buck regulator. The results of the analysis were shown to be exactly what one would anticipate when one is aware of the optimal pole positions from Chapter 6 and the transformation developed in Chapter 7 between state-space-averaged results and the linearized-discrete predictions. Commonality was established on several

levels between the continuous and discrete converter representations. A simple but important illustrative example of the discrete analysis revolved around the control of a single inductive current state where useful results of an uncomplicated nature were obtained. Among the outcomes of examining current feedback control was an introduction to the concept of a finite-settling-time response which served as a prelude to Chapter 8 concluding this documentation.

CONCLUSION

Two important problems inherent to switching regulation, both of which stem from the switching process itself, have been addressed. Offsetting the advantages of switching conversion as compared to linear regulation are the drawbacks of switching noise generation and nonlinear response to control. Unfortunately for the uninitiated, these difficulties in switcher design are often not perceived and fully assessed until after the functional form of the converter is established. Then, to the dismay of the designer, corrections for the inadequacies of the fundamental approach usually add to the circuit complexity and leave the engineer dwelling on problems that may have been avoided from the outset. The material contained in this dissertation can provide guidance in avoiding such a quandary or in resolving one that exists.

Part I of this work is concerned with the problem of switching noise. The switching process produces high rates of current change within the converter structure that are sometimes transmitted unattenuated to the source or load, which generates external noise and often conflicts with user requirements or government regulations. The engineer who, by his own lack of foresight, is saddled with resolving such a conflict often must resort to adding filtering elements external to the basic converter. The penalties are that size, weight, and complexity are increased, efficiency is degraded, and in some circumstances converter dynamics are adversely affected, greatly complicating the regulation problem.

The approach taken to circumvent these difficulties begins by examining the intrinsic current waveforms of the various fundamental converter types with particular attention to large discontinuities, if any, that are seen by the source or load. The Ćuk converter stands out in this examination as the only configuration with nonpulsating input and output currents. Hence selection of an appropriate Ćuk topology is a step toward alleviating noise difficulties before they arise. Since the coupled-inductor converter produced unusual and potentially advantageous waveforms, it was chosen as the prime candidate for further investigation and possible improvement.

The coupled-inductor converter was modelled in terms of its capacitor voltage and core flux. The necessary magnetic field relationships were derived from a simple geometric model of the coupled inductor and Maxwell's equations. Application of standard state-space analysis technique resulted in the impedance division model explaining in simple conceptual form some of the previously puzzling current behavior observed. The impedance division model not only serves as an analysis tool but, owing to its simplicity, it may be intuitively understood and manipulated to realize refined or new converter topologies with even more desirable noise attenuation properties. Several such extensions to the basic coupled-inductor Ćuk converter are discussed and shown to have external currents that are nearly the ideal dc quantities. The converters based on impedance division techniques boast the advantages that they are simple to understand and construct, and give good performance with little sensitivity to component tolerances, making them ideal candidates for practical applications.

Since the observed negative-inductance effect is not explained by the impedance division model, a second look was taken at the converter's ripple properties with the additional free parameter of the turns ratio on the coupled inductor. Again idealized component assumptions were employed to facilitate assessment of the new variable's impact. The result obtained which explains the negative inductance effect is easily understandable and unobscured by difficult mathematics in accordance with the analysis. The impedance matching technique that came forth again is a simple enough concept that it could be used as a design tool. Several more new topologies for switching converters based on the Ćuk designs were envisioned and constructed for laboratory verification. Superlative ripple suppression performance was demonstrated for these configurations providing alternatives to the impedance division topologies. The important observation was made that the two ripple attenuation techniques were compatible giving rise to a myriad of possible combinations. One configuration using both methods and exhibiting good component utilization was selected and used for demonstration.

A serendipitous result of the analysis of the coupled-inductor converter is that the impedance matching technique can be applied to other converter types. Boost-type converters can possess zero input ripple and buck types zero output ripple. Further, the basic Ćuk converter without coupled inductors can be rendered zero ripple on input and output since it is boost-buck. These findings stimulated yet a third round of analysis.

A particular arrangement of circuit elements was identified in the converters with the zero-ripple properties and dubbed the new filter.

Rigorous mathematical analysis of the new filter gave a precise frequency-domain understanding of its functioning and the presence of the negative-inductance effect. Application of classical filter theory refined the performance of the new filter by configuring it as an elliptic function filter with transmission zeroes at the switching frequency. Not only was the new filter's performance verified by small-signal laboratory measurements but also its unique merits as a power processing filter were exemplified by its use in a switching audio amplifier.

Thus three new methods of ripple suppression were developed. The impedance division technique, the impedance matching technique, and the new filter all represent refinements to switching conversion that help to alleviate noise problems through judicious topology selection or generation.

Another problem that often plagues switching converter engineers who attempt to design empirically is that of obtaining stable regulation. The engineer who surmounts hardware problems in cookbook fashion is often left with an ill-conditioned plant or is otherwise unable to design appropriate feedback compensation. Often he resorts out of desperation or ignorance to placing a low-frequency dominant pole in the loop that makes the system stable, only at the expense of other performance aspects such as transient response and line rejection.

Part II addresses the control problem for switching converters with emphasis on the application of modern control theory to obtain new alternatives to the classical approaches already in use. The development of control loops that feed back several states is typically foreign to the engineer versed in classical control. For ease of understanding and

comparison with established methods, the presentation relates results whenever possible to the familiar classical concepts. The modern techniques are not promoted as competing with the classical, but are recommended according to their merits to provide additional guidance and capabilities for the design engineer.

A general method is developed for switching converter regulation loop design relying on the use of state-vector feedback and the application of the optimal linear regulator problem to a continuous-time small-signal converter dynamic model. The method is developed from the basic state-space descriptions of the converter dynamics during each of its switched topologies in such a manner that it is evident that any converter may be analyzed in this fashion. Therefore, with the use of optimal control theory a regulation scheme relying on all-state feedback may be formulated for any switching converter and the regulator performance will be the best with respect to a chosen performance criterion. The algorithms for solution of the control problem are laid out so that they may be implemented on a computer, or in simple cases effected by hand. Two forms of buck converter are examined and significant closed-form results are given and related to classical control concepts, showing how one may use the results of classical and modern control theory in harmony.

Another approach to modelling converter dynamics is also developed from fundamental state-space descriptions and as such is also generally applicable to switching converters. This second model relies on a discretized representation of converter dynamics rather than a continuous one and is shown to have certain specific merits in predicting high-frequency transient behavior. A simple yet important example concerning

the discrete control of inductive current provides new insight into the regulation mechanics and their interpretation in the z-domain. The discretized model is useful in both analysis and design of regulators. This is evidenced by an analysis example of a state-vector feedback buck regulator with appropriate comparison to results from established methods, and a design example wherein the fastest possible transient response for a switching regulator is predicted and experimentally obtained. The generality of the discrete analysis is evident in the development, and the accuracy of the predictions is established in the laboratory and by comparison with existing models.

Substantial contributions toward the solution of two of the major problem areas associated with switching conversion are provided. Many new or refined topologies for efficient low-noise power conversion are presented along with explanation of the principles responsible for the improved performance and methodical approaches for generation of such new configurations. General techniques for switching regulator dynamic design and analysis are developed from fundamentals and related to existing methods to provide the engineer with expanded capability to obtain desirable regulator properties.

REFERENCES

[1] Slobodan Ćuk, "Modelling, Analysis, and Design of Switching Converters," PhD thesis, California Institute of Technology, November 1976. Also, NASA Report CR-135174.

[2] R. D. Middlebrook and Slobodan Ćuk, "Isolation and Multiple Output Extensions of a New Optimum Topology Switching Dc-to-Dc Converter," IEEE Power Electronics Specialists Conference, 1978 Record, pp. 256-264 (IEEE Publication 78CH1337-5 AES).

[3] Slobodan Ćuk and R. D. Middlebrook, "Coupled-Inductor and Other Extensions of a New Optimum Topology Switching Dc-to-Dc Converter," IEEE Industry Applications Society Annual Meeting, 1977 Record, pp. 1110-1126 (IEEE Publication 78CH1246-8-IA).

[4] Slobodan Ćuk, "Discontinuous Inductor Current Mode in the Optimum Topology Switching Converter," IEEE Power Electronics Specialists Conference, 1978 Record, pp. 105-123 (IEEE Publication 77CH 1213-8 AES).

[5] R. D. Middlebrook, Slobodan Ćuk, and W. Behen, "A New Battery Charger/Discharger Converter," IEEE Power Electronics Specialists Conference, 1978 Record, pp. 251-255 (IEEE Publication 78CH1337-5 AES).

[6] Slobodan Ćuk and Robert W. Erickson, "A Conceptually New High-Frequency Switched-Mode Amplifier Technique Eliminates Current Ripple," Proc. Fifth National Solid-State Power Conversion Conference (Powercon 5), pp. G3.1-G3.22, May 1978.

[7] Slobodan Ćuk, "Switching Dc-to-Dc Converter with Zero Input or Output Current Ripple," IEEE Industry Applications Society Annual Meeting, 1978 Record, pp. 1131-1146, IEEE Publication 78CH1346-61A.

[8] R. D. Middlebrook, "Modelling and Design of the Ćuk Converter," Proc. Sixth National Solid-State Power Conversion Conference (Powercon 6), pp G3-1 to G3-14.

[9] Loman Rensink, Art Brown, Shi-Ping Hsu, and Slobodan Ćuk, "Design of a Kilowatt Off-Line Switcher Using a Ćuk Converter," Proc. Sixth National Solid-State Power Conversion Conference (Powercon 6) pp H3-1 to H3-26.

[10] Shi-Ping Hsu, Art Brown, Loman Rensink, and R. D. Middlebrook, "Modelling and Analysis of Switching Dc-to-Dc Converters in Constant-Frequency Current-Programmed Mode," IEEE Power Electronics Specialists Conference, 1979 Record.

[11] Slobodan Ćuk, "Dc-to-dc Switching Converter with Zero Input and Output Current Ripple and Integrated Magnetics Circuits," U.S. Patent Application S.N.026,541 filed March 30, 1979.

[12] A. Bryson & Y. Ho, Applied Optimal Control, John Wiley & Sons, NY, 1975.

[13] D. Schultz & J. Melsa, State Functions and Linear Control Systems, McGraw-Hill, NY, 1967.

[14] J. Melsa & S. Jones, Computer Programs for Computational Assistance in the Study of Linear Control Theory, McGraw-Hill, NY, 1973.

[15] H. Kwakernaak & R. Sivan, Linear Optimal Control Systems, Wiley-Interscience, NY, 1972.

[16] R. E. Kalman, "When is a Linear Control System Optimal?" J. Basic Eng., Trans ASME, SerD, Vol 86, pp 51-60, 1964.

[17] J. N. Franklin, Matrix Theory, Prentice Hall, Englewood Cliffs, NY. 1968.

[18] Dennis J. Packard, "Discrete Modeling and Analysis of Switching

Regulators," PhD thesis, California Institute of Technology, May 1976; also, Report No. M76-43, Hughes Aircraft Co., Aerospace Groups, Culver City, Calif.

[19] B. C. Kuo, Linear Networks and Systems, McGraw-Hill, NY, 1967.

[20] Saucedo & Schiring, Introduction to Continuous and Digital Control Systems, The Macmillan Company, London, 1968.

[21] C. W. Deisch, "Simple Switching Control Method Changes Power Converter into a Current Source" IEEE Power Electronics Specialists Conference, 1978 Record, pp 300-306.

[22] Kalman & Bertram, "General Synthesis Procedure for Computer Control of Single-Loop and Multiloop Linear Systems," Trans AIEE, 78, Pt. 2, 602-609, 1959.

[23] D. P. Lindorff, Theory of Sampled-Data Control Systems, John Wiley & Sons Inc., NY, 1965.

[24] R. D. Middlebrook, "Measurement of Loop Gain in Feedback Systems," International J. of Electronics, vol. 38, no. 4, pp 485-512, April 1975.

[25] R. D. Middlebrook, "Improved-Accuracy Phase Angle Measurement," International J. of Electronics, vol. 40, no. 1, pp 1-4, Jan. 1976.

APPENDIX

COMPUTER PROGRAMS

In the course of developing the material for this dissertation it was found expedient at times to resort to computer-aided design, when the result sought had sufficient importance and the required method involved tedious or repetitious calculations. To aid the reader in duplicating, or building on, the design examples presented in the text, the Fortran coding for three of the programs is included here.

The first program calculates the circuit element values for the new filter of Chapter 5. The input variables are; AR, the passband ripple amplitude in dB, EM, the lowest stop-band frequency (trial and error is needed here to place the zeroes at a selected switching frequency), FB, the passband ripple bandwidth, and R, the nominal load resistance. The program output includes the normalized low-pass poles and zeroes for the third-order elliptic function filter and the circuit parameters for the new filter configuration that generates the elliptic response. The output format identifies the dc biased inductor as L, the tap fraction as A, the tap inductor as L1, and the blocking capacitor as C. The inputs are read by namelist, so the data card generating the design of Chapter 5 begins in column 2 and reads:

```
 $INPUT AR=2., EM=3.5., FB=20000., R=8. $
```

For this input the program output should include:

```
L= 1.9392E-04  A= 5.6948E-01  L1= 5.0772E-05  C= 1.2136E-06
```

These values are provided so that the program may be tested when adapted to another computer. A complete program listing follows:

```
      PROGRAM ELLIP (INPUT,OUTPUT,TAPE5=INPUT,TAPE6=OUTPUT)
      COMPLEX POLE(20),ZERO(20),T1,T2,T3,TZS,NUM,DEN
      DATA N,TUPI /3,6.283185308/
      REAL L,L1
      PK(X)=SQRT (1.-X*X)
      NAMELIST /INPUT/AR,EM,FB,R
    5 READ (5,INPUT)
      IF (EOF(5).NE.0.) STOP
      WRITE (6,INPUT)
      AP=10.**(-.05*AR)
      AK2=1./EM
      CK2=COMK(AK2)
      AK1=QINV(AK2,N)
      GA=CK2*FINC(ASIN(AP),PK(AK1))/N/COMK(AK1)
      CALL JACOBI (GA,PK(AK2),SN2,CN2,DN2,PHN2)
C-----N MUST BE ODD   NO PROVISIONS FOR EVEN ORDERS.
      DO 10 I=2,N,2
      BETA =CK2*(1.-(I-1.0)/N)
      CALL JACOBI (BETA,AK2,SN1,CN1,DN1,PHN1)
      ZERO(I)=CMPLX(0.,-1./AK2/SN1)
      ZERO(I-1)=CONJG(ZERO(I))
      EPS=1.-(DN1*SN2)**2
      POLE(I)=CMPLX (-CN1*DN1*SN2*CN2,-SN1*DN2)/EPS
   10 POLE(I-1)=CONJG (POLE(I))
      POLE(N)=-SN2/CN2
      M=N-1
      WRITE (6,50) (ZERO(I),I=1,M)
   40 WRITE (6,60) (POLE(I),I=1,N)
   50 FORMAT (/1X25HNORMALIZED LOW PASS ZEROS //(2F20.8))
   60 FORMAT (/1X25HNORMALIZED LOW PASS POLES //(2F20.8))
```

```
C-----FORM TIME CONSTANTS FROM NORMALIZED POLES AND INPUT BREAK FREQUENCY.
      T1=-1./POLE(1)/FB/TUPI
      T2=-1./POLE(2)/FB/TUPI
      T3=-1./POLE(3)/FB/TUPI
      TZS= 1./(ZERO(1)*ZERO(2))/FB/FB/TUPI/TUPI
C-----COMPUTE OPTIMAL FILTER ELEMENT VALUES
      L=R*REAL(T1+T2+T3)
      NUM=TZS-T1*T2*T3/(T1+T2+T3)
      DEN=(T1*T2+T1*T3+T2*T3-TZS)
      A=REAL(NUM/DEN+1.)
      C=1./L*REAL(T1*T2+T1*T3+T2*T3-TZS)/A
      L1=REAL(T1*T2*T3/(T1+T2+T3))/C
C-----OUTPUT RESULTS.
      WRITE (6,70) L,A,L1,C
   70 FORMAT(//1X,22HCIRCUIT ELEMENT VALUES /,4H L= 1PE10.4,5X
     13HA= E10.4,5X,4HL1= E10.4,5X,3HC= E10.4 )
      GO TO 5
      END

      FUNCTION COMK(X)
C-----COMPLETE ELLIPTIC INTEGRAL
      Y=1.-X*X
      COMK=1.386294361+ .09666344259*Y +.03590092383*Y*Y +
     1  .03742563713*Y*Y*Y + .01451196212*Y*Y*Y*Y
      COMK=COMK+(.5+ .1249859357*Y + .06880248576*Y*Y +
     1  .03328355346*Y*Y*Y + .00441787012*Y*Y*Y*Y)*ALOG(1./Y)
      RETURN
      END

      SUBROUTINE JACOBI(U,AK,SN,CN,DN,PHN)
C-----JACOBI ELLIPTIC FUNCTIONS
      DIMENSION A(10),B(10),C(10)
```

```
      ASN(X)=ATAN(X/SQRT(1.-X*X))
      ACC=1.E-12
   80 N=1
      A(1)=1.
      B(1)=SQRT(1.-AK*AK)
   30 M=N
      N=N+1
      IF(N-10) 60,60,70
   70 ACC=ACC*10.
      WRITE (6,90) ACC
   90 FORMAT (5X,3HACC,E20.8)
      GO TO 80
   60 A(N)=.5*(A(M)+B(M))
      B(N)=SQRT(A(M)*B(M))
      C(N)=.5*(A(M)-B(M))
      IF (ABS(C(N))-ACC) 20,20,30
   20 PHN=2.**(N-1)*A(N)*U
      DO 100 I=2,N
      L=N-I+2
  100 PHN=.5*(PHN+ASN(C(L)/A(L)*SIN(PHN)))
      SN=SIN(PHN)
      CN=COS(PHN)
      DN=SQRT(1.-(AK*SN)**2)
      RETURN
      END

      FUNCTION FINC(PH,AL)
C-----INCOMPLETE ELLIPTIC INTEGRAL
      ASN(X) =ATAN(X/SQRT(1.-X*X))
      PK(X)=SQRT(1.-X*X)
      PHI=PH
```

```
      IF(A1-1.E-6) 10,10,30
   30 AK=A1
      ACC=1.E-12
      FA=1.
  100 PHI=.5*(PHI+ASN(AK*SIN(PHI)))
      AK=2.*SQRT(AK)/(1.+AK)
      FA=FA*(1.+PK(AK))
      IF (1.-ACC-AK) 20,20,100
   20 PHI=.25*(PHI+ASN(AK*SIN(PHI)))
      FINC=FA*ALOG((COS(PHI)+SIN(PHI))/(COS(PHI)-SIN(PHI)))
      RETURN
   10 FINC=PH
      RETURN
      END

      FUNCTION QINV (AK,N)
C----- Q**N AND INVERSE Q
      IF (AK-.7) 10,10,20
   10 AP=SQRT(1.-AK*AK)
      GO TO 21
   20 AP=AK
   21 AP=SQRT(AP)
      E=.5*(1.-AP)/(1.+AP)
      Q=E+2.*E**5+15.*E**9+150.*E**13
      IF(AK-.7)30,30,40
   40 Q=EXP(9.8696044010894 /ALOG(Q))
   30 CONTINUE
      Q=Q**N
      IF(Q-.043)50,50,60
   60 Q=EXP(9.8696044010894 /ALOG(Q))
      QINV=(1.+Q*Q+Q**6)/(1.+2.*Q+2.*Q**4)
      QINV=SQRT(1.-16.*Q*QINV**4)
```

```
      GO TO 100
   50 QINV=(1.+Q*Q+Q**6)/(1.+2.*Q+2.*Q**4)
      QINV=4.*SQRT(Q)*QINV*QINV
  100 RETURN
      END
```

The second computer program solves for the finite-settling-time feedback gains for a second-order switching converter. The inputs to the program are: A, the state-space-averaged natural response matrix, T, the switching period, and B, the averaged duty-ratio control influence vector (termed g in the text). The program proceeds to output the state transition matrix F, its eigenvalues and eigenvector elements, and the feedback gains with a minus sign included identified as C1 and C2. Subsequently the program generates loop gain root locus information including the z-domain poles and the element values of the closed-loop matrix M. The input for the design example of Chapter 8 is:

```
 $INPUT A=0.0, 9.33E+04, -500., -1244., T=50.E-06,
  B=3.0E+04, -3.73E+04 $
```

The output should agree with the example in the text. A complete program listing follows:

```
      PROGRAM FINITE (INPUT,OUTPUT,TAPE5=INPUT,TAPE6=OUTPUT)
      COMPLEX LAMDA1,LAMDA2,TRF,DETF,L21,L22,G1,G2,K1,K2,C(2),S,P1,P2
     1,TRM,DETM
      REAL M(2,2),K
      DIMENSION A(2,2),F(2,2),B(2)
      NAMELIST /INPUT/ A,T,B
   10 READ (5,INPUT)
      WRITE (6,INPUT)
      IF (EOF(5).NE.0.) STOP
C-----ESTABLISH I+AT=F
      F(1,1)=A(1,1)*T+1.
      F(1,2)=A(1,2)*T
      F(2,1)=A(2,1)*T
      F(2,2)=A(2,2)*T+1.
      WRITE (6,30) F(1,1),F(1,2),F(2,1),F(2,2)
   30 FORMAT (/24H STATE TRANSITION MATRIX,/2(1PE10.3)/,2(1PE10.3)/)
C-----DETERMINE THE EIGENVALUES OF F.
      TRF=F(1,1)+F(2,2)
      DETF=F(1,1)*F(2,2)-F(1,2)*F(2,1)
      LAMDA1=TRF/2.+CSQRT((TRF/2.)**2-DETF)
      LAMDA2=TRF/2.-CSQRT((TRF/2.)**2-DETF)
      WRITE (6,40) LAMDA1,LAMDA2
   40 FORMAT ( 8H LAMDAS=,4(1PE10.3)/)
C-----NORMALIZED EIGENVECTOR ELEMENTS.
      L21=-(F(1,1)-LAMDA1)/F(1,2)
      L22=-(F(1,1)-LAMDA2)/F(1,2)
      WRITE (6,50) L21,L22
   50 FORMAT (  5H L21=,2(1PE10.3),2X,4HL22=,2(1PE10.3),/)
      G1=(L22*B(1)-B(2))*T/(L22-L21)
      G2=(-L21*B(1)+B(2))*T/(L22-L21)
```

```
      WRITE (6,60) G1,G2
   60 FORMAT (  4H G1=,2(1PE10.3),2X, 3HG2=,2(1PE10.3),/)
      K1=-LAMDA1**2/(LAMDA1-LAMDA2)/G1
      K2= LAMDA2**2/(LAMDA1-LAMDA2)/G2
      WRITE (6,70) K1,K2
   70 FORMAT (  4H K1=,2(1PE10.3),2X, 3HK2=,2(1PE10.3),/)
      C(1)=(K1*L22-K2*L21)/(L22-L21)
      C(2)=(K2-K1)/(L22-L21)
      WRITE (6,80) C(1),C(2)
   80 FORMAT ( 4H C1=,2(1PE10.3),2X, 3HC2=,2(1PE10.3),//)
C-----ITERATE K AND SOLVE FOR CLOSED LOOP Z-PLANE POLE LOCATIONS.
      WRITE (6,85)
   85 FORMAT(//41H CLOSED LOOP Z-PLANE POLE POSITIONS VS K1,/)
      K=-.2
      DO 120 JZ=1,11
C-----FORM M MATRIX M=BCKT,K 0 TO 2.
      K=K+.2
      DO 95 J=1,2
      DO 90 I=1,2
   90 M(I,J)=B(I)*C(J)*K*T+F(I,J)
   95 CONTINUE
      WRITE (6,100)((M(I,J),I=1,2),J=1,2)
  100 FORMAT (/ 20H M MATRIX ELEMENTS  ,4(1PE10.3), )
C-----DETERMINE EIGENVALUES OF M.
      TRM=M(1,1)+M(2,2)
      DETM=M(1,1)*M(2,2)-M(1,2)*M(2,1)
      S=CSQRT((TRM/2.)**2-DETM)
      P1=TRM/2.+S
      P2= TRM/2.-S
      WRITE (6,110) P1,P2,K
```

```
110 FORMAT ( 4H P1= ,2(1PE10.3),4X, 3HP2=,2(1PE10.3)2X,3HK= ,0PF6.2)
120 CONTINUE
    GO TO 10
    END
```

The third and final program also solves for the finite-settling-time control gains, but does so in much greater generality and accepts the most fundamental inputs. The input information is taken in the form of the two switched subintervals' state-space matrices A1, A2, B1, and B2 named in accordance with their identification in Chapters 7 and 8. Additional inputs are the duty ratio D, the switching period T, the nominal control vector U, the system order NA, the number of control influences NU, and a logical variable LX to use input values of the steady-state operating point in the solution. The program calculates the matrices of the complete discrete dynamic model including the duty-ratio modulation influence vector (and hence the operating conditions), and prints out the results along with the input information, all identified in accordance with the nomenclature in the text. It then utilizes the generalized coordinate solution to obtain the feedforward and feedback gains, and while so doing it prints out the controllability matrix and its inverse. The input for the design example is:

```
 $INPUT a1(1,1)=0.,A1(2,1)=0.,A1(1,2)=0.,A1(2,2)=-1244.,
  A2(1,1)=0.,A2(2.1)=186567.,A2(1,2)=-1000.,A2(2,2)=-1244.,
  B1(1,1)=1000.,B1(2,1)=1244.,B2(1,1)=1000.,B2(2,1)=1244.,
  D=0.5,T=50.E-6,U(1,1)=15.,NA=2,NU=1,LX=.F. $
```

The output should agree with the numbers given in Chapter 8. A complete program listing follows:

```
      PROGRAM FINITE (INPUT,OUTPUT,TAPE5=INPUT,TAPE6=OUTPUT)
      LOGICAL LX
      DIMENSION A1(10,10),A2(10,10),B1(10,10),B2(10,10),F(10,10),
     1 B(10,10),G(10,10),U(10,10),X0(10,10),FI(10,10),FIB(10,10),
     2 HM(10,10),XP(10,10),UP(10,10),CO(10,10),COI(10,10),FNA(10,10),
     3 FNAB(10,10),FG(10,10),CFG(10,10),AM(10,10)
      NAMELIST /INPUT/A1,A2,B1,B2,D,T,U,NA,NU,LX
      NAMELIST /OUTPUT/D,T,NA,NU
   10 READ(5,INPUT)
      IF (EOF(5),NE,0.) STOP
      WRITE (6,OUTPUT)
C-----PRINT THE STATE MATRICIES,
      WRITE (6,15)
   15 FORMAT (//3H A1//)
      CALL PMX (A1,NA,NA)
      WRITE (6,20)
   20 FORMAT (//3H B1//)
      CALL PMX(B1,NA,NU)
      WRITE (6,25)
   25 FORMAT (//3H A2//)
      CALL PMX (A2,NA,NA)
      WRITE (6,30)
   30 FORMAT (//3H B2//)
      CALL PMX (B2,NA,NU)
      WRITE (6,37)
   37 FORMAT (//2H U//)
      CALL PMX(U,NU,1)
C-----DP IS 1-D,
```

```
      DP=1.-D
C-----FORM F THE STATE TRANSITION MATRIX.
C-----DONT ADD THE IDENTITY MATRIX UNTIL AFTER X0 IS CALCULATED.
      DO 50 J=1 ,NA
      DO 40 I=1,NA
   40 F(I,J)=A1(I,J)*D*T+A2(I,J)*DP*T
   50 CONTINUE
C-----FORM B THE CONTROL INFLUENCE MATRIX.
C-----B IS NA BY NU
      DO 70 J=1,NU
      DO 60 I=1,NA
   60 B(I,J)=B1(I,J)*D*T+B2(I,J)*DP*T
   70 CONTINUE
C-----OUTPUT B.
      WRITE (6,75)
   75 FORMAT (2H B//)
      CALL PMX (B,NA,NU)
C-----CALCULATE THE STEADY STATE BOUNDARY CONDITION X0.
C-----FORM INVERSE OF F=I.
      CALL ELIM (F,NA,FI)
C-----FORM PRODUCT OF FI AND B.
      CALL MXMLPY(FI,NA,NA,B,NA,NU,FIB)
C-----OPTIONAL USE OF INPUT X0 WITH LX TRUE.
      IF (LX) GO TO 77
      CALL MXMLPY(FIB,NA,NU,U,NU,1,X0)
      DO 76 I=1,NA
   76 X0(I,1)=-X0(I,1)
   77 CONTINUE
      DO 80 I=1,NA
      F(I,I)=F(I,I)+1.
```

```
   80 CONTINUE
C------PRINT F
      WRITE (6,95)
   95 FORMAT (// 2H F//)
      CALL PMX (F,NA,NA)
C------PRINT X0.
      WRITE (6,97)
   97 FORMAT ( 3H X0//)
      CALL PMX (X0,NA,1)
C------FORM G, THE DUTY RATIO MODULATION INFLUENCE VECTOR.
      DO 110 J=1,NA
      DO 100 I=1,NA
  100 AM(I,J)=(A1(I,J)-A2(I,J))
  110 CONTINUE
      DO 130 J=1,NU
      DO 120 I=1,NA
  120 BM(I,J)=(B1(I,J)-B2(I,J))
  130 CONTINUE
C------FORM INTERMEDIATE VARIABLES X-PRIME AND U-PRIME.
      CALL MXMLPY(AM,NA,NA,X0,NA,1,XP)
      CALL MXMLPY(BM,NA,NU,U,NU,1,UP)
      DO 140 I=1,NA
  140 G(I,1)=(XP(I,1)+UP(I,1))*T
C------PRINT OUT G.
      WRITE (6,150)
  150 FORMAT (//2H G//)
      CALL PMX (G,NA,1)
C------FORM THE DMAT COEFFICIENT MATRIX COMPRISED OF COLUMNS OF DESCENDING
C------POWERS OF F TIMES G.
      CALL COEF (F,G,NA,CO)
```

```
      WRITE (6,160)
  160 FORMAT (//3H CO//)
      CALL PMX (CO,NA,NA)
C*****FORM THE INVERSE OF CO.
      CALL ELIM (CO,NA,COI)
      WRITE (6,170)
  170 FORMAT (//4H COI//)
      CALL PMX(COI,NA,NA)
C*****FORM *F**N AND *F**N*1*B.
      CALL PWR (F,NA,B,NU,FNA,FNAB)
      DO 174 J=1,NA
      DO 172 I=1,NA
      FNAB(I,J)=-FNAB(I,J)
  172 FNA(I,J)=-FNA(I,J)
  174 CONTINUE
      WRITE (6,180)
  180 FORMAT (//7H -F**NA//)
      CALL PMX (FNA,NA,NA)
      WRITE (6,190)
  190 FORMAT (//13H -F**(NA-1)*B//)
      CALL PMX (FNAB,NA,NU)
C*****FORM THE FINITE SETTLING TIME GAIN VECTOR FROM THE FIRST ROW OF
C*****COI AND F**NA
      CALL MXMLPY (COI,1,NA,FNA,NA,NA,FG)
      WRITE (6,200)
  200 FORMAT (//34H FINITE SETTLING TIME GAIN VECTOR //)
      CALL PMX (FG,1,NA)
C*****FORM THE CONTROL FEEDFORWARD GAIN VECTOR.
      CALL MXMLPY (COI,1,NA,FNAB,NA,NU,CFG)
      WRITE (6,210)
```

```
  210 FORMAT (//32H CONTROL FEEDFORWARD GAIN VECTOR //)
      CALL PMX (CFG,1,NU)
C-----RETURN TO DO ANOTHER CASE.
      GO TO 10
      END

      SUBROUTINE PMX (X,I,J)
C-----THIS SUBROUTINE PRINTS THE X MATRIX DIMENSIONED I BY J LESS THAN 10X10.
      DIMENSION X(10,10)
      DO 100 L=1,I
  100 WRITE (6,200) (X(L,K),K=1,J)
  200 FORMAT (//,10(2X,1PE11.4))
      RETURN
      END

      SUBROUTINE MXMLPY(X,I,J,Y,K,L,Z)
C-----THIS SUBROUTINE FORMS MATRIX PRODUCTS X*Y,X I BY J,Y K BY L
C-----AND RETURNS THE RESULT IN Z. J MUST EQUAL K.
      DIMENSION X(10,10),Y(10,10),Z(10,10)
      DOUBLE PRECISION D(10,10)
C-----TEST FOR INVALID CALL.
      IF (J.NE.K) GO TO 40
      DO 30 LL=1,L
      DO 20 II=1,I
      D(II,LL)=0.
C-----FORM A ROW-COLUMN PRODUCT.
      DO 10 JK=1,J
   10 D(II,LL)=X(II,JK)*Y(JK,LL)+D(II,LL)
      Z(II,LL)=D(II,LL)
   20 CONTINUE
```

```
   30 CONTINUE
      RETURN
   40 WRITE (6,50)
   50 FORMAT (///24H INVALID CALL TO MXMLPY /1X,22(1H*))
      STOP
      END

      SUBROUTINE COEF (F,G,NA,CO)
C*****THIS SUBROUTINE FORMS THE DHAT COEFFICIENT MATRIX FROM F AND G.
      DIMENSION F(10,10),G(10,10), CO(10,10),TEMP(10,10)
C*****ZERO PART OF CO OPERATED ON.
      DO 100 J=1,NA
      DO 50 I=1,NA
   50 CO(I,J)=0.
  100 CONTINUE
C*****LOAD G VECTOR INTO SUCESSIVE COLUMNS OF CO.
      DO 200 J=1,NA
      DO 150 I=1,NA
  150 CO(I,J)=G(I,1)
      IF (J.EQ.NA) RETURN
C*****REPEATEDLY MULTIPLY BY F.
      CALL MXMLPY (F,NA,NA,CO,NA,NA,TEMP)
C*****REPLACE CO WITH ITS UPDATED VALUE.
      DO 170 L=1,NA
      DO 160 K=1,NA
  160 CO(K,L)=TEMP(K,L)
  170 CONTINUE
  200 CONTINUE
      END
```

```
      SUBROUTINE PWR (F,NA,B,NU,FNA,FNAB)
C-----THIS SUB CALCULATES THE NTH POWER OF F AND THE N-1 POWER TIMES B
      DIMENSION F(10,10),B(10,10),FNA(10,10),FNAB(10,10),TEMP(10,10)
C-----SET TEMP TO IDENTITY.
      DO 100 J=1,NA
      DO 50 I=1,NA
      TEMP(I,J)=0.
   50 IF(I.EQ.J) TEMP(I,J)=1.
  100 CONTINUE
      DO 300 J=1,NA
      CALL MXMLPY (F,NA,NA,TEMP,NA,NA,FNA)
      IF (J.EQ.NA) GO TO 400
C-----OTHERWISE SET TEMP TO FNA AND REPEAT MULTIPLICATION BY F.
      DO 200 L=1,NA
      DO 150 K=1,NA
  150 TEMP(K,L)=FNA(K,L)
  200 CONTINUE
  300 CONTINUE
C-----TEMP IS F**NA-1 AND FNA IS F**NA
C-----FORM F**NA-1 TIMES B.
  400 CALL MXMLPY (TEMP,NA,NA,B,NA,NU,FNAB)
      RETURN
      END

      SUBROUTINE ELIM (A,NA,X)
C-----THIS ROUTINE USES GAUSS-JORDAN ELIMINATION WITH MAXIMUM PIVOT
C-----STRATEGY TO SOLVE FOR THE INVERSE OF A REAL MATRIX.
      LOGICAL ROW(10),COL(10)
      DIMENSION A(10,10),W(20,10),B(10,10),X(10,10)
      DOUBLE PRECISION W,P,ABSP,WEIGHT
```

```
C------ELIM CAN HANDLE UP TO A 10X10 SYSTEM.
      DIMENSION IROW(10),ICOL(10)
C------A IS THE COEFFICIENT MATRIX,  B IS THE AUGMENTING MATRIX.
C------X WILL RETURN THE SOLUTION MATRIX,  NA IS SYSTEM ORDER.
      NAMELIST /EL/A,ROW,COL,IROW,ICOL
C------ESTABLISH THE AUGMENTING IDENTITY MATRIX.
      DATA B/100*0./
      DO 50 I=1,NA
   50 B(I,I)=1.
C------LOAD ELEMENTS INTO AUGMENTED WORKING ARRAY---A AND B REMAIN UNTOUCHED.
      NA2=NA+NA
      DO 110 I=1,NA
      DO 100 J=1,NA
C------A TRANSPOSE POSITION IS USED TO IMPROVE EFFICIENCY.
      W(J+NA,I)=B(I,J)
  100 W(J,I)=A(I,J)
C------SET PIVOT SEARCH LOGICALS FALSE.
      ROW(I)=.F.
      COL(I)=.F.
  110 CONTINUE
C------BEGINING OF THE ELIMINATION LOOP.
      DO 200  K=1,NA
      ABSP=0.
      P=0.
C------CHOOSE THE LARGEST PIVOT ELEMENT NOT IN A PREVIOUSLY USED ROW OR
C------COLUMN.
      DO 140 M=1,NA
      IF (COL(M))       GO TO 140
      DO 130 L=1,NA
      IF (ROW(L))       GO TO 130
```

```
      IF (ABSP.GT.DABS(W(L,M)))GO TO 130
      P=W(L,M)
      ABSP=DABS(P)
C-----STORE THE PIVOT LOCATION FOR EVENTUAL UNSCRAMBLING THE ANSWER.
      IR=L
      IC=M
  130 CONTINUE
  140 CONTINUE
C-----CHECK TO SEE IF PROBLEM IS INDETERMINATE.
      IF (ABSP.GT.1E-6) GO TO 160
      WRITE (6,150) ABSP
  150 FORMAT (/35H MAXIMAL PIVOT ELEMENT MAGNITUDE IS,1PE12.5,1X
     1 36H THE EQUATIONS MAY BE INDETERMINATE.,/)
      WRITE (6,EL)
      STOP
C-----SET SORTING LOGICALS AND PIVOT ARRAYS.
  160 IROW(K)=IR
      ROW(IR)=.T.
      ICOL(K)=IC
      COL(IC)=.T.
C-----DIVIDE THE COLUMN BY ITS PIVOT.
      DO 170 N=1,NA2
  170 W(N,IC)=W(N,IC)/P
C-----ELIMINATE THE PIVOT ROW.
C-----JJ IS THE COLUMN WHERE THE ELIMINATION IS DONE.
      DO 190 JJ=1,NA
C-----AVOID OPERATING ON THE PIVOT COLUMN.
      IF (JJ.EQ.IC) GO TO 190
      WEIGHT=W(IR,JJ)
      DO 180 II=1,NA2
```

```
C------SUBTRACT THE WEIGHTED PIVOT COLUMN FROM EVERY OTHER COLUMN.
  180 W(II,JJ)=W(II,JJ)-W(II,IC)*WEIGHT
  190 CONTINUE
C------ALL W(IR,JJ)=0  EXCEPT FOR JJ=IC.
C------END OF THE ELIMINATION LOOP.  K IS INCREMENTED AND THE PROCESS
C------REPEATED UNTIL THE WORKING ARRAY IS AN IDENTITY MATRIX AUGMENTED
C------BY THE INVERSE MATRIX---POSSIBLY SCRAMBLED.
  200 CONTINUE
C------STORE THE SOLUTION IN X IN UNSCRAMBLED ORDER.
      DO 220 LL=1,NA
      LN=LL+NA
      DO 210 KK=1,NA
  210 X(IROW(KK),LL)=W(LN,ICOL(KK))
  220 CONTINUE
      RETURN
      END
```